Heat Transfer Augmentation Surfaces Using Modified Dimples/Protrusions

Mohammad A. Elyyan

Dissertation submitted to the faculty of Virginia Polytechnic Institute and State University in partial fulfillment of the requirement for the degree of

Doctor of Philosophy
in
Mechanical Engineering

Chairman:
Prof. Danesh K. Tafti

Committee Members:
Prof. Kenneth S. Ball
Prof. Thomas E. Diller
Prof. Mark R. Paul
Prof. Saad A. Ragab

December 9, 2008

Blacksburg, Virginia

Keywords: Large Eddy Simulation, Fins, Dimples, Compact Heat Exchangers, Turbine Cooling.

Heat Transfer Augmentation Surfaces Using Modified Dimples/Protrusions

ABSTRACT

Mohammad A. Elyyan

This work presents direct and large eddy simulations of a wide range of heat augmentation surfaces roughened by modified dimples/protrusions. The dissertation is composed of two main parts: Part I (Chapters 2-4) for compact heat exchangers and Part II (Chapter 5) for internal cooling of rotating turbine blades. Part I consists of three phases: Phase I (Chapter 2) investigates flow structure and heat transfer distribution in a channel with dimples/protrusions; Phase II (Chapter 3) studies the application of dimples as surface roughness on plain fins; and Phase III (Chapter 4) considers a new fin shape, the split-dimple fin, that is based on modifying the conventional dimple shape.

Chapter 2 presents direct and large eddy simulations conducted of a fin bank over a wide range of Reynolds numbers, Re_H=200-15,000, covering the laminar to fully turbulent flow regimes and using two channel height geometries. While the smaller fin pitch channel has better performance in the low to medium Reynolds number range, both channel heights show similar trends in the fully turbulent regime. Moreover, analysis of the results shows that vortices generated in the dimple cavity and at the dimple rim contribute substantially to heat transfer from the dimpled surface, whereas flow impingement and acceleration between protrusions contribute substantially on the protrusion side.

Chapter 3 considers applying dimples as surface roughness on plain fin surfaces to further enhance heat transfer from the fin. Three fin geometries that consider dimple imprint diameter effect and perforation effect are considered. The dimple imprint diameter has a minimal effect on the flow and heat transfer of the fin. However, the introduction of perforation in the dimple significantly changes the flow structure and heat transfer on the dimple side of the fin by eliminating recirculation regions in the dimple and generating higher intensity vortical structures.

Chapter 4 presents a novel fin shape, the split-dimple fin, which consists of half a dimple and half a protrusion with an opening between them. The split dimple provides an additional mechanism for augmenting heat transfer by perturbing continuous boundary layer formation on the fin surface and generating energetic shear layers. While the protruding geometry of the split dimple augments heat transfer profoundly, it also increase pressure drop. The split dimple fin results in heat conductance that is 60–175% higher than a plain fin, but at a cost of 4–8 times the frictional losses.

Chapter 5 studies the employment of dimples/protrusions on opposite sides for internal cooling of rotating turbine blades. Two geometries with two dimple/protrusion depths are investigated over a wide range of rotation numbers, Ro_b=-0.77 to 1.10. Results show that the dimple side is more sensitive to the destabilizing forces on the trailing surface, while both react similarly to the stabilizing effect on the leading side. It is concluded that placing the protrusion on the trailing side for low rotation number, $|Ro_b|<0.2$, provides better performance, while it is more beneficial to place the dimple side on the trailing side for higher rotation numbers.

To my mom and to the soul of my father

Acknowledgments

بسم الله الرحمن الرحيم

Praise is due to Allah, the Beneficient, the Merciful. First and foremost, I would like to thank God for his blessings and help that He has bestowed on me throughout my journey in life.

I would like to express my sincere gratitude to my advisor, Professor Tafti, whose consistent guidance, inspiring ideas, unlimited support, and devotion to research and helping his student—even on Sundays—were priceless elements that helped me complete this degree. My experience through the PhD degree was extremely fruitful; I really enjoyed doing research, coming to the office every day, talking with my fellow students and my professors. I would like also to extend my sincere appreciation to my committee Dr. Saad Ragab, Dr. Ken Ball, Dr. Tom Diller, and Dr. Mark Paul. Their constructive comments and great ideas were valuable inputs to this work and they are highly appreciated.

During my study at Virginia Tech, I came across a number of friends who made me love my experience at Virginia Tech, Hugh Hill, Evan Sewall, Anant Shah, Shi-Ming Li, Sai Shrinivas Sreedharan, Naresh Selvarasu, Sunil Patil, Kohei Takamuku, Keagan Delaney, Jose Tijiboy, Amit Amritkar , Jonathan Cowan, and Nagendra Krishnamurthy,. I will not forget the strong discussion and laughs of Pradeep Gopalakrishnan, the most important things in life from Ali Rozati, and the constant support of Aroon Viswanathan. I would like also to thank my dear friend Dr. Imran Akhtar for his support, helpful discussions, and the many rides to the mechanic. I will not forget you guys.

Throughout my stay in Blacksburg, I had the opportunity to meet some exceptional people, whom I respect and became good friends of mine, Jamil Renno, Bashar Hammad, Mazen Arafeh, Mohamed Naguieb, Abdul Haleem Salem, Abdul Salam Gom'a, Adam Daken, Ahmad Sidqi, Sameer Arabasi, Rami Musa, Shadi El-Swaifi, Osama Marzouk, Ahmad Athamneh, Shouib Qudah, Mohannad Sughair, and many dear friends.

I would like also to acknowledge a number of my dear friends, who, although not in Blacksburg, kept on touch along all these years; Saleh Ashagathra, Yousef Qaroush, Mohammad Daqqaq, Abdulaziz Bagabas, and Majed Nassar. Their constant phone calls and emails were of great help.

Last but not least, I would like to thank my brothers, sisters, and my dear mom. Without their endless encouragement and support I would not have been able to finish this degree.

Finally, I just want to say “Mom, I am finally done with school, but not with learning.”

Table of Contents

List of Tables

List of Figures

Chapter 1: Introduction

The science and engineering of air-side heat transfer plays a critical role in the design of compact heat exchangers. Typically, air-side thermal resistance constitutes about 80% of the total thermal resistance to heat flow. Commonly, densely packed fins are used to increase the air-side surface area and also play the dual role of increasing the heat transfer coefficient. This is accomplished by using various topologies such that the thermal boundary layer is constantly regenerated either by interrupted surfaces and/or inducing self sustained flow oscillations. Fins can be broadly categorized into continuous surfaces, e.g. wavy fins and ribbed channels, and interrupted fins, e.g. strip fins and louvered fins. An additional aspect which any design has to be sensitive to is the friction penalty of achieving enhanced heat transfer. Hence, surface topologies which maximize heat transfer augmentation with minimal friction penalty are sought.

This research investigates new fin topologies with heat transfer characteristics that will surpass conventional fin, where the main goals are to increase the heat transfer rate of the fin surface while keeping an acceptable pressure drop penalty. Boundary layer regeneration and enhanced flow mixing are the main techniques through which fins increase the overall Nusselt number of the surface. Surface roughness is usually applied to smooth surfaces to promote flow mixing and initiate turbulence in the flow.

Since spherical indentations or dimples have shown good heat transfer characteristics when used as surface roughness, in this work the employment and modification of dimples/protrusions shape for different heat enhancement applications will be investigated. This dissertation is composed of four standalone papers, three of which have already been published (Chapters 2-4) and the fourth to be submitted to the International Journal of heat and Fluid flow.

Overall, this dissertation can be divided into two parts: Part I which focuses on new fin shapes for compact heat exchangers and Part II which focuses on internal cooling of rotating turbine blades. Part I consists of three phases (Chapters 2-4): Phase I which focuses on dimpled channels, Phase II which investigates a dimpled plate fin, and Phase III which investigates-split dimple fins. On the other hand, Part II of the dissertation focuses on applying dimples and protrusions for internal cooling of rotating turbine blades.

All the simulations conducted in this work are performed using GenIDLEST (Generalized Incompressible Direct and Large Eddy Simulations of Turbulence), which an in-house code developed by Professor Danesh K. Tafti, where the transient generalized continuity, momentum, and energy equations are solved on a non-staggered grid topology, uses second order accurate central differencing for spatial discretization, and a semi-implicit predictor-corrector scheme for time integration. Sub-grid scale turbulence is modeled using the dynamic Smagorinsky model.

The first chapter of this work investigates the application of continuous surfaces with dimples and protrusions on opposite sides for heat augmentation. High fidelity time-dependent calculations are applied to perform an in-depth investigation of the flow structure and heat transfer distribution on a channel with dimples and protrusions on opposite sides. In order to investigate the fin pitch effect on heat transfer and pressure drop of the channel, two channel geometries are tested, Case 1 and Case 2, with the fin pitch of Case 2 half that of Case 1. Detailed investigation of the instantaneous and mean flow structures, turbulent kinetic energy, and heat transfer distribution is provided in chapter 1. This chapter is a paper titled "Investigation of Dimpled Fins for Heat Transfer Enhancement in Compact Heat Exchangers," by Elyyan, M.A., Rozati, A., and Tafti, D.K., published in the International Journal of Heat and Mass Transfer, volume 51, pp. 2950-2966, 2008.

Chapter three of this research investigates the application of dimples as surface roughness elements on plain fin surfaces. Three different dimple geometries are tested, Case 1, 2 and 3, where Cases 1 and 2 vary in the dimple imprint diameter, and Case 3 study the effect of adding a perforation in the dimple cavity. Time dependent calculations covered the laminar to early turbulent flow regime and detailed analysis of the flow structure and heat transfer distribution is performed. This chapter is a paper titled "Flow and Heat Transfer Characteristics of Dimpled Multilouvered Fins," by Elyyan, M.A. and Tafti, D.K., published in the Journal of Enhanced Heat Transfer, volume 16, number 1, pp. 43-60, 2009.

Chapter four introduces a new fin geometry, the split-dimple fin, where a modified dimple shape is used as a surface roughness on plain fin surfaces. Additional boundary layer regeneration, enhanced flow mixing, and reduced recirculation are the main objectives of the split-dimple fin. Detailed analysis of the performance of the split-dimple fin is conducted over a wide range of Reynolds number covering the laminar to fully turbulent flow regime. An in-depth investigation of the flow structure, turbulent statistics, and heat transfer distribution is performed in this study. This chapter is a paper titled “A Novel Split-dimple Interrupted Fin Configuration for Heat Transfer Augmentation,” by Elyyan, M.A. and Tafti, D.K., which has been accepted for publication in the International Journal of Heat and Mass Transfer.

Moving from compact heat exchanger applications, the second part of this research is concerned with internal cooling of turbine blades. Turbine blades are exposed to increasingly high combustion gas temperatures which exceed the melting point of the blade material. Effective cooling of blades is required to maintain an acceptable life span, where relatively cooler bleed air is extracted from the compressor and passed through serpentine passages inside the blade and then ejected onto the blade surface to form a protective layer known as film cooling. Although current surface roughness elements used to enhance heat transfer from internal channels, e.g. ribs and pin fins, provide reasonable heat augmentation levels, the pressure drop penalty can be substantial. In this part, the application of dimpled surfaces for heat enhancement of internal cooling passages in rotating turbine blades is investigated. Simulations covered a wide range of rotation numbers. Coriolis forces effect on the flow structure and heat transfer distribution in the channel is investigated and recommendations on using dimple/protrusion surfaces for heat enhancement in rotating blades are provided. The results of this part will be submitted for publication in the International Journal of Heat and Fluid Flow.

Chapter 2: Investigation of Dimpled Fins for Heat Transfer Enhancement in Compact Heat Exchangers[1]

2.1 Abstract

Direct and Large-Eddy simulations are conducted in a fin bank with dimples and protrusions over a Reynolds number range of Re_H = 200 to 15000, encompassing laminar, transitional and fully turbulent regimes. Two dimple-protrusion geometries are studied in which the same imprint pattern is investigated for two different channel heights or fin pitches, Case 1 with twice the fin pitch of Case 2. The smaller fin pitch configuration (Case 2) develops flow instabilities at Re_H=450, whereas Case 1 undergoes transition at Re_H=900. Case 2, exhibits higher Nusselt numbers and friction coefficients in the low Reynolds number regime before Case 1 transitions to turbulence, after which, the differences between the two decreases considerably in the fully turbulent regime. Vorticity generated within the dimple cavity and at the dimple rim contribute substantially to heat transfer augmentation on the dimple side, whereas flow impingement and acceleration between protrusions contribute substantially on the protrusion side. While friction drag dominates losses in Case 1 at low Reynolds numbers, both form and friction drag contributed equally in Case 2. As the Reynolds number increases to fully turbulent flow, form drag dominates in both cases, contributing about 80% to the total losses. While both geometries are viable and competitive with other augmentation surfaces in the turbulent regime, Case 2 with larger feature sizes with respect to the fin pitch is more appropriate in the low Reynolds number regime Re_H<2000, which makes up most of the operating range of typical compact heat exchangers.

Keywords: Dimples, compact heat exchangers, LES.

---

[1] This chapter is reprinted from the Int. J. Heat Mass Transfer, Vol. 51, "Investigation of Dimpled Fins for Heat Transfer Enhancement in Compact Heat Exchangers," Elyyan, M.A., Rozati, A., and Tafti, D.K., pp. 2950-2966, 2008, with permission from Elsevier.

Nomenclature

D	Dimple imprint diameter
C_f	Fanning friction coefficient
f	non-dimensional frequency based on mean velocity and fin pitch
g^{ij}	Contravariant metric tensor
k	Thermal conductivity
S	Stream-wise pitch
P	Span-wise pitch
H	Channel Height or fin pitch (characteristic length scale)
L_x	Periodic length
$\vec{n}$	Surface normal vector
Nu	Nusselt number
p	Fluctuating, modified or homogenized pressure
Pr	Prandtl number
q''	Constant heat flux on channel walls
Re_τ	Reynolds number based on friction velocity (u_τ)
Re_H	Reynolds number based on mean flow velocity
Q_x	Flow rate in the streamwise direction
t	Non-dimensional time based on u_τ and H
$Time$	Non-dimensional time based on u_b and H
$\vec{u}$	Cartesian velocity vector
u_τ	Friction velocity (characteristic velocity)
u_b	Mean flow velocity
$\vec{x}$	Physical coordinates
β	Mean pressure gradient
δ	Dimple depth
γ	Mean temperature gradient
θ	Fluctuating, modified or homogenized temperature
Ω	Heat transfer surface area

$\vec{\xi}$	Computational coordinates

Subscripts

b	bulk
D_h	based on the hydraulic diameter of the channel
H	based on channel height
o	smooth channel
t	turbulent parameters
τ	values based on friction velocity

Superscripts

+	wall coordinates
*	dimensional quantities

2.2 Introduction

The science and engineering of air-side heat transfer enhancement plays a critical role in the design of compact heat exchangers. Typically, air-side resistance to heat transfer contributes between 80 to 90 percent of the total resistance to heat flow. Commonly, densely packed fins are used to increase the air side surface area and also play the dual role of increasing the heat transfer coefficient. This is accomplished by using various topologies such that the thermal boundary layer is constantly regenerated either by interrupted surfaces and/or inducing self sustained flow oscillations. Wavy fins, offset strip fins, and louvered fins are common examples. An additional aspect which any design has to be sensitive to is the friction penalty of achieving enhanced heat transfer. Hence, surface topologies which maximize heat transfer augmentation with minimal friction penalty are sought.

Recently surfaces imprinted with dimples or concave indentations have been researched extensively. One of the early investigations was conducted by Afansayev *et al.* [1], who investigated the effect of applying shallow dimples ($\delta/D = 0.067$) on flat plates on the overall heat transfer and pressure drop for turbulent flow. Significant heat transfer augmentation (30-40%) at negligible pressure drop augmentation was reported. Since then a number of experimental investigations have been conducted for different dimple geometries yielding heat transfer augmentation factors of about 2-2.5 with low frictional losses compared to other surfaces with flow turbulators [2].

Most experimental studies were conducted in the fully turbulent flow regime; the few low Reynolds number studies conducted were mainly concerned with flow visualization, which showed periodic and continuous shedding of a primary vortex pair from the central portion of the dimple, in addition to a secondary vortex pair shed from the span-wise edges of the dimple (Mahmood *et al.* [3], Ligrani *et al.* [4] and Ligrani *et al.* [5]). Heat transfer distribution and local Nusselt number variation on the dimpled surface showed the existence of a low heat transfer region in the upstream half of the dimple cavity followed by a high heat transfer region in the downstream half. Additional regions of high heat transfer were identified at the downstream rim of the dimple. A number of studies have reported significant heat transfer augmentation at low pressure drop penalty (Mahmood *et al.* [3], Ligrani *et al* [5], Chyu *et al.* [6], Moon *et al.* [7], Burgess and Ligrani [8] and Ekkad and Nasir [9]).

Study of the different geometrical factors resulted in the conclusion that the channel height to dimple imprint diameter ratio (H/D) and the dimple depth to dimple imprint diameter ratio (δ/D) play a significant role in the heat transfer and flow structure inside the domain. Ligrani *et al.* [4] reported that as H/D decreased the secondary flow structures and flow mixing intensified. Nevertheless, Moon *et al.* [7] obtained almost a constant heat augmentation ratio of 2.1 for a dimpled passage with H/D = 0.37, 0.74, 1.11 and 1.49, but their experiments were conducted in the fully turbulent flow regime (Re~12000-60000). Burgess and Ligrani [8] reported that both Nusselt number and friction augmentation increased as (δ/D) increased.

The use of two dimpled surfaces on opposite walls was studied by Borisov *et al.* [10], where highest heat transfer enhancement was reported at $Re \approx 2500$. The use of dimples on rotating channel surfaces has been studied by Griffith *et al.* [11] who reported a heat transfer augmentation of 2.0. The effect of using spherical dimples and protrusions on opposite walls of the channel was studied by Ligrani *et al.* [12] and Mahmood *et al.* [13], where only the dimpled side of the channel was heated. Intensified secondary flow structures, flow unsteadiness and heat transfer augmentation were reported. Moon *et al.* [14] studied the effect of gap clearance in a channel with protrusions only on one side of the channel, where heat distribution showed high heat transfer augmentation at the front of the protrusion and in the passage between protrusions.

Numerical study of the problem of dimpled channel flow was conducted by a number of researchers. Wang et al. [15], using laminar flow simulation, identified a symmetric 3D horseshoe vortex inside a single dimple. Lin *et al.* [16], Isaev and Leont'ev [17], Park *et al.* [18], Won and Ligrani [19] and Park and Ligrani [20] used steady state Reynolds Averaged Navier Stokes (RANS) modeling to study flow and heat transfer in dimpled channel in the turbulent regime. All of the RANS calculations were done in the fully turbulent flow regime. Patrick and Tafti [21] used Direct Numerical Simulations (DNS) and Large-Eddy Simulations (LES) to predict the heat transfer and friction coefficient augmentation in a channel with one dimpled wall at low Reynolds numbers (Re_H = 50 to 2000). Elyyan *et al.* [22] used LES to predict heat transfer and flow structure in a channel with dimples and protrusions on opposite sides for a fully turbulent flow of $\mathrm{Re_H}$ = 15000. Recently, Wang *et al.* [23] used DNS to study turbulent flows over dimpled surfaces in a channel for different dimple depths, diameter and densities. They used a mesh density of 128^3 in resolving 4-16 dimples in a channel.

The objective of this paper is to investigate the low to moderate Reynolds number flow regime typical of compact heat exchangers and beyond into the fully turbulent regime. Most of the experimental work available is in the fully turbulent regime at very high Reynolds numbers. The flow regime in the current paper spans laminar steady, transitional, and turbulent flow. The geometry of interest is a channel with dimples and protrusions on opposite walls which is a realistic representation of dimpled fins in a heat exchanger. The calculations presented here are unique in a number of respects: in extending the state-of-the-art in the application of DNS and LES to complex geometries; in investigating the transitional and low to moderate Reynolds number turbulence regime which has not been studied before for this geometry; and finally leading to an enhanced understanding of heat transfer augmentation over dimpled and protruding surfaces by identifying the spatio-temporal evolution of flow variables and structures.

2.3 Governing Equations and Computational Model

The computational model assumes fully-developed flow and heat transfer and simulates a periodically repeating spatial unit. Both channel walls are heated by imposing a constant heat flux (q''^*) boundary condition. The governing flow and energy equations are non-dimensionalized by a characteristic length scale which is chosen to be the height of the channel or fin pitch (H^*), a characteristic velocity scale given by the friction velocity $u_\tau^* = \sqrt{\Delta \overline{P}_x^* / \rho^*}$, and a characteristic temperature scale given by $q''^* H^* / k$. The assumed periodicity of the domain in the streamwise or x-direction requires that the mean gradients of pressure and temperature be isolated from the fluctuating periodic components as follows:

$$\begin{aligned} P^*(\vec{x},t) &= P_{in}^* - \beta^* x^* + p^*(\vec{x},t) \\ T^*(\vec{x},t) &= T_{in}^* + \gamma^* x^* + \theta^*(\vec{x},t) \end{aligned} \tag{1}$$

On substitution into the Navier-Stokes and energy equations, the *non-dimensional* time-dependent equations in transformed coordinates $\vec{\xi} = \vec{\xi}(\vec{x})$ take the following conservative form[1]:

Continuity:

$$\frac{\partial}{\partial \xi_j}\left(\sqrt{g} U^j\right) = 0 \tag{2}$$

Momentum:

$$\frac{\partial}{\partial t}\left(\sqrt{g} u_i\right) + \frac{\partial}{\partial \xi_j}\left(\sqrt{g} U^j u_i\right) = -\frac{\partial}{\partial \xi_j}\left(\sqrt{g} (\vec{a}^j)_i \, p\right) + \frac{\partial}{\partial \xi_j}\left(\left(\frac{1}{Re_\tau} + \frac{1}{Re_{t_\tau}}\right)\sqrt{g} g^{jk} \frac{\partial u_i}{\partial \xi_k}\right) + \sqrt{g}\beta\delta_{i1} \tag{3}$$

---

[1] Henceforth, all usage is in terms of non-dimensionalized values.

Energy:

$$\frac{\partial}{\partial t}\left(\sqrt{g}\,\theta\right)+\frac{\partial}{\partial \xi_j}\left(\sqrt{g}\,U^{j}\theta\right)=\frac{\partial}{\partial \xi_j}\left(\left(\frac{1}{\mathrm{Pr}\;\mathrm{Re}_{\tau}}+\frac{1}{\mathrm{Pr}_t\;\mathrm{Re}_{t_\tau}}\right)\sqrt{g}\,g^{jk}\,\frac{\partial \theta}{\partial \xi_k}\right)-\sqrt{g}\,\gamma u_1 \tag{4}$$

where $\vec{a}^{i}$ are the contravariant basis vectors[1], $\sqrt{g}$ is the Jacobian of the transformation, g^{ij} are the elements of the contravariant metric tensor, $\sqrt{g}U^{j}=\sqrt{g}\,(\vec{a}^{j})_i u_i$ is the contravariant flux vector, $\bar{u}_i$ is the Cartesian velocity vector, and θ is the modified temperature. The non-dimensional mean pressure gradient β is assumed to be unity, whereas γ is calculated from a global energy balance as: $\gamma = q''\Omega / Re_{\tau}\,Pr\,Q_x L_x$. More details about the modified fully-developed treatment can be found in Zhang *et al.* [24].

Re_{t_τ} is the inverse of the non-dimensional turbulent eddy-viscosity and is modeled by the Smagorinsky model as

$$\frac{1}{\mathrm{Re}_{t_\tau}}=C_s^{\,2}(\sqrt{g})^{2/3}\left|\bar{S}\right| \tag{5}$$

where $|\bar{S}|$ is the magnitude of the resolved strain rate tensor given by $|\bar{S}| = \sqrt{2\bar{S}_{ik}\bar{S}_{ik}}$. The Smagorinsky constant C_s^2 is obtained via the dynamic subgrid stress model [25]. The turbulent Prandtl number is assumed to have a constant value of 0.5 [26].

The governing equations for momentum and energy are discretized with a conservative finite-volume formulation using a second-order central difference scheme on a non-staggered grid topology. The Cartesian velocities, pressure, and temperature are calculated and stored at the cell center, whereas the contravariant fluxes are stored and calculated at the cell faces. A projection method is used for time integration. The temporal advancement is performed in two steps, a predictor step, which calculates an

---

[1] The notation $\left(\vec{a}^{\,j}\right)_k$ is used to denote the *k-th* component of vector $\vec{a}^{\,j}$. $(\vec{a}^{\,j})_k = \partial\xi_j / \partial x_k$

intermediate velocity field, and a corrector step, which calculates the updated velocity at the new time step by satisfying discrete continuity.

The computer program GenIDLEST (Generalized Incompressible Direct and Large-Eddy Simulations of Turbulence) used for these simulations has been applied extensively to study air-side heat transfer augmentation in compact heat exchangers, e.g. Cui and Tafti [27], and in stationary and rotating internal ducts used for cooling gas turbine blades, e.g. Sewall *et al.* [28], and other heat transfer augmentation geometries with very close matches with experiments in the literature. Details about the algorithm, functionality, and capabilities can be found in Tafti [29].

2.4 Calculation of Friction and Heat Transfer Coefficients

Typically the calculations are initiated with some initial guess of the velocity and temperature field under the imposed pressure gradient and integrated in time till the flow and heat transfer adjust to the new conditions and reach a steady state. In the unsteady regime the velocity and temperature fields are integrated further to obtain statistical means. Typical sampling times are 5 to 15 non-dimensional time units. The mean fields are then used to present time-averaged data. All results are non-dimensionalized by the mean flow velocity u_b and fin pitch H.

To characterize the heat transfer, we define a local Nusselt number based on channel height as

$$Nu = \frac{H^* q''^* / (T_s^* - T_{ref}^*)}{k^*} \tag{6}$$

where T_s^* and T_{ref}^* are the dimensional surface temperatures (time mean when unsteady flow) and global reference temperature, respectively. In terms of non-dimensional quantities the above can be re-written as

$$Nu = \frac{1}{\theta_s - \theta_{ref}} \tag{7}$$

where θ_s is the local modified non-dimensional surface temperature and θ_{ref} is the reference modified non-dimensional temperature defined as:

$$\theta_{ref} = \frac{\iint |u| \theta dA_x}{\iint |u| dA_x} \tag{8}$$

The surface-averaged Nusselt number is obtained by integration over the protrusion and dimple surface as:

$$Nu = \frac{\iint \quad dS}{\iint (\theta - \theta_{ref})dS} \tag{9}$$

where S denotes the heat transfer surface.

The Fanning friction coefficient C_f is calculated as:

$$C_f = \frac{(\overline{\Delta p}^* / L_x^*)(D_h^*)}{2\rho \cdot u_b^{*2}} \tag{10}$$

After substituting the non-dimensional value of $\overline{\Delta p} / L_x$ as unity, the expression reduces to

$$C_f = \frac{D_h}{2u_b^2} \tag{11}$$

where u_b is the bulk mean flow velocity obtained from the simulation under the condition of the applied mean pressure gradient of unity. D_h is the hydraulic diameter and its usual definition yields D_h=1.8263 for both cases[1].

The heat transfer and friction augmentation ratios are calculated based on baseline values. In the present study, the laminar Fanning friction coefficient and Nusselt number for flow between smooth parallel plates and the Petukhov and Gnielinski correlations for turbulent flow are used to calculate the baseline Fanning friction coefficient and Nusselt number, respectively [30]. The choice of correlations was made based on their validity and accuracy over the range of Reynolds numbers of interest in this study. The friction coefficient and Nusselt number for these correlations based on Re_H are as follows:

---

[1] For a plain channel, D_h=2. However, the dimple and protrusion increase the wetted perimeter by a factor of 1.095 for both cases.

$$C_{f_0} = \frac{12}{Re_H} \qquad ;Re_H < 1500$$

$$C_{f_0} = (1.580 \ln Re_H - 2.185)^{-2} \qquad ;1500 \le Re_H \le 2.5\times10^6$$

$$Nu_0 = \frac{hH}{k} = 4.12 \qquad ;Re_H < 1500$$

$$Nu_0 = \frac{(C_{f_0}/2)(Re_H - 500)Pr}{1+12.7(C_{f_0}/2)^{1/2}(Pr^{2/3}-1)} \qquad ;1500 \le Re_H \le 2.5\times10^6 \tag{12}$$

Although the original forms of the equations are in terms of Re_{Dh}, they are rewritten here in terms of Re_H assuming that for a smooth channel $D_h^* = 2H^*$.

2.5 Fin Geometry

The fin geometry consists of two parallel plates with staggered dimples and protrusions on opposite walls without any offset with respect to each other, as shown in Figure 2.1-a. Table 2.1 summarizes the two geometries tested. In Case 1, the non-dimensional span-wise and stream-wise pitches are $P=S=1.62$, and the dimple imprint diameter, D=1.0, with dimple depth, δ=0.2. In Case 2, all the dimple dimensions are doubled with respect to the fin pitch or channel height. Physically, this is representative of a scenario in which the dimensional fin pitch is decreased by a factor of two while keeping the physical dimensions of the dimple imprint geometry the same or conversely keeping the fin pitch the same and increasing the dimple dimensions by a factor of two. Case 2 matches the experimental set up of Mahmood *et al.* [13].

2.6 Domain size and grid resolution

Under the assumption of fully-developed flow and heat transfer, it is desirable to choose the smallest repetitive unit as the computational domain to minimize the computational cost. Moreover, the selected computational domain should be capable of capturing all the relevant physical modes in the solution. If the imposed periodicity is too small a spatial domain, the important modes pertinent to the solution will not be captured. To investigate the trade-off between computational cost and accuracy, an initial study is conducted to investigate the effect of domain size on the solution. The smallest periodic domain which can be constructed is Domain 1 ($1\times P/2\times S$) as shown in Figure 2.1-b, whereas Domain 2 ($1 \times P \times S$) and Domain 3 ($1 \times P/2 \times 2S$) admit lower wave number solutions in the stream-wise and span-wise directions. The domains and grid sizes with friction and heat transfer augmentation results are summarized in Table 2.2 at Re_H=3,700 for Case 1.

The results in Table 2.2 show a difference of less than 3% between Domain 1 and 2 and less than 5.6% between domain 1 and 3, in time-averaged Nusselt number and friction coefficient augmentations and hence Domain 1 was deemed adequate to accurately represent the physics of the flow and heat transfer.

A hybrid structured/unstructured multi-block grid is used to discretize the computational domain with a total mesh resolution of approximately 933 thousand computational cells for Case 1 and 1.6 million cells for Case 2. The grid is designed such that maximum resolution is provided in the dimple (protrusion), and in the vicinity of the top and bottom surfaces. In the wall normal direction the first grid point is placed at $\Delta \approx 6.5 \times 10^{-4}$ near the two channel walls. An *a-posteriori* calculation of the local friction velocity for Case 2 at the highest Reynolds number showed that the condition $y^+_1 < 1$ is satisfied throughout on both surfaces [22]. In addition, surface averaged values of the wall parallel distribution is $\Delta^+_{//} \approx 15$ at the highest Reynolds number simulated.

In the two geometries, the laminar to unsteady laminar regimes are treated in a direct simulation mode without any subgrid model. The LES model is only activated after the flow tends towards a chaotic turbulence like regime which for Case 1 is at Re_H=1000 and for Case 2 at Re_H=700. It is noted that the dynamic model calculates a physically correct eddy-viscosity based on the grid resolution and the turbulence length scales present in the flow. From previous calculations on similar mesh resolutions for a dimpled channel [31], the subgrid modeling is expected to have a negligible effect on mean heat transfer and friction at least up to Re_H =2000.

2.7 Validation

For the purposes of this study, a calculation was conducted to compare with the experimental data of Mahmood *et al.* [13]. The experimental setup was similar to Case 2 with the exception that only the dimpled surface was heated. To replicate the experimental conditions, a constant heat flux boundary condition is applied to the dimpled surface and an adiabatic wall boundary condition is applied to the protrusion surface in the calculation. The Reynolds number based on the channel height, Re_H, is 14600. Table 2.3 summarizes the comparisons. While the Nusselt number augmentation shows excellent agreement with experiments, the augmentation of C_f is more than twice the value reported by Mahmood *et al.* [13]. To further investigate this discrepancy, a calculation was conducted for a channel with dimples on one side and a smooth wall on the other at Re_H=8160. The Nusselt number augmentation obtained by the calculation (Nu/Nu_o=1.69) compared well with the experimental value of (Nu/Nu_o=1.83) reported by Mahmood *et al.* [13] at Re_H=10200. The predicted friction coefficient augmentation of C_f/C_{fo}=2.67, on the other hand, was much higher than the value of 1.50 reported in [13]. The good match in Nusselt number augmentation ratio but the large irreconcilable difference in friction augmentation is puzzling. The same computational techniques have been used in ribbed duct flows to obtain friction augmentation in very close agreement with experiments [28]. Additionally, computations in turbulent channel flow at Re_H=5600 show excellent agreement with friction and Nusselt number correlations (within 5-10%) [22].

2.8 Results and Discussion

2.8.1 Laminar Flow and Transition to Turbulence

This section describes the typical mean flow features in the laminar regime and the transition to turbulence. For the two geometries investigated, Case 1 and Case 2, Figure 2.2 plots 3-D streamlines injected near the dimple and protrusion surfaces at nominal Re_H=250. In both cases the flow is laminar at this Reynolds number. At the dimpled surface the flow accelerates as it approaches the upstream edge of the dimple where it separates forming a recirculating zone in the dimple. The recirculating zone extends to the downstream edge of the dimple where the separated shear layer reattaches. Upon reattachment, the flow accelerates upward along the downstream rim of the dimple. Part of the recirculating flow, as it traverses the side of the dimple, decelerates, loses momentum and is ejected along the side rims. On the other side of the channel, the flow accelerates around and on the protrusion. The flow on the protrusions accelerates up to an angle of 70-80 degrees after which it decelerates up to 180 degrees; at low Reynolds number no separation in the wake is observed.

To identify the coherent vorticity in the present study, the vortex eduction technique proposed by Chong *et al.* [33]. In this method, in regions dominated by vortical motion, the velocity gradient tensor exhibits two eigen values which are complex conjugates. The magnitude of the eigenvalue is indicative of the strength of the vortex. The structures identified by this method are referred to as "coherent vorticity" in this paper, and the magnitude of the eigenvalue as the strength of the coherent vortices.

Figure 2.3 shows isosurfaces of coherent vorticity near the dimple and protrusion surface as a function of Reynolds number, and the corresponding velocity traces near the surface on the flat landing downstream of the dimple and in the wake of the protrusions. The beginning of transition to turbulence is signaled by the break in symmetry of the three-dimensional vorticity. On the dimple, coherent vorticity is generated at the upstream and downstream rims, which is mostly the agglomeration of spanwise or z-directional vorticity. On the protrusion side, the calculated coherent vorticity is concentrated between protrusions, and at the leading side of the protrusion in regions of high flow acceleration. In Case 1, a slight asymmetry is observed as early as Re_H=530 on the protrusion side of the channel (not shown). However, the developing instability is not reflected in the velocity signal in the wake of the protrusion. At Re_H=790, the asymmetry gets stronger and the velocity in the wake of the protrusion and immediately downstream of the dimple show a periodic fluctuation. This is in spite of the fact that the coherent vorticity distribution at the dimple shows no visible asymmetry. Hence it is concluded that for Case 1, the asymmetry which eventually leads to transition to turbulence develops in the wake of the protrusions and spreads to the rest of the domain. By Re_H=990, the asymmetry spreads to the dimples as well and the flow is well into the transitional regime with highly fluctuating and somewhat intermittent signal.

For Case 2, the structure of coherent vorticity is noticeably different in the dimple (Figure 2.4). In this case, the initial asymmetry in the flow appears earlier in the dimple. This is inferred from the signal downstream of the dimple on the flat landing at Re_H=440, which exhibits a sinusoidal low amplitude variation, although no visible asymmetries are found in the vorticity distribution on both sides. By Re_H=480, the flow on both sides exhibits a chaotic structure. Hence, Case II with a larger dimple depth and imprint diameter transitions much earlier than Case-I. However the transition to turbulence is more gradual and is not as sharp as that observed in Case 1.

2.8.2 Turbulent Flow Regime

In the fully turbulent regime (Re_H=15000), Figure 2.5, the mean flow streamlines show the existence of two vortical structures, which together form the recirculation region inside the dimple cavity. These recirculation zones are symmetrical about the dimple center-plane and the core of each structure is located in the upstream half of the dimple. As the flow Reynolds number increases the size of the recirculation zone shrinks; this is due to early reattachment of the flow as the separated shear layer becomes more turbulent. Between the two cases, Case 2 has a noticeably smaller reattachment length. It is observed that as the flow ejects from the dimple, the rim curvature induces helicity to the mean streamlines around the downstream rim of the dimple, which manifests instantaneous helical vortices shed from the rim. On the protrusion, the flow accelerates on the leading face and on deceleration leads to three-dimensional separation with a highly unsteady wake. The boundary layer on the protrusion separates earlier in Case-1. Additionally, another small recirculation region just upstream of the protrusion can be identified as the flow slows down before it impinges on the front of the protrusion.

2.8.3 Coherent vorticity structure and magnitude

Coherent vortical structures and dynamics play an important role in heat transfer enhancement [32]. A single-valued isosurface (value 10) of coherent vorticity is shown in

Figure 2.6 for nominal Re_H=1400 on the dimple and protrusion side of the channel. Comparing the density of the educed structures between Case 1 and 2, it is evident that Case 2 contains more turbulent eddies than does Case 1, particularly on the dimple side of the channel. Although difficult to decipher in these snapshots, vorticity shed from the separated shear layer in the dimple is ejected out from the reattachment region in the dimple cavity. On ejection, the vortices are stretched and tilted in the stream-wise direction as they come in contact with the mainstream flow and are transported in the close vicinity of the flat landing downstream of the dimple. Additional vorticity is also generated as the flow ejects out over the side and downstream rims of the dimple cavity. On the protrusion side of the channel, vorticity is mainly shed from the separated shear layers which form the wake vortices. These observations on the flow dynamics in the dimple cavity generally agree with the flow visualization observations made by Won *et al.* [34].

As the Reynolds number increases and the flow becomes more turbulent, the magnitude of the coherent vorticity also increases. Since the coherent vorticity in the domain is closely linked to the level of heat transfer enhancement [32], it is useful to find a means of quantifying the variation of the coherent vorticity with Reynolds number in the calculation domain. This is done by defining a volume-weighted time-averaged coherent vorticity (Ψ) in the domain, which is calculated by finding the time-mean of the instantaneous coherent vorticity and then finding the volume average of that quantity over the whole calculation domain. This is plotted in

Figure 2.6–c and shows that the time-mean volume-averaged coherent vorticity increases with Reynolds number and that it is higher in Case 2 than in Case 1 up to a Reynolds number of 2000, after which both geometries exhibit very similar magnitudes. For Case 1, there is a sharp increase in coherent vorticity as the flow transitions to turbulence, whereas Case 2 exhibits higher values for $Re_H<1000$, which increase gradually as the flow Reynolds number increases.

2.8.4 Turbulent kinetic energy and turbulent statistics

Figure 2.7 shows the Turbulent Kinetic Energy (TKE) normalized by the square of the mean velocity, at a span-wise plane located at 0.2 D downstream of the edge of the dimple and a stream-wise plane at the centerline of the dimple/protrusion. Regions of high TKE values are observed:

- In the separated shear layer in the dimple where the mainstream flow and recirculation region interact.
- Close to the flat landing downstream of the dimple, due to the reattachment of the small scale vortices ejected from the dimple cavity.
- In the wake of the protrusion.

While Case 1 exhibits slightly higher levels of TKE in the wake of the protrusion (possibly a result of the smaller wake region in Case 2), the TKE levels on the dimple side are noticeably higher for Case 2 in the separated shear layer and at the flat landing behind the dimple. This is attributed to the larger dimple depth and the more intense vorticity generated in the dimple cavity.

Figure 2.8 shows the effect of Reynolds number on the TKE profile at a span-wise center plane through the dimple located at 0.2 D downstream of the edge of the dimple/protrusion. Two major conclusions can be made from these profiles, which are; i) There is a large increase in TKE levels near the respective channel surfaces in the wake of the protrusion and on the flat landing behind the dimple as the Reynolds number increases beyond $Re_H \approx 1400$. The shift in the location of the peak value of TKE on the protrusion side is a result of early separation at low Reynolds numbers which displaces the wake away from the surface. Between Re_H=9000 and 15000, the normalized profiles of TKE are quite similar indicating no change in the turbulent structure of the flow. ii) As observed earlier, the TKE level near the flat landing for Case 2 is substantially higher than Case 1. However, there is no substantial difference between the two cases on the protrusion side, indicating that the increased depth of the protrusion does not have any effect on the wake structure, whereas the increased depth of the dimple produces more turbulence.

Figure 2.8-c shows the variation of volume averaged TKE with Reynolds number much like the volume averaged coherent vorticity plotted in

Figure 2.6-c. It is observed that Case 2 exhibits higher values than Case 1 over the full range of Reynolds numbers. However, it is noteworthy that while the normalized TKE asymptotes to a near constant value after Re_H=4000 for Case 1 and Re_H=2000 for Case 2, the normalized coherent vorticity keeps increasing with Reynolds number, which as will be shown later correlates much better with the Nusselt number variation.

Figure 2.9 shows representative component RMS profiles of the fluctuating velocities for Case 2 at the same location as that in Figure 2.8. Near the walls on the dimple side, the turbulent energy is dominated by the U_{rms} component, which results from the streamwise fluctuations produced by the small scale vorticity ejected from the dimple as well as that produced by the shear layer around the rim of the dimple. On the protrusion side, turbulent energy is highest in the W_{rms} component, which is a result of the highly unsteady lateral entrainment into the low pressure wake behind the protrusion.

The three components exhibit isotropy in the middle half of the channel but strong anisotropies are present in the distributions near the surfaces.

2.8.5 Friction Characteristics

Both friction drag and form or pressure drag contribute to the overall frictional losses. Figure 2.10–a shows the contribution of form drag and friction drag to the total drag in the channel as a function of Reynolds number for both geometries. In the laminar regime, the pressure differential across the protrusion is small in the absence of separation. In the dimple cavity, the pressure differential between the fore and aft side of the dimple is also small. Hence, at low Reynolds numbers the shear or surface friction dominates the total losses. As the Reynolds number increases and flow separation and wake formation on the protrusion and separation and reattachment within the dimple intensify, form losses start dominating over surface friction. The trend is present in both geometries, except that the transition from a friction dominated pressure drop to a form dominated one occurs much earlier in Case 2 (Re_H=400) than in Case 1 (Re_H=1200) and seems to be correlated to the onset of unsteadiness in the two geometries. At Reynolds numbers above 10000, the percentage form and friction drag asymptote to a near 80-20 split.

Figure 2.10–b shows a further breakdown of the percentage contribution of form and friction drag on the dimple and protrusion surfaces for the two cases. The protrusion surface exhibits a distinct cross-over between form and friction drag at Re_H =1500-2000 for both cases. The dimple surface, on the other hand, behaves differently. Whereas Case 1 shows the crossover at Re_H=1000, the crossover for Case 2 occurs at a much lower Reynolds number. These observations lead to the conclusion that the losses on the dimpled surface are much more dependent on the onset of unsteadiness than the surface with protrusions. It is also noted that in both cases, form losses on the dimple surface are larger than form losses on the surface with protrusions. While form losses on the protrusion surface assume fairly constant values beyond Re_H=5000, the corresponding form losses on the dimple side exhibit a steady increase with Reynolds number. This can be explained by postulating that the protrusion wake dynamics (scaled by ρu_b^2) becomes

Reynolds number independent much quicker than the dynamics of separation and reattachment in the dimple, which is the primary contributor to form losses in the dimple. In fact, the asymptotic nature of form drag with Reynolds number agrees with the constancy of drag coefficients for flow over bluff bodies. While the percentage form drag on the dimple side is larger in Case 2 than in Case 1, it is noteworthy that on the protrusion side, Case 1 exhibits a higher percentage form contribution to the total drag, in spite of a larger protrusion in Case 2. This can be attributed to the formation of a smaller wake in Case 2 (see Figure 2.5).

Figure 2.10-c shows the variation of the friction coefficient and its augmentation over a smooth plain channel with Reynolds number. Case 2 exhibits higher friction coefficients at low to moderate Reynolds numbers in the laminar and early turbulence regime but on the onset of turbulent flow in Case 1, the two friction coefficients are comparable to each other. A striking feature of Case 2 is that there is no well defined transition from laminar to turbulent flow in the friction coefficient, much like the variation in the time-mean volume averaged coherent vorticity (Ψ) in Figure 2.6–c. Rather the friction coefficient behaves much like that in a turbulent flow even at low Reynolds numbers. This behavior is consistent with observations on the onset of instabilities which occur as early as Re_H=440, but which develop much more gradually than Case 1. On the other hand Case 1 exhibits a classical shape with a distinct laminar region followed by transition and a fully turbulent region. Up to a Re_H=1000, C_f in Case 1 behaves much like that in a plain channel flow with augmentation ratios ranging from 1 to 1.4, which increases to about 5.5 at Re_H=10000.

2.8.6 Heat transfer characteristics

Figure 2.11 shows the Nusselt number augmentation distribution on the dimple and protrusion surfaces for laminar flow at nominal Re_H=250 and turbulent flow at nominal Re_H=15000. At Re_H=250 on the protrusion side, the heat transfer coefficient attains a maximum at the apex of the protrusion for Case 1, where the flow reaches its maximum velocity as it accelerates on the front half of the protrusion. For Case 2, the region of augmentation spreads to the sides of the protrusion due to the larger flow acceleration experienced between adjacent protrusions. At the same time, the flat landing in the wake of the protrusion exhibits a more pronounced deterioration in the Nusselt number for Case 2. On the dimple side, Case 2 shows higher overall heat transfer augmentation within the dimple cavity, because of the smaller recirculation region.

Larger augmentation is also noticed on the flat landing downstream of the dimple, which is influenced by the stronger flow ejection out of the deeper cavity.

The augmentation pattern on the dimple side remains the same as the Reynolds number increases to $Re_H \approx 15{,}000$; but changes considerably on the protrusion side. The maximum augmentation shifts to the fore-sides of the protrusion as the bulk of the flow now accelerates around the sides of the protrusions. An additional zone of high augmentation is found in the wake of protrusion where the separated shear layer on the protrusion comes in the proximity of the flat landing. Regions of low heat transfer are observed on the flat landing in front of the protrusion due to the development of secondary recirculation regions. Whereas Case 1 has a higher heat transfer augmentation on the protrusion side compared to Case 2, the opposite trend is observed on the dimple side. Within the dimple cavity, regions of low heat transfer shrink considerably as the flow becomes turbulent. For Case 2 at $Re_H \approx 15{,}000$ a small zone of low heat transfer appears along the downstream rim of the dimple as a result of the recirculation region that forms as the flow ejects out of the dimple cavity. The heat transfer augmentation reaches another maximum as the flow reattaches to the fin surface at the flat landing downstream of the dimple.

Figure 2.12 plots the variation of area-weighted time-averaged Nusselt number with Reynolds number. Case 2 clearly shows higher heat transfer coefficients up to $Re_H=1000$. The higher Nusselt numbers is a result of the earlier onset of unsteadiness in Case 2 combined with the more intense flow impingement and acceleration on the protrusion. In this range, Case 1 shows little or no augmentation till the flow develops instabilities and transitions to turbulence. It is clear from these results that between the two geometries, Case 2 is more viable for heat transfer augmentation in the low Reynolds number range less than $Re_H=2000$. The augmentation ratio peaks at 3.5 at $Re_H=1200$-1500 for Case 2 and at 2.8 for Case 1 after which it decreases with the use of turbulent baseline values for normalization. As the flow reaches a fully turbulent state both geometries exhibit similar Nusselt number values (augmentation ratios between 2.3-2.5). This agrees with the experimental results reported by Moon *et al.* [7], where the Nusselt number augmentation exhibited a near constant value over $0.37 \leq H/D \leq 1.49$ in the fully turbulent regime.

A clear correlation exists between the time-mean volume averaged coherent vorticty plotted in

Figure 2.6, and the overall Nusselt number, Figure 2.12. At low Reynolds numbers before transition, Case 1 exhibits a near constant magnitude of normalized vorticity which correlates with the near constant Nusselt number. In this range both vorticity and Nusselt number are higher in Case 2 than in Case 1. As the Reynolds number increases into the turbulent regime, the Nusselt numbers and coherent vorticity approach each other for the two cases but increase with Reynolds number. On the other hand, as mentioned earlier, normalized TKE not only approaches a near constant value in the turbulent regime but also remains higher in Case 2, unlike the trend in Nusselt number. This leads to the conclusion that trends in coherent vorticity magnitude is a better indicator of trends in heat transfer augmentation than turbulent kinetic energy.

2.9 Summary and Conclusions

Direct and Large-Eddy Simulations are conducted in a channel with dimples and protrusions which is a realistic representation of finned compact heat exchangers. The Reynolds number range covers laminar, transitional and fully turbulent regimes. The same imprint pattern is investigated for two different fin pitches, Case 1 with twice the fin pitch of Case 2.

It is established that Case 1 provides little or no augmentation in the steady laminar flow regime up to a $Re_H=900$ before the flow transitions to turbulence. Case 2 on the other hand, provides some augmentation in the laminar steady regime which lasts up to a $Re_H=450$. As a consequence in the low Reynolds number regime $Re_H<1000$, Case 2 exhibits superior augmentation properties. However, once the flow becomes turbulent in Case 1, there is no substantial difference between the two geometries after $Re_H=3000$. Investigating the dynamics of heat transfer augmentation it was found that augmentation on the dimpled surface was chiefly brought about by vortex impingement in the reattachment region of the cavity. The ejection and redirection of these vortices and additional vortex shedding at the rim of the dimple was responsible for the high augmentation on the flat landing. On the protrusion side, flow impingement and acceleration between protrusions played an important role in augmenting heat transfer. Based on the variation of coherent vorticity with Reynolds number, it was concluded that the magnitude of volume weighted time-averaged coherent vorticity correlated better with Nusselt number than did the volume averaged turbulent kinetic energy.

At low Reynolds number, Case 2 exhibited much higher friction losses than Case 1, but the difference decreased considerably in the fully turbulent regime. While friction drag dominated losses in Case 1 at low Reynolds numbers, both form and friction contributed equally in Case 2. As the Reynolds number increased to fully turbulent flow, form drag dominated in both cases contributing about 80% to the total losses. Unexpectedly, in Case 2, the dimple surface contributed about 70% of the total form drag.

In conclusion, the dimple/protrusion combination as a heat transfer enhancement surface produced mixed results. While both geometries are viable and competitive with other augmentation surfaces such as ribs in the turbulent regime, Case 2 with the smaller fin pitch is more appropriate in the low Reynolds number regime Re_H<2000, which makes up most of the operating range of typical compact heat exchangers.

2.10 Acknowledgments

This work is a result of support provided by the US Army RDECOM, Fort Belvoir, VA and Modine Manufacturing Co., Passenger Thermal Management, Racine, WI for air-side heat transfer enhancement in next generation compact heat exchangers. The support is gratefully acknowledged. The calculations were performed on Virginia Tech's Terascale computing facility, System-X.

2.11 References

[1] V.N., Afanasyev, Ya.P., Chudnovsky, A.I., Leontiev, P.S., Roganov, Turbulent flow friction and heat transfer characteristics for spherical cavities on a flat plate, Experimental Thermal and Fluid Science 7 (1) (1993) 1-8.

[2] P.M., Ligrani, M.M., Oliveira, T., Blaskovich, Comparison of heat transfer augmentation techniques, AIAA journal 41 (3) (2003) 337-362.

[3] G.I., Mahmood, M.L., Hill, D.L., Nelson, P.M., Ligrani, P.M., Local heat transfer and flow structure on and above a dimpled surface in a channel, ASME Paper No. 2000-GT-230.

[4] P.M., Ligrani, J.L., Harrison, G.I., Mahmood, M.L., Hill, Flow structure due to dimple depressions on a channel surface, Physics of fluids 13 (11) (2001) 3442-3451.

[5] P.M., Ligrani, N., Burgess, S., Won, Nusselt numbers and flow structure on and above a shallow dimpled surface within a channel including effects of inlet turbulence intensity level, J. of Turbomachinery 127 (2005) 321-330.

[6] M.K., Chyu, Y., Yu, H., Ding, J.P., Downs, F.O., Soechting, Concavity enhanced heat transfer in an internal cooling passage, ASME Paper No. 97-GT-437.

[7] H.K., Moon, T.O., O'Connell, B., Glezer, Channel height effect on heat transfer and friction in a dimpled passage, Journal of Engineering for Gas Turbine and Power 122 (2) (2000) 307-313.

[8] N.K., Burgess, P.M., Ligrani, Effects of dimple depth on Nusselt numbers and friction factors for internal cooling channel, ASME Paper No. GT2004-54232.

[9] S., Ekkad, H., Nasir, Dimple enhanced heat transfer in high aspect ratio channels, J. of Enhanced Heat Transfer 10 (4) (2003) 395-405.

[10] A.K., Borisov, S., Kobzar, B., Glezer, Comparison of thermo-hydraulic characteristics for two types of dimpled surfaces, ASME Paper No. GT2004-54204.

[11] T., Griffith, L., Al-Hadhrami, L., J.C., Han, Heat transfer in rotating rectangular cooling channels (AR=4) with dimples, J. of Turbomachinary 125 (3) (2003) 555 – 563.

[12] P.M., Ligrani, G.I., Mahmood, J.L., Harrison, C.M., Clayton, D.L., Nelson, Flow structure and local Nusselt number variation in a channel with dimples and protrusions on opposite walls, Int. J. Heat Mass Transfer 44 (2001) 4413-4425.

[13] G.I., Mahmood, M.Z., Sabbagh, P.M., Ligrani, Heat transfer in a channel with dimples and protrusions on opposite walls, J. Thermophysics and Heat Transfer 15 (3) (2001) 275-283.

[14] H.K., Moon, T., O'Connel, R., Sharma, Heat transfer enhancement using a convex-patterned surface, J. Turbomachinery 125 (2) (2003) 274-280.

[15] Z., Wang, K.Z., Yeo, B.C., Khoo, Numerical simulation of laminar channel flow over dimpled surface, AIAA Paper No. AIAA 2003-3964.

[16] Y.L., Lin, T.I-P., Shih, M.K., Chyu, Computations of flow and heat transfer in a channel with rows of hemispherical cavities, ASME Paper No. 99-GT-263.

[17] S.A., Isaev, A.I., Leont'ev, Numerical simulation of vortex enhancement of heat transfer under conditions of turbulent flow past a spherical dimple on the wall of a narrow channel, High Temperature 41 (5) (2003) 655-679.

[18] J., Park, P.R., Desam, P.M., Ligrani, Numerical predictions of flow structure above a dimpled surface in a channel, Numerical Heat Transfer A 45 (1) (2004) 1-20.

[19] S., Won, P., Ligrani, P.M., Numerical predictions of flow structure and local Nusselt number ratios along and above dimpled surfaces with different dimple depths in a channel, Numerical Heat Transfer A 46 (6) (2004) 549-570.

[20] J., Park, P.M., Ligrani, P. M., Numerical predictions of heat transfer and fluid flow characteristics for seven different dimpled surfaces in a channel, Numerical Heat Transfer A 47 (3) (2005) 209-232.

[21] W.V., Patrick, D.K., Tafti, D.K., Computations of flow structures and heat transfer in a dimpled channel at low to moderate reynolds number, ASME Paper No. HT-FED2004-56171.

[22] M. Elyyan, A., Rozati, D.K., Tafti, Study of flow structures and heat transfer in parallel fins with dimples and protrusions using large eddy simulation, ASME Paper No. FEDSM2006-98113.

[23] Z., Wang, K.S., Yeo, B.C., Khoo, DNS of low Reynolds number turbulent flows in dimpled channels, Journal of Turbulence 7 (37) (2006) 1-31. .

[24] L. Zhang, D.K., Tafti, F., Najjar, S., Balachander, Computations of flow and heat transfer in parallel-plate fin heat exchangers on the CM-5: effects of flow unsteadiness and three-dimensionality, Int. J. Heat Mass Transfer 40 (66) (1997) 1325-1341.

[25] M. Germano, U., Piomelli, P., Moin, W.H., Cabot, A dynamic subgrid-scale eddy viscosity model, Phys. Fluids 3 (1991) 1760-1765.

[26] P., Moin, K., Squires, W., Cabot, S., Lee, A dynamic sub-grid-scale model for compressible turbulence and scalar transport, Phys. Fluids A 3 (11) (1991) 2746-2757.

[27] J., Cui, D.K.,Tafti, D. K., Computations of flow and heat transfer in a three-dimensional multilouvered fin geometry, Int. J. Heat Mass Transfer 45 (2002) 5007-5023.

[28] E.A., Sewall, D.K., Tafti, A.B., Graham, K.A., Thole, Experimental validation of large eddy simulation of flow and heat transfer in a stationary ribbed duct, Int. J. Heat and Fluid Flow 27 (2) (2006) 243-258.

[29] D.K., Tafti, GenIDLEST – A scalable parallel computational tool for simulating complex turbulent flows, Proc. ASME Fluids Engineering Division-*FED* 256 (2001) 357-346..

[30] F.P., Incropera, D.P., and DeWitt, Fundamentals of Heat and Mass Transfer, fifth ed., Wiley, New York, 1996, pp. 463-493.

[31] W.V., Patrick, Computations of flow structure and heat transfer in a dimpled channel at low to moderate Reynolds number, Master's thesis, Virginia Tech, VA, 2005.

[32] D.K., Tafti, J. Cui, Fin tube junction effects on flow and heat transfer in flat tube multilouvered heat exchangers, Int. J. Heat Mass Transfer 45 (25) (2002) 5007-5023.

[33] M., Chong, A., Perry, B.J., Cantwell, A general classification of three-dimensional flow fields, Physics of Fluids A 2 (1990) 765-777.

[34] S.Y., Won, Q., Zhang, P.M., Ligrani, Comparisons of flow structure above dimpled surface with different dimple depths in a channel, Physics of Fluids 17 (4) (2005) 045105.

Table 2.1: Non-dimensional Geometry Specifications

	$H=H^*/H^*$	**$D=D^*/H^*$**	**$\delta=\delta^*/H^*$**	**$P=P^*/H^*$**	**$S=S^*/H^*$**
Case 1	1.0	1.0	0.2	1.62	1.62
Case 2	1.0	2.0	0.4	3.24	3.24

Table 2.2: Effect of domain size on solution

Domain	**1**	**2**	**3**
Dimensions	$1\times P/2\times S$	$1\times P\times S$	$1\times P/2\times 2S$
# of cells	933,888	1,867,776	1,867,776
Re_H	3735	3714	3826
Nu/Nu_0	2.72	2.67	2.57
%Difference	***Reference***	1.5	5.55
C_f/C_{fo}	4.87	4.94	4.70
%Difference	***Reference***	1.5	3.5

Table 2.3: Comparison between numerical and experimental results

	Re_H	**Nu/Nu_0**	**C_f/C_{fo}**
Present study	14600	2.31	6.36
Experimental [13]	15000	2.23	3.08

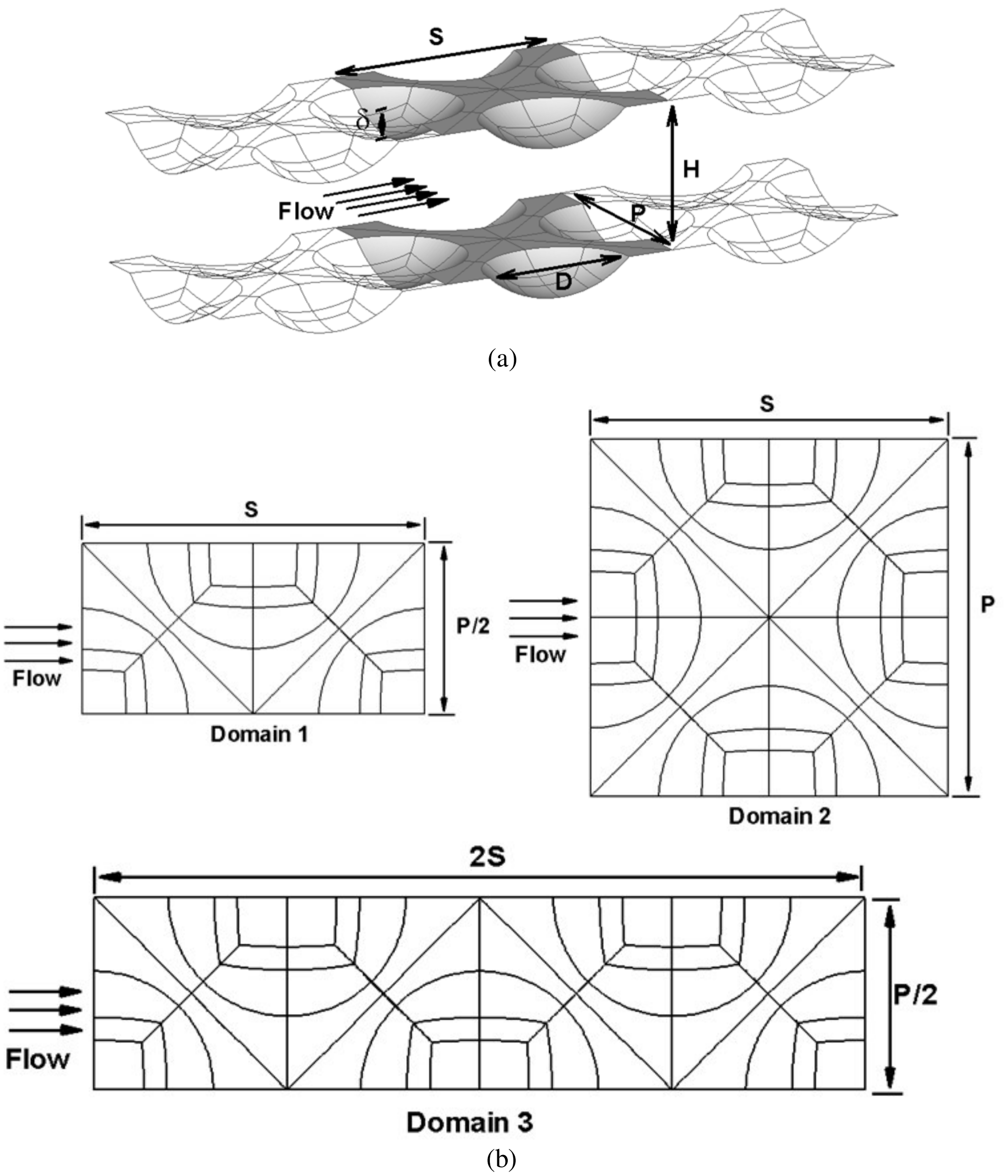

Figure 2.1: a) Dimpled channel Geometry; b) Different computational domain sizes: domain 1, 2 and 3

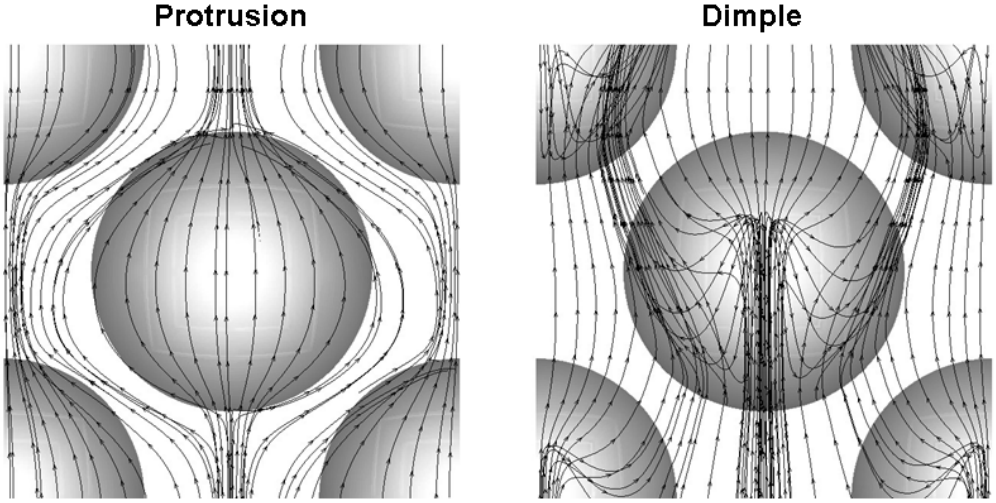

Case 1

(a)

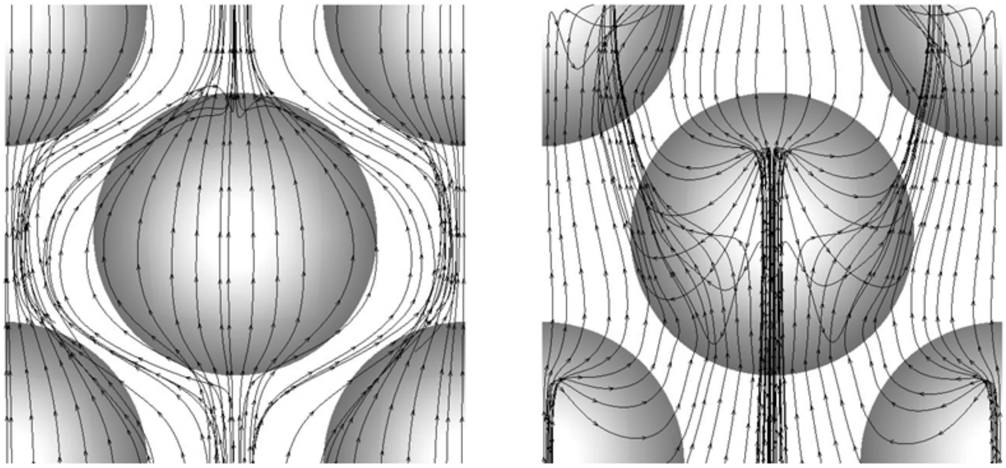

Case 2

(b)

Figure 2.2: Mean 3D velocity streamlines in laminar flow at nominal Re_H of 250

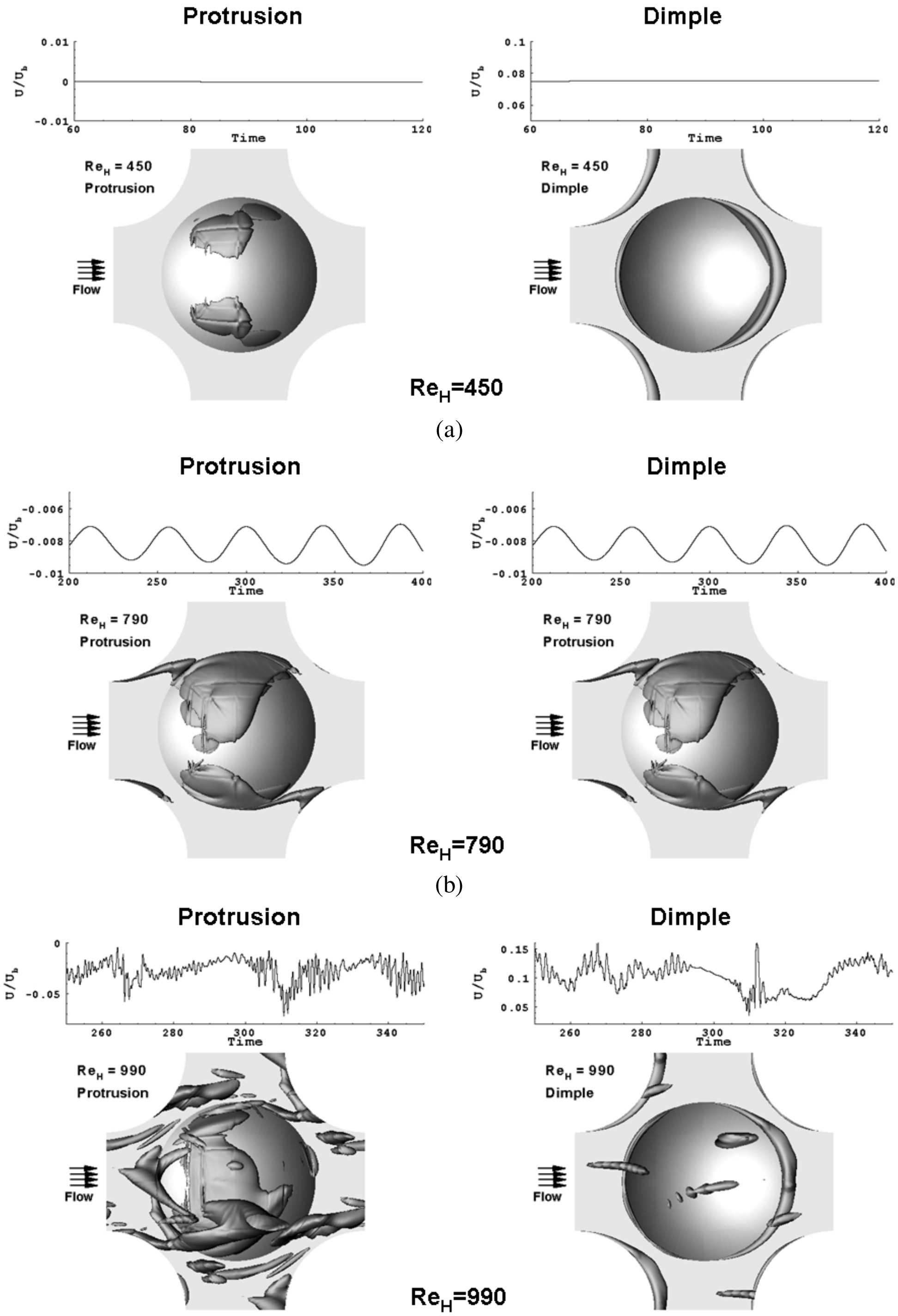

(a)

(b)

(c)

Figure 2.3: Isosurfaces of the coherent vorticity for Case 1 with isosurface level = 10

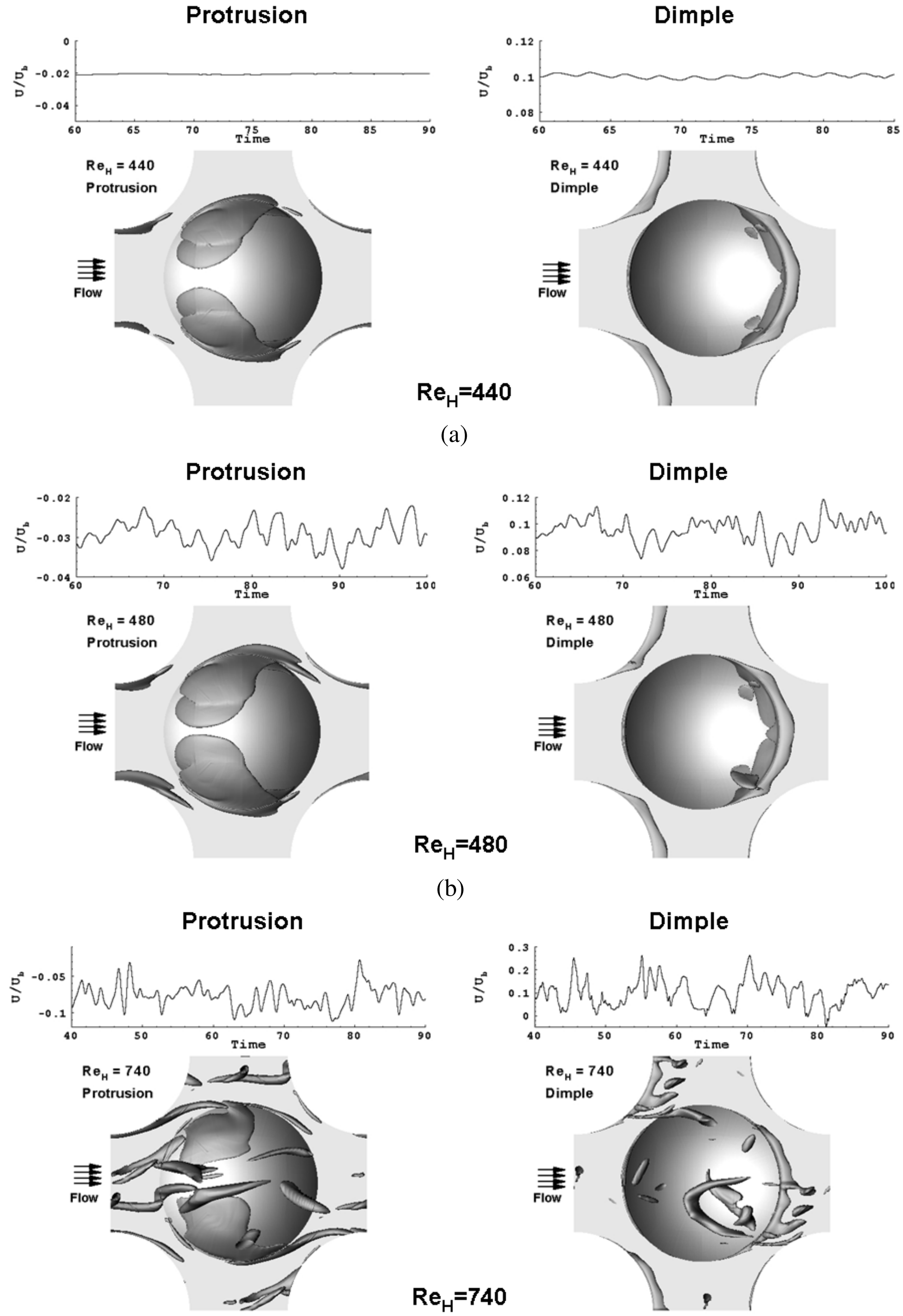

(a)

(b)

(c)

Figure 2.4: Isosurfaces of the coherent vorticity for Case 2 with isosurface level = 10

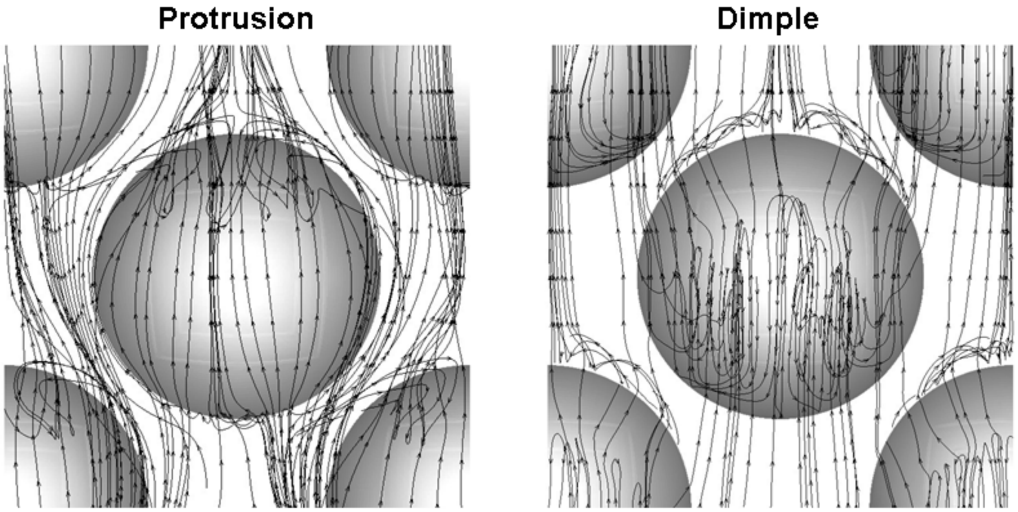

Case 1

(a)

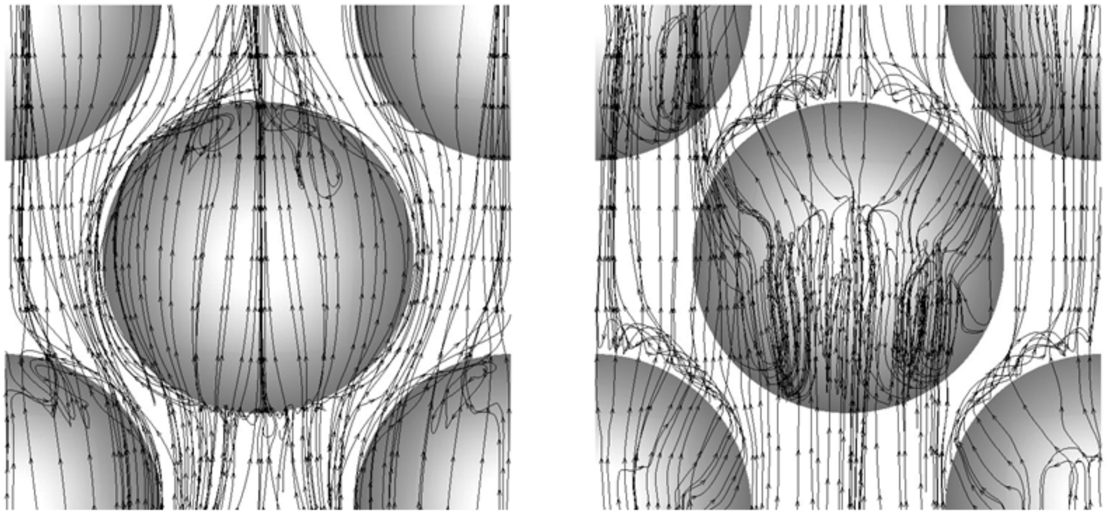

Case 2

(b)

Figure 2.5: Mean flow structures in turbulent flow, at nominal $Re_H = 15000$, for protrusion (left) and dimple (right) for: a) Case 1; b) Case 2

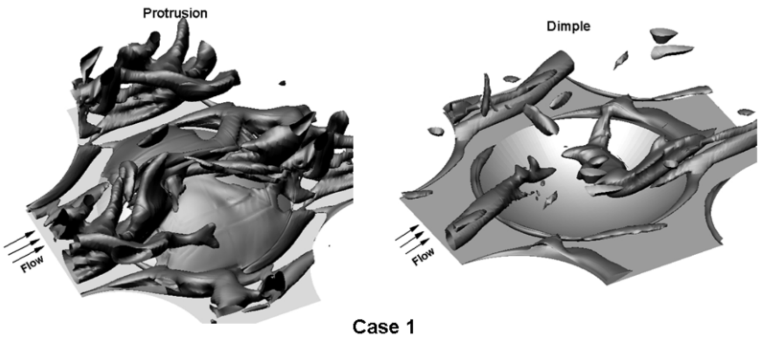

Case 1

(a)

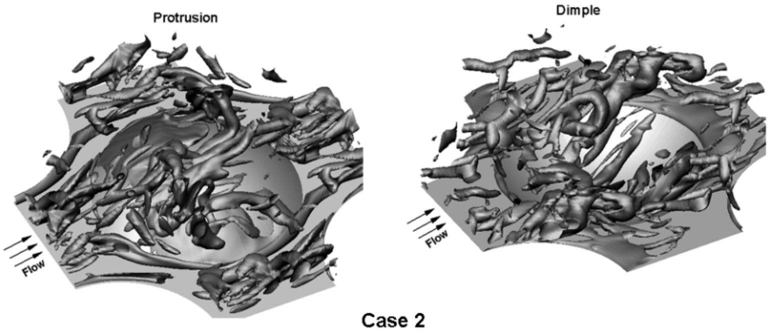

Case 2

(b)

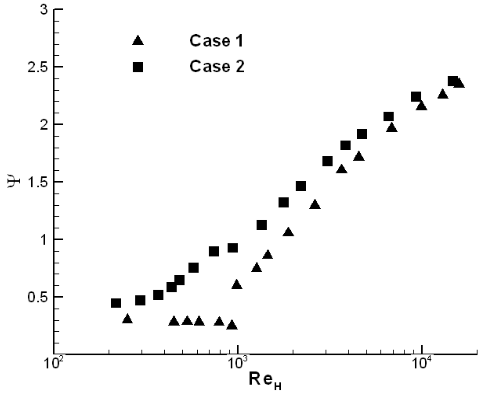

(c)

Figure 2.6: (a) Isosurfaces of coherent vorticity (level =10) at nominal Re_H = 1400 for a) Case 1; (b) Case 2; and c) volume-weighted time averaged coherent vorticity (Ψ).

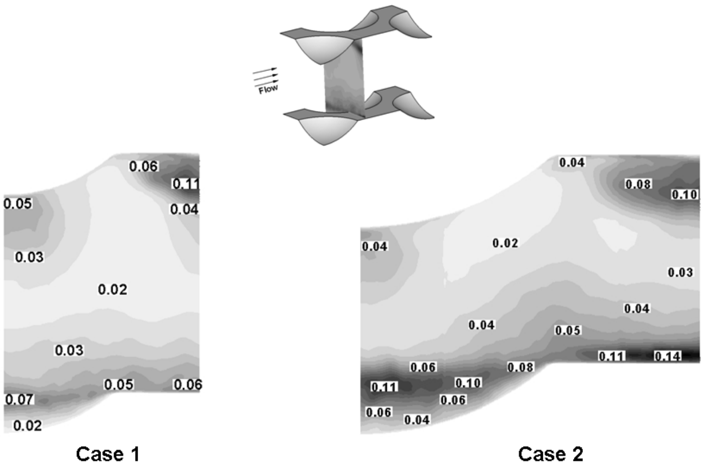

(a)

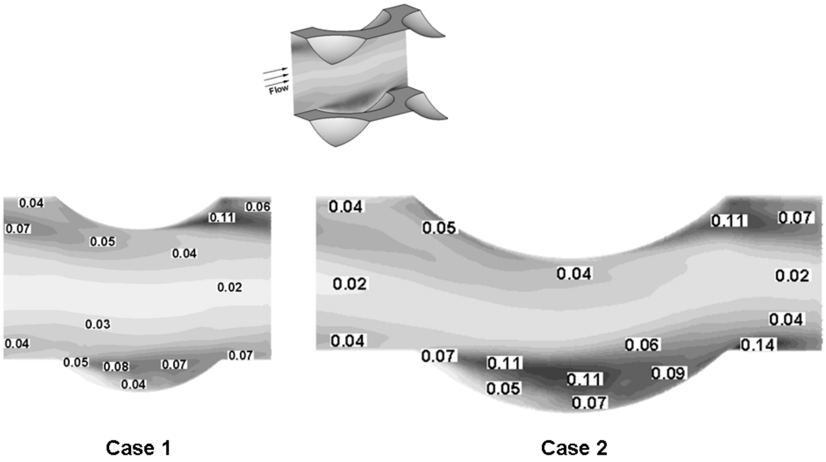

(b)

Figure 2.7: Normalized TKE distribution, at nominal $Re_H = 15000$, on : a) cross sectional cut at 0.2D downstream the dimple edge; b) Stream-wise cut across the centerline of the domain

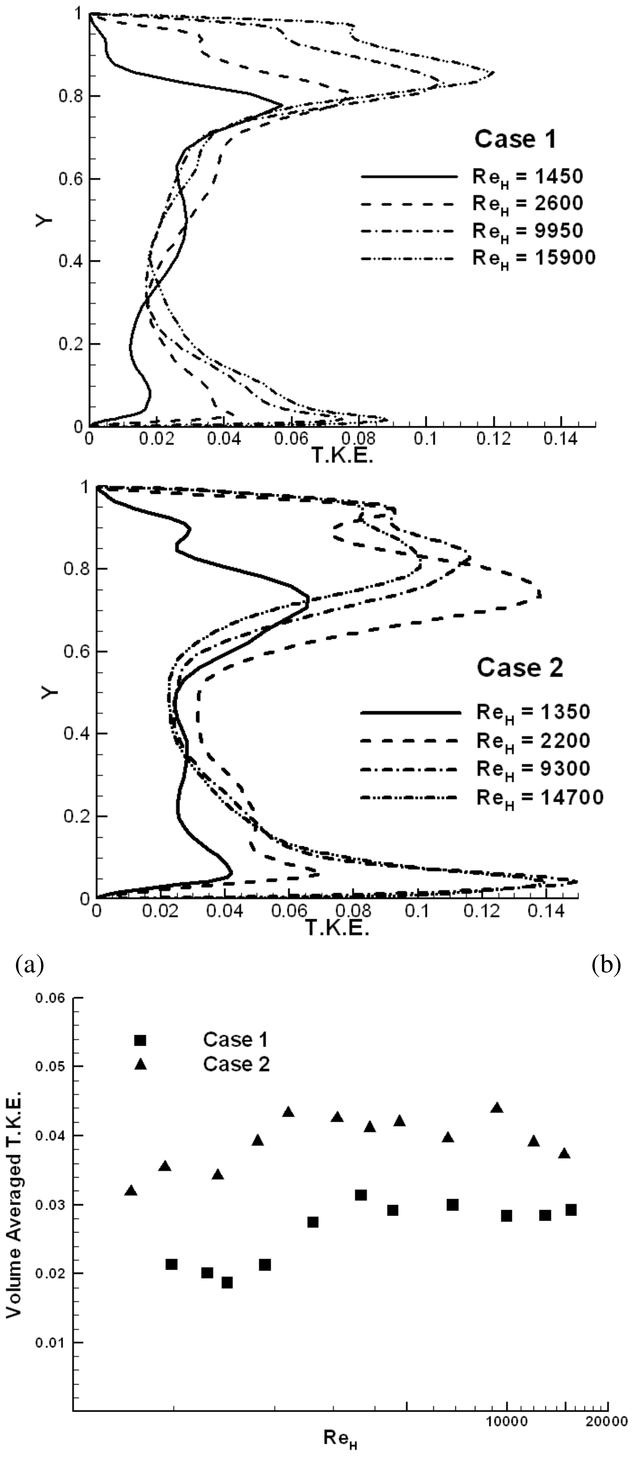

(a) (b)

(c)

Figure 2.8: Profile of TKE at 0.2D downstream of the dimple on the centerline for: a) Case 1; b) Case 2; and c) volume averaged TKE variation with Re_H for both cases.

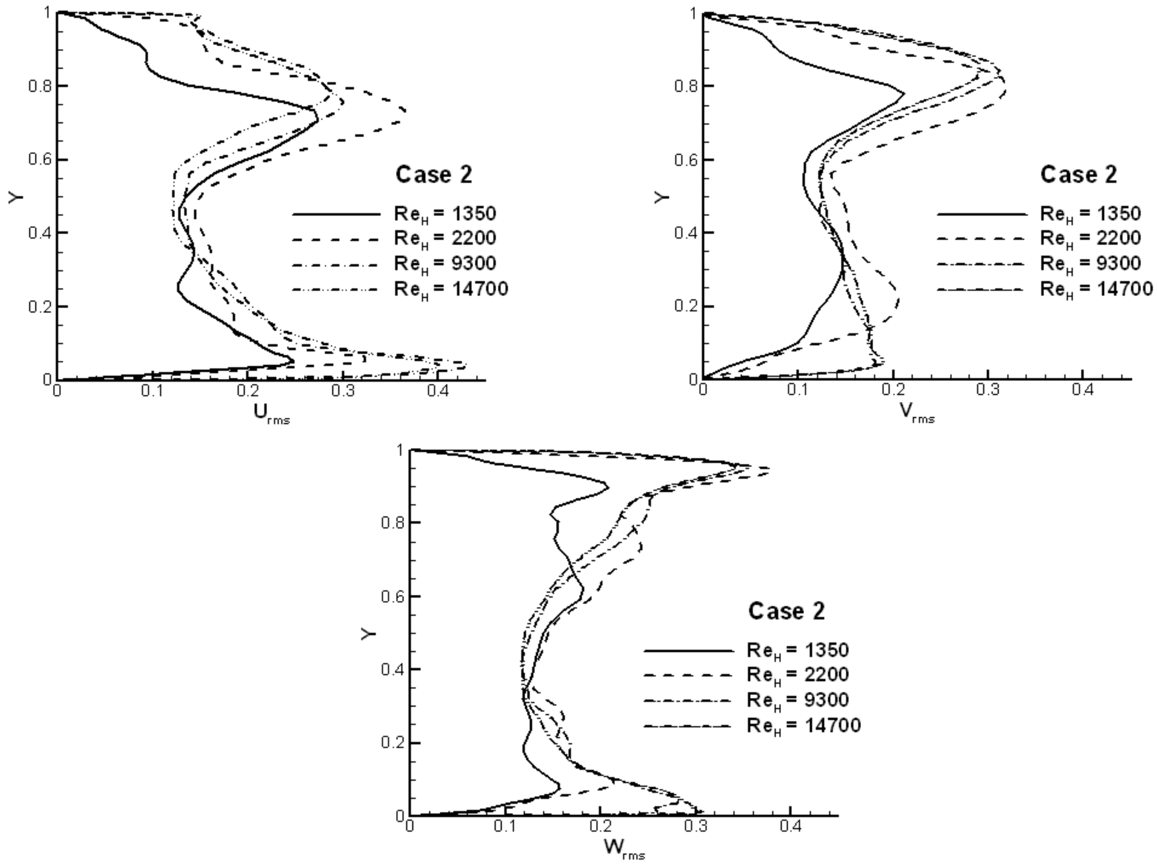

Figure 2.9: RMS Profiles 0.2D downstream of the dimple on the centerline for Case 2

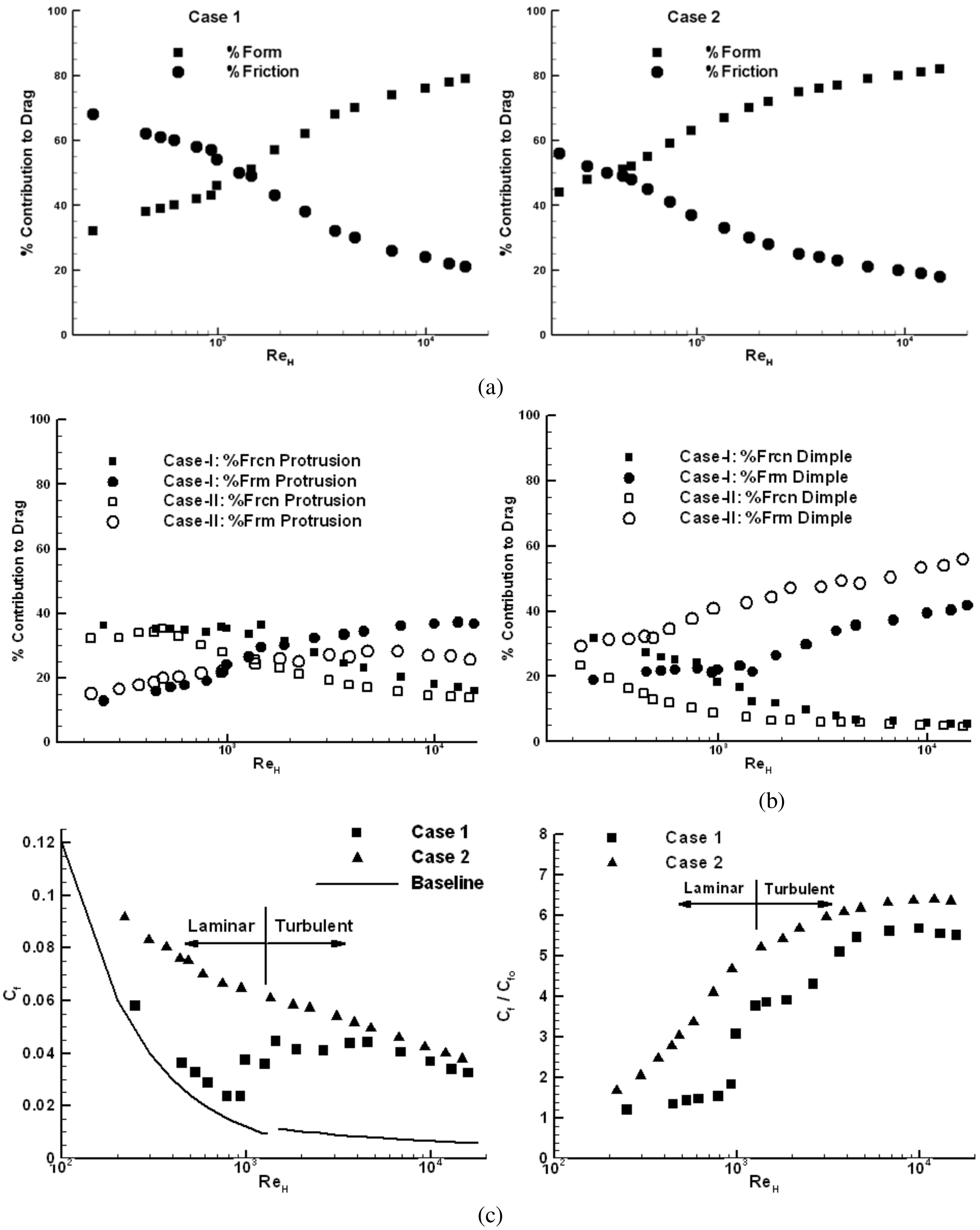

(a)

(b)

(c)

Figure 2.10: Variation of form and friction drag contribution to overall pressure losses. (a) Percentage form and friction contribution to overall losses; (b) Breakdown of contributions from dimple and protrusion surface; (c) Variation of friction coefficient and augmentation ratio with Reynolds number.

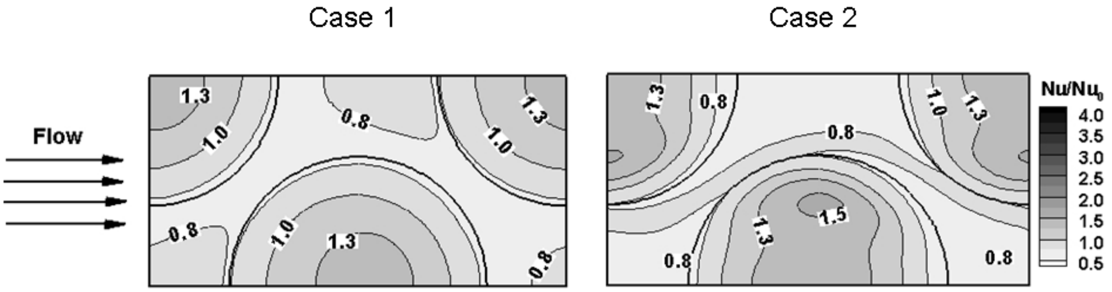

Re$_H$≈250, Protrusion

(a)

Re$_H$≈250, Dimple

(b)

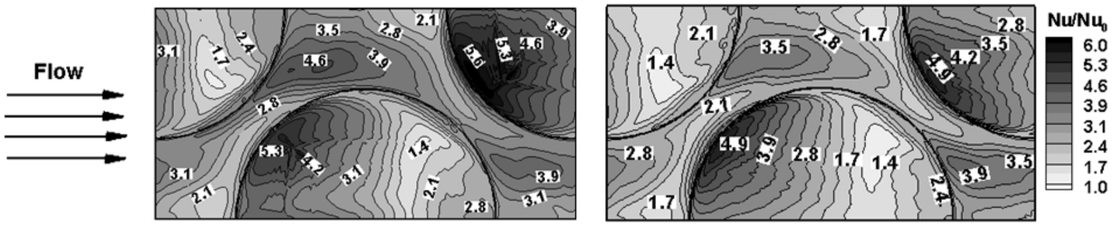

Re$_H$≈15000, Protrusion

(c)

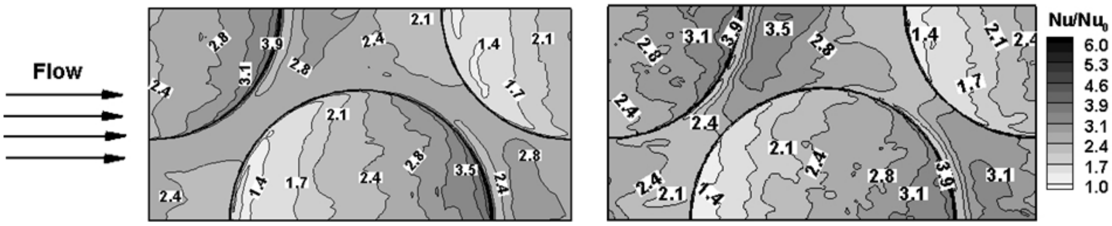

Re$_H$≈15000, Dimple

(d)

Figure 2.11: Distribution of Nusselt number augmentation.

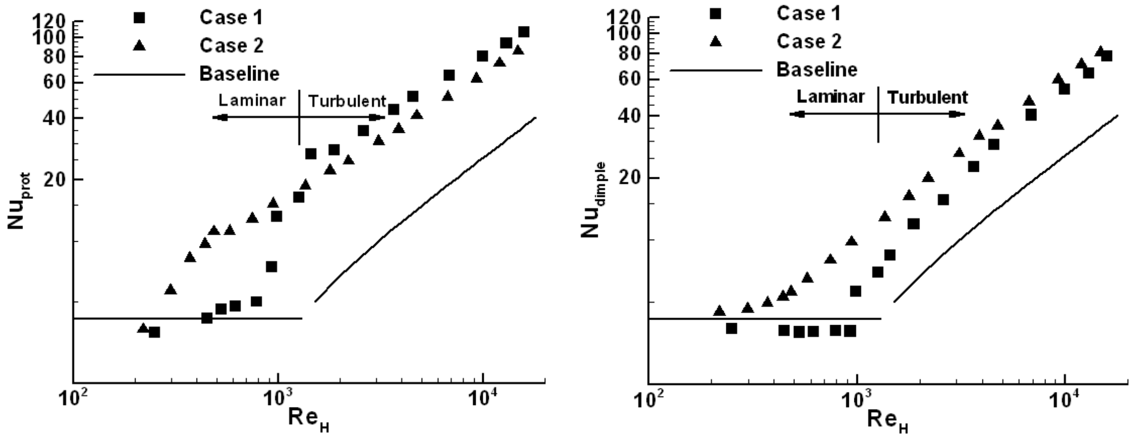

(a) Nusselt on Protrusion side (b) Nusselt on Dimple side

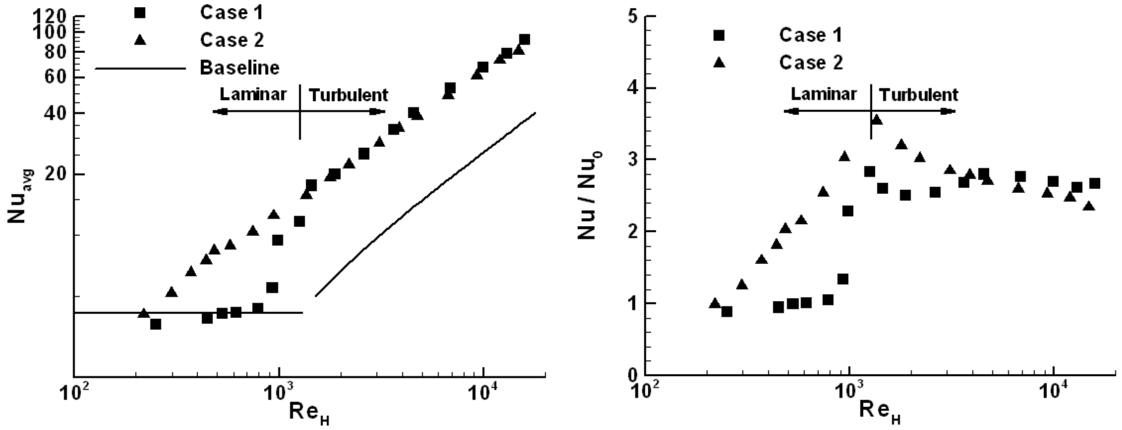

(c) Total Nusselt (d) Total augmentation ratio

Figure 2.12 : Variation of Nusselt number with Re_H for Case 1 and Case 2

Chapter 3: Flow and Heat Transfer Characteristics of Dimpled Multilouvered Fins[1]

3.1 Abstract:

A new fin geometry approximating a dimpled louver in a multilouver configuration under a fully-developed flow assumption is investigated. The calculations are conducted on three fin configurations. Case 1 and 2 investigate the effect of imprint diameter, whereas Case 3 investigates the effect of introducing a perforation in the dimple imprint. It is established that the dimple imprint diameter has a minimal effect on the flow and heat transfer. However, the introduction of the perforation in the dimple changes the flow and heat transfer profoundly on the dimple side of the fin by eliminating any recirculation regions in the dimple and generating higher intensity vortical structures. The introduction of the perforation increases the heat transfer coefficient between 12-50% with a corresponding increase of 15-60% in the friction coefficient.

Keywords: Dimples, Fins, Heat Transfer Enhancement, Large Eddy Simulation.

Nomenclature:

D	Dimple imprint diameter
D_h	Hydraulic diameter
C_f	Fanning friction coefficient
F_p	Fin pitch
k	thermal conductivity
S	Stream-wise pitch
P	Span-wise pitch
H	Fin pitch
L_x	Periodic length
L_P	Louver pitch

---

[1] This chapter is reprinted from Journal of Enhanced Heat Transfer, Vol. 16, Elyyan, M.A. and Tafti, D.K., "Flow and Heat Transfer Characteristics of Dimpled Multilouvered Fins," pp. 43-60, 2009, with permission from Begell House, Inc.

Nu	Nusselt number
Pr	Prandtl number
q''	Constant heat flux on channel walls
Re	Reynolds number
u_τ	friction velocity
y_1^+	distance of first point from fin surface in wall coordinates
δ	Dimple depth

Subscripts

o	Smooth channel
H	Fin pitch

Superscripts

$^+$	Wall units
*	Dimensional quantities

3.2 Introduction:

Heat transfer enhancement is an important factor in increasing the overall efficiency of heat exchangers. Airside thermal resistance typically accounts for more than 80% of the total resistance to heat transfer and hence is of considerable importance. Heat transfer resistance can be decreased by increasing the surface area and/or increasing the heat transfer coefficient. One widely adopted technique is the use of extended surfaces or fins, which are used either as interrupted or continuous surfaces.

Interrupted surfaces work well at low Reynolds numbers typically encountered in compact heat exchangers. Different fin shapes have been tested for maximum heat transfer augmentation; e.g. offset strip fins, and louvered fins. Louvered fin is one of the most popular fin shapes used for heat transfer augmentation in the automobile and HVAC industries due to its effectiveness and economical manufacturability. Extensive research on louvered fins has been carried out both in industry and universities.

Webb and Trauger [1991] experimentally studied heat transfer and flow structure in louvered heat exchangers for Reynolds number (Re_{Lp}= 400-4000). The flow efficiency, which is a measure of flow between louvers, was defined by Webb and

Trauger [1991] as the ratio of the distance the flow travels in the transverse direction to the ideal transverse distance it can travel. The flow efficiency was found to increase with increasing louver angle, and reduced louver to fin pitch ratio. A critical Reynolds number, after which the flow efficiency is independent of the louver angle, was identified.

Tafti *et al.* [1999] used unsteady calculations to cover the laminar to transitional range for two cases; a fully developed periodic flow around a louver, and a developing flow in louvered fins. Duct-directed flow was observed at low Reynolds number; as Reynolds number increased the flow became louver-directed. The local heat transfer from the fin surface was found to be strongly affected by the large scale vortices shed from the louver.

Tafti and Zhang [2001] numerically studied the effect of fin pitch, louver angle, fin thickness and flow depth on the onset, propagation, and characteristic frequencies of instabilities in multilouvered fins. Instabilities were found to occur earlier at larger angles and thicker fins. The internal instabilities in the louver bank were shown to be completely independent of the wake instability in the wake of louvered fin.

Zhang and Tafti [2001] studied the effect of thermal wakes on multilouvered fins numerically. They showed that neglecting the thermal wake effects at low Reynolds numbers resulted in errors as high as 100% in calculating the heat transfer coefficients. The errors were considerably less for louver directed flow at higher Reynolds numbers.

Lyman *et al.* [2002] experimentally studied the effect of louver angle and the ratio of fin pitch to louver pitch on the heat exchanger performance. The adiabatic wall temperature was used for heat transfer coefficients in order to distinguish the thermal and flow field effects on louver performance. Larger fin pitches and louver angles were reported to provide better performance at low Reynolds number flows.

DeJong and Jacobi [2003] studied the flow efficiency, pressure drop and heat transfer behavior in louvered fin arrays. Low heat transfer coefficients were reported at the turnaround louver due to its larger length and slower flow velocity than other louvers. DeJong and Jacobi [2003] also reported that, unlike offset-strip fins, vortex shedding from louvers did not have a significant effect on heat transfer.

In contrast to the interrupted surfaces of louvered fins, continuous fins, e.g. wavy fins and dimpled surfaces, have proven to provide good heat transfer augmentation at lower pressure drop penalty than interrupted surfaces. The use of dimpled surfaces for heat transfer augmentation has received much attention lately due to their good heat transfer characteristics. Afansayev *et al.* [1993] studied the application of shallow dimples ($\delta/D = 0.067$) on flat plates on pressure drop and heat transfer for turbulent flow. They reported a 30-40% increase in heat transfer with negligible increase in pressure drop.

Experimental studies of the flow structure in dimpled surfaces showed the existence of flow recirculation zone in the upstream half of the dimple, with primary vortex shedding from the center of the downstream portion of the dimple and shedding of secondary vortex pair from the span-wise edges of the dimple (Mahmood *et al.* [2000], Ligrani *et al.* [2001] and Ligrani *et al.* [2005]). A region of low heat transfer was observed in the upstream half of the dimple cavity followed by a high heat transfer region in the flow reattachment region in the downstream half of the dimple and the flat landing downstream of dimple (Mahmood *et al.* [2000], Ligrani *et al.* [2005], Chyu *et al.* [1997], Moon *et al.* [2000], Burgess and Ligrani [2004], and Ekkad and Nasir [2003]).

Most of the numerical studies reported on the dimpled channel geometry were conducted in the fully turbulent flow regime and used steady-state RANS modeling Wang *et al.* [2003], Lin *et al.* [1999], Isaev and Leont'ev [2003], Park *et al.* [2004], Won and Ligrani [2004] and Park and Ligrani [2005]). Patrick and Tafti [2004] predicted heat transfer and pressure drop augmentation in a channel with one side dimpled in the low to medium Reynolds number flow ($Re_H = 50 - 2000$) using DNS and LES. Elyyan *et al.* [2006] predicted the flow structure and heat transfer distribution in a channel with dimples and protrusion on opposite walls at fully developed turbulent flow ($Re_H = 15000$) using LES.

In an effort to disrupt the boundary layer in continuous fins, perforated fins have also been studied where a pattern of spaced holes are formed in the fin material before the fin is folded into a U-shaped flow channel (Webb and Kim [2005]). The perforated fins produce little heat enhancement in the laminar flow regime and a moderate one in the turbulent regime (Webb and Kim [2005]). Fujii *et al.* [1988] studied a new type of perforated fin, where the heat exchanger is constructed with surfaces using enlargements and contractions forming a trapezoidal shape. Fujii et al [1988] covered Reynolds number flows less than 3000. They reported that the heat enhancement from the fin surface is due to the secondary flow induced by the suction and injection through the perforations, and due to the frequent boundary layer interruptions at each contraction part.

3.3 Objective:

The objective of this paper is to investigate a new fin geometry based on a dimpled louver fin in an attempt to combine the advantages of the interrupted surfaces of a louvered fin, the surface roughness of dimples, and the smaller scale discontinuities introduced by perforations. In the new fin geometry spherical indentations in the form of dimples are placed on the flat louvered fin surface, as shown in Figure 3.1.

Three louver geometries are studied in this paper. The effect of dimple diameter is studied in cases 1 and 2. Whereas Case 3 investigates the effect of a perforation in the dimple on the overall flow structure and heat transfer from the louver. The paper presents details of the instantaneous and mean flow structure, and detailed heat transfer distribution on the fin surface.

3.4 Fin Geometry

Flow through a louvered fin array can be classified as duct-directed or louver-directed flow (Figure 3.1-a). The duct-directed flow occurs at low Reynolds numbers (DeJong and Jacobi [2003]) between two adjacent fins. On the other hand, louvered directed flow occurs at higher Reynolds numbers, large louver pitch (L_p) and small fin pitch (F_p) (Zhang and Tafti [2001]). For example, Zhang and Tafti [2001] reported a flow efficiency (flow angle/louver angle) of 0.94 for fins with fin pitch to louver pitch ratio (F_P/L_P) of 1.0 and louver angle of 30^o at Reynolds number (Re_{Lp}= 1000); a flow efficiency of 0.88 was reported for louver angle of 25^o at the same Reynolds number.

In the present work, to simplify the geometry and ensuing mesh generation, we assumed that the flow is louver directed and that the louvered geometry can be approximated by a flat plate fin oriented parallel to the flow, Figure 3.1-b, with the fin spacing in the streamwise and pitchwise directions derived from a typical louvered geometry rotated by an angle equal to the louver angle.

This modification combined with a fully-developed flow and heat transfer assumption, allows us to consider a single dimpled plate fin for computational purposes, but which is representative of an infinite array of plate fins which approximates an infinite array of louvers with louver directed flow. The ensuing fin geometry is shown in Figure 3.1-b with details of the plate fin in Figure 3.2.

Table 3.1 and Table 3.2 present the dimensions for the three cases non-dimensionalized with the fin pitch (H^*). In all cases the fin length to fin pitch ratio is ($L^*/H^* = 1.0$), fin thickness ratio ($b^*/H^* = 0.1$), dimple depth ratio ($\delta^*/H^* = 0.1$). Cases 1 and 2 use a plain dimple, whereas Case 3 uses a dimple with a perforation with size ratio ($d^*/H^*=0.2$). Case 1 and Case 3 have dimple diameter ratios ($D^*/H^*=0.4$), while the ratio for Case 2 is 0.3. Hence, Case 1 and Case 2 investigate the effect of dimple diameter, whereas Case 1 and Case 3 investigate the effect of the perforation in the dimple cavity.

3.5 Computational Model, Governing Equations, and Numerical Method

The incompressible time-dependent Navier-Stokes and energy equations are solved in a generalized coordinate system. Fully-developed hydrodynamic and thermal conditions are assumed. Constant heat flux boundary condition (q''^*) and no-slip boundary conditions are applied at the fin surface. The equations are non-dimensionalized by the fin pitch (H^*) as the characteristic length scale, friction velocity (u_τ^*) as the characteristic velocity scale, and $q''^* H^*/k^*$ as the characteristic temperature scale. To facilitate the application of periodicity in the streamwise direction, both pressure and temperature are decomposed into mean and fluctuating components to modify the momentum and energy equations, for further information see Zhang *et al.* [1997]. Subgrid turbulence is modeled with the Smagorinsky model in which the turbulent viscosity is calculated dynamically, for more information about the dynamic Smagorinsky model see Germano *et al.* [1991]. A constant Prandtl number Pr=0.7 is assumed for air, while the turbulent Prandtl number is assumed to be 0.5, see Moin *et al.* [1991]. The model is activated only when the flow showed a chaotic turbulence like behavior, which for Case 1 was at $Re_H = 1080$, at $Re_H = 930$ for Case 2 and at $Re_H = 850$ for Case 3.

The modified non-dimensional time dependent Navier-Stokes and energy equations are discretized with a conservative finite-volume formulation using a second-order central difference scheme on a non-staggered grid topology. The Cartesian velocities, pressure, and temperature are calculated and stored at the cell center, whereas the contravariant fluxes are stored and calculated at the cell faces. A projection method is used for time integration. The temporal advancement is performed in two steps, a predictor step, which calculates an intermediate velocity field, and a corrector step, which calculates the updated velocity at the new time step by satisfying discrete continuity. The computer program GenIDLEST (Generalized Incompressible Direct and Large-Eddy Simulations of Turbulence) used for these simulations has been applied extensively to study flow and heat transfer in stationary and rotating internal ducts used for cooling gas turbine blades, e.g. Sewall *et al.* [2006] and other heat transfer augmentation geometries, e.g. Cui and Tafti [2002]. Details about the algorithm, functionality, and capabilities can be found in Tafti [2001].

3.6 Baseline Nu and C_f

The baseline laminar Fanning friction coefficient and Nusselt number for flow between parallel smooth plates and the Petukhov and Gnielinski correlations for a smooth channel, Incropera and Dewitt [1996], are used to normalize the Fanning friction coefficient and Nusselt number of the domain. These correlations were chosen due to their validity and accuracy over the range of Reynolds numbers of interest in this study. Friction coefficient and Nusselt number for these correlations based on the Re_H are as follows

$$\begin{aligned} C_{f_0} &= \frac{12}{Re_H} && ;Re_H < 1500 \\ C_{f_0} &= (1.58 \ln Re_H - 2.185)^{-2} && ;1500 \le Re_H \le 2.5\times10^6 \end{aligned} \qquad (1)$$

$$\begin{aligned} Nu_0 &= 4.12 && ;Re_H < 1500 \\ Nu_0 &= \frac{(C_{f_0}/2)(Re_H - 500)Pr}{1 + 12.7(C_{f_0}/2)^{1/2}(Pr^{2/3} - 1)} && ;1500 \le Re_H \le 2.5\times10^6 \end{aligned} \qquad (2)$$

where for smooth parallel plates, the hydraulic diameter (D_h) is twice the channel height (H), i.e. $Re_{Dh}=2Re_H$.

3.7 Grid Resolution:

A hybrid structured/unstructured multi-block grid is used for meshing the computational domain. Case 1 and Case 2 were meshed using 100 grid blocks with a total of 1.77 million cells; while Case 3 mesh consisted of 108 blocks with 1.88 million cells.

The mesh was designed to have a finer grid spacing in the vicinity of the fin surface, where the first grid point was placed at $\Delta \approx 4.0 \times 10^{-3}$ from the fin surface. The overall grid structure and spacing was extrapolated from previous investigations in similar geometries, see Elyyan *et al.* [2006].

Due to the high computational cost of conducting a grid independency study in unsteady calculations such as these, an *a-posteriori* test, at the highest Reynolds number for Case 3, was conducted to check the sufficiency of the grid distribution near the fin surface. Figure 3.3 shows the distribution of y_1^+ on the top and bottom fin surface for Case 3 at Re_H=1770, the highest Reynolds number investigated in this study. The condition of $y_1^+<1.0$ based on local shear stress was satisfied throughout most of the fin surface with a maximum value of $y_1^+=1.5$ obtained at the leading edge. Based on the gird spacing normal to the wall, 5- 6 grid points existed between the surface and $y^+<10$. The surface averaged values of the wall parallel distribution gives a maximum value of $\Delta^+_{//} = 8$ at the highest Reynolds number simulated. Thus, the grid resolution used was deemed sufficient for the LES calculations conducted in the current work.

3.8 Results and Discussion:

3.8.1 Instantaneous Flow structure

The presence of large scale flow structures or vorticity in the presence of a heat transfer surface is a good comparative indicator of the heat transfer augmentation. This section describes the instantaneous flow structures in the domain for the three cases at low and medium Reynolds number flows. The instantaneous flow structures are described with the aid of coherent vorticity. The coherent vorticity is identified using the vortex eduction technique proposed by Chong and Perry [1990].

As a result of the vortex shedding from the leading edge of the fin, the flow exhibits unsteady behavior at Reynolds number as low as Re_H=200. Figure 3.4 and Figure 3.5 show the iso-surfaces of the coherent vorticity on the top and bottom sides of the fin at a single-valued iso-surface level of 10 at $Re_H = 200$. The iso-surfaces for Case 1 and 2 show vortex shedding and shear layer instabilities from the fin leading edge on both sides of the fin. While shear layer formation and regeneration at the upstream and downstream dimple rims is obvious for Case 1, no such behavior is noticed for Case 2; this is a result of the smaller dimple imprint diameter of Case 2.

The bottom side of the fin shows the existence of coherent structures at the top of the protrusion for Case 1 and 2 as a result of flow impingement and acceleration. Case 3 shows a much different distribution which is characterized by: i) richer coherent structures present on the fin leading edge of the fin and around the dimple rim, ii) vortex shedding from the protrusion at the bottom side of the fin, which is due to the flow redirection from the top to bottom of the fin through the perforation, iii) shear layer formation and regeneration at the sides of the perforation as the flow passes from the top to bottom side of the fin.

Figure 3.6 and Figure 3.7 show the coherent structure iso-surfaces at $Re_H \sim 500$ with a single valued iso-surface of 18. Roller vortex shedding from the leading edge of the fin is more pronounced for this Reynolds number for Case 1 and 2. There is no vortex shedding from the first row of dimples, which lies within the recirculation zone of the leading edge separated shear layer. Weak vortex shedding from the downstream dimples is noticed for Case 1 and 2. The bottom side of the fin of Case 1 and 2 shows similar behavior to that at $Re_H = 200$, but with coherent structures at the leading edge of the fin and top of the protrusion. The coherent structures in Case 3 once again show a behavior distinct from the other cases. The roller vortices shed from the leading edge are not present and two vortex tube like structures are shed from the upstream dimple. The bottom of the fin shows structures that are similar to that at low Reynolds number.

Overall, the addition of the perforation at the center of the dimple alters the flow structure significantly. The alteration is a result of the difference in pressure inside the dimple cavity and the protrusion side, which induces flow from the top to the bottom of the fin. The induced flow results in boundary layer regeneration not only at the rim of the dimple but also at the edges of the perforation.

3.8.2 Mean Flow

In this section we consider the mean flow structure in the domain with the aid of mean velocity streamlines at a stream-wise plane across the centerline of the domain (Z=0). Figure 3.8 and Figure 3.9 show the mean velocity streamlines at stream-wise plane at Z=0 at $Re_H = 200$ and $Re_H \sim 900$, respectively, for the three cases.

The mean flow structure at $Re_H = 200$ is shown in Figure 3.8. Case 1 and 2 show similar flow structure, where a separated shear layer forms at the leading edge of the fin and reattaches within the dimple. The flow on the bottom side of the fin impinges at the front of the protrusion and accelerates till the center of the protrusion, after which flow decelerates but remains attached to the protrusion surface, i.e. no flow separation region is observed at the back of the protrusion. No flow recirculation is observed for Case 3; rather the flow is redirected between the top and bottom sides of the fin through the perforation placed at the center of the dimple.

Figure 3.9 shows the mean flow structure at a higher Reynolds number ($Re_H \sim 900$) for the three cases. The mean flow for Case 1 and 2 is similar to that observed at the lower Reynolds number. The most significant change in flow structure at this Reynolds number is the flow separation in the wake of the protrusion, and the vortex shedding in the wake of the fin. Case 3 shows the existence of flow separation and recirculation in the dimple cavity which leads to partial closing of the opening between the two sides of the fin.

3.8.3 Fin Surface Heat Transfer Distribution

Figure 3.10 and Figure 3.11 show the Nusselt number augmentation distribution on the top and bottom fin surface, respectively, at $Re_H \sim 900$ for Case 1 and 3. The heat transfer distribution for Case 2 is very similar to Case 1 and is not shown. Both Case 1 and 3 show high heat transfer augmentation at the leading edge of the fin due to boundary layer regeneration. In Case 1, a low heat transfer region is observed in the flow recirculation zone in the upstream half of the dimple followed by an increase in the reattachment zone and downstream of the dimple on the flat landing. The bottom side of the fin exhibits high heat transfer augmentation in the region of flow impingement at the front of the protrusion and low heat transfer in the wake due to flow separation at the back of the protrusion.

Case 3, on the other hand, shows a different heat transfer distribution. Much higher heat transfer augmentation is observed in the dimple cavity and downstream of the dimple. This is a result of flow being drawn into the dimple, eliminating most of the recirculation observed in Case 1, followed by much stronger flow ejection from the dimple cavity which promotes higher velocities and larger vorticity magnitude in the vicinity of the surface. On the protrusion side, because of the flow redirection from the top of the fin, mixing in the wake of the protrusion is enhanced significantly, which increases heat augmentation in the wake of the protrusion.

3.8.4 Friction Coefficient and Nusselt Number Augmentations

Figure 3.12 shows the variation of the friction coefficient and its augmentation with Reynolds number for the three fin cases and a flat plate fin with no dimples. The friction coefficient profiles indicates that the size of the imprint diameter did not significantly affect the friction characteristics of the flow, which agrees with the observations made from the flow field structure explained earlier. Case 3, on the other hand, shows a friction coefficient that is on average 50% higher than that of Case 1 and 2. The increase in friction coefficient is a result of increased surface shear induced by the flow redirection in the dimple and a probable increase in form losses. Note that the friction coefficient for the flat plate fin is lower than that of the different dimpled fin cases; the largest difference was for Case 3 with about 80% increase of C_f from that of the flat plate fin. The friction coefficient augmentation, Figure 3.12-b, peaks for Case 3 at $Re_H = 1350$ with a value of 6.12.

Figure 3.13 shows the Nusselt number variation and its augmentation over a plain channel for the three dimpled fin cases and the flat plate fin. Similar to the friction coefficient, the size of the dimple imprint diameter did not have a large effect on the Nusselt number, although Case 1 has slightly higher values. The Nusselt number in Case 3 exhibits values which are between 20-50% higher than those of Case 1 and 2. Case 1 and Case 2 resulted in lower Nusselt than the flat plate fin, Case 3 on the other hand showed about 10% increase over the flat plat fin. Case 3 shows a peak Nusselt number augmentation of 5.6 at Re_H =1100 based on a turbulent baseline value.

Case 1 and 2 show very similar friction and Nusselt number values indicating that the dimple imprint diameter does not have a large effect on the overall flow structure and heat transfer characteristics of the fin. Modifying the fin geometry by adding the dimple on the fin surface results in larger heat transfer area, where the increase is about 11% for the three fin cases from that of the flat plate fin. Note that adding the perforation to the fin surface reduces the area by 15%; although this reduction is balanced by the additional area of the side walls of the perforation.

To further quantify the effect of modifying the fin geometry on the heat transfer characteristics of the fin, the variation of the top (dimple) and bottom (protrusion) Nusselt number with Reynolds number is shown in Figure 3.14. The heat transfer from the protrusion surface is quite insensitive to the change in geometry as seen in Figure 3.14-a. Flow impingement and acceleration at the front of the protrusion is what drives heat out of the fin surface. Although some of the heat transfer through impingement and acceleration at the top of the protrusion is lost in Case 3, it is compensated by the fact that less flow separation and recirculation is associated with this case.

The Nusselt number profile on the dimple side of the fin shows that all the improvement in overall heat transfer in Case 3 comes from the dimple side of the fin. The better performance of Case 3 is due the effective role of the perforation in reducing flow recirculation inside the dimple cavity, increasing flow redirection between the fin sides and enhancing vortex ejection from the dimple. Note that the Nusselt number values for Case 1 and 2 deviate at high Reynolds number flows, Re_H>900, where the Nusselt number of Case 1 levels off at a value of about 12 and Case 2 keeps increasing at a lower rate.

3.9 Summary and Conclusions

A new fin geometry which combines the heat transfer enhancement properties of interrupted surfaces with surface roughness has been investigated using Direct and Large

Eddy Simulations. The fin geometry approximates a dimpled louver in a multilouver configuration under a fully-developed assumption.

The calculations are conducted on three fin configurations. Case 1 and 2 have identical fin shapes except a larger dimple imprint diameter in Case 1, whereas Case 3 introduces an opening or perforation in the dimple. It is established that the dimple imprint diameter has a minimal effect on the flow and heat transfer. On the other hand, the introduction of the perforation in the dimple changes the flow and heat transfer profoundly, mainly on the dimple side of the fin. By redirecting flow from the dimple to the protrusion side of the fin, the recirculation region in the dimple is eliminated or reduced. In addition, more flow is drawn into the dimple cavity, resulting in enhanced vorticity production and ejection onto the flat landing downstream of the dimple. Further, the edges of the perforation also act as boundary layer regenerators and are regions of high heat transfer. The redirected flow ejecting out on the protrusion side enhances mixing, and enhances heat transfer in the wake of the protrusion. While the favorable effect of the perforation on the protrusion wake is offset by a reduction in impinging flow area on the protrusion face, the presence of the perforation has a large favorable effect on heat transfer on the dimple side.

The introduction of the perforation increases the heat transfer coefficient between 12-50% but also increases friction up to 60%.

3.10 Acknowledgements

This work is a result of support provided by the US Army RDECOM, Fort Belvoir, VA and Modine Manufacturing Co., Passenger Thermal Management, Racine WI for air-side heat transfer enhancement in next generation compact heat exchangers. The support is gratefully acknowledged. The calculations were performed on Virginia Tech’s Terascale computing facility, System-X. The allocation grant and support provided by the staff is also gratefully acknowledged.

3.11 Reference

Afanasyev, V.N., Chudnovsky, Ya.P., Leontiev, A.I., and Roganov, P.S. (1993) Turbulent Flow Friction and Heat Transfer Characteristics for Spherical Cavities on a Flat Plate, Experimental Thermal and Fluid Science, No. 7, pp 1-8.

Burgess, N. K., and Ligrani, P. M. (2004) Effects of Dimple Depth on Nusselt Numbers and Friction Factors for Internal Cooling Channel, Proc. of ASME Turbo Expo 2004, Paper No. GT2004-54232.

Chong, M., Perry, A., and Cantwell, B.J. (1990) A General Classification of Three-Dimensional Flow Fields, Physics of Fluids A, Vol. 2, pp 765-777.

Chyu, M.K., Yu, Y., Ding, H., Downs, J.P., and Soechting, F.O. (1997) Concavity Enhanced Heat Transfer in an Internal Cooling Passage, Proc. ASME Turbo Expo 1997, Paper No. 97-GT-437.

Cui, J., and Tafti, D. K. (2002) Computations of Flow and Heat Transfer in a Three-Dimensional Multilouvered Fin Geometry, Int'l Journal Heat Mass Transfer, Vol. 45, pp. 5007-5023.

DeJong, N. C., and Jacobi, A. M. (2003) Localized Flow and Heat Transfer Interactions in Louvered-Fin Arrays, Int'l Journal of Heat and Mass Transfer, Vol. 46, pp. 443-455.

Ekkad, S., and Nasir, H. (2003) Dimple Enhanced Heat Transfer in High Aspect Ratio Channels, Journal of Enhanced Heat Transfer, Vol. 10, No. 4, pp 395-405.

Elyyan, M., Rozati, A., and Tafti, D. (2006) Study of Flow Structures and Heat Transfer in Parallel Fins with Dimples and Protrusions Using Large Eddy Simulation, Proc. ASME Joint US-European Fluids Eng Summer Meeting, Paper No. FEDSM2006-98113.

Fujii, M., Sehimo, Y., and Yamanak, G. (1988) Heat Transfer and Pressure Drop of Perforated Surface Heat Exchanger with Passage Enlargement and Contraction, Int'l Journal of Heat and Mass Transfer, Vol. 31, No. 1, pp. 135-142.

Germano, M., Piomelli, U., Moin, P., and Cabot, W.H. (1991) A Dynamic Subgrid-Scale Eddy Viscosity Model, Phys. Fluids, Vol. 3, pp. 1760-1765.

Incropera, F., and DeWitt 1996. Fundamentals of Heat and Mass Transfer. 4th Edition, John Wiley, New York.

Isaev, S.A., and Leont'ev, A.I. (2003) Numerical Simulation of Vortex Enhancement of Heat Transfer under Conditions of Turbulent Flow Past a Spherical Dimple on The Wall of a Narrow Channel, High Temperature, Vol. 41, No. 5, pp 655-679.

Ligrani, P., Burgess, N. and Won, S. (2005) Nusselt Numbers and Flow Structure on and Above a Shallow Dimpled Surface Within a Channel Including Effects of Inlet Turbulence Intensity Level, Journal of Turbomachinery, Vol. 127, pp 321-330.

Ligrani, P.M., Harrison, J.L., Mahmood, G.I., and Hill, M.L. (2001) Flow Structure Due To Dimple Depressions on a Channel Surface, Physics of fluids, Vol. 13, No. 11, pp 3442-3451.

Lin, Y.L., Shih, T.I-P., and Chyu, M.K. (1999) Computations of Flow and Heat Transfer in a Channel with Rows of Hemispherical Cavities, Proc. ASME Turbo Expo 1999, Paper No. 99-GT-263.

Lyman, A. C., Stephen, R. A., Thole, K. A., Zhang, L. W., and Memory, S. B. (2002) Scaling of Heat Transfer Coefficients Along Louvered Fins, Experimental Thermal and Fluid Sciences, Vol. 26, pp. 547-563.

Mahmood, G.I., Hill, M.L., Nelson, D.L., and Ligrani, P.M. (2000) Local Heat Transfer and Flow Structure on and Above a Dimpled Surface in a Channel, Proc. ASME Turbo Expo 2000, Paper No. 2000-GT-230.

Moin, P. Squires, K., Cabot, W., and Lee, S. (1991) A Dynamic Sub-Grid-Scale Model for Compressible Turbulence and Scalar Transport, Phys. Fluids A, Vol. 3, No. 11, pp. 2746- 2757.

Moon, H.K., O'Connell, T.O., and Glezer, B. (2000) Channel Height Effect on Heat Transfer and Friction in a Dimpled Passage, Journal of Engineering for Gas Turbine and Power, Vol. 122, pp 307-313.

Park, J., and Ligrani, P. M. (2005) Numerical Predictions of Heat Transfer and Fluid Flow Characteristics for Seven Different Dimpled Surfaces in a Channel, Numerical Heat Transfer A, Vol. 47, pp 209-232.

Park, J., Desam, P.R., and Ligrani, P.M. (2004) Numerical Predictions of Flow Structure Above a Dimpled Surface in a Channel, Numerical Heat Transfer A, No. 45, pp 1-20.

Patrick, W.V., and Tafti, D.K. (2004) Computations of Flow Structures and Heat Transfer in a Dimpled Channel at Low to Moderate Reynolds Number, Proc. 2004 ASME Heat Trans/Fluids Eng Summer Conf., Paper No. HT-FED2004-56171.

Sewall, E.A., Tafti, D.K., Graham, A.B., Thole, K.A., 2006. Experimental validation of large eddy simulation of flow and heat transfer in a stationary ribbed duct, Int'l Journal Heat and Fluid Flow, No. 27, pp 243-258.

Tafti, D. K., and Zhang, X. (2001) Geometry effects on flow transition in multilouvered fins – onset, propagation, and characteristic frequencies, Int'l Journal of Heat and Mass Transfer, Vol. 44, pp. 4195-4210.

Tafti, D. K., Zhang, L. W., and Wang, G. (1999) Time Dependent Calculation Procedure for Fully Developed and Developing Flow and Heat Transfer in Louvered Fin Geometries, Numerical Heat Transfer A, Vol. 35, pp. 225-249.

Tafti, D.K. (2001) GenIDLEST – A Scalable Parallel Computational Tool for Simulating Complex Turbulent Flows, Proc. ASME Fluids Engineering Division, FED publication, Vol. 256, pp. 347-356.

Wang, Z., Yeo, K.S., and Khoo, B.C. (2003) Numerical Simulation of Laminar Channel Flow over Dimpled Surface, Proc. AIAA Conference, Paper No. AIAA 2003-3964.

Webb, R. L., and Kim, N. (2005) Principles of Enhanced Heat Transfer, New York: Taylor & Francis, p. 118-122.

Webb, R. L., and Trauger, P. (1991) Flow Structure in the Louvered Fin Heat Exchanger Geometery, Experimental Thermal and Fluid Science, Vol. 4, pp. 205-217.

Won, S., and Ligrani, P. (2004) Numerical Predictions of Flow Structure and Local Nusselt Number Ratios Along and Above Dimpled Surfaces with Different Dimple Depths in a Channel, Numerical Heat Transfer A, No. 46, pp 549-570.

Zhang, L. W., Tafti, D. K., Najjar, F. M., and Balachandar, S. (1997) Compuatations of Flwo and Heat Transfer in Parallel-plate Fin Heat Exhcangers on the CM-5: Effects of Flow Unsteadiness and three-dimensionality, Int'l Journal of Heat and Mass Transfer, Vol. 40, No. 6, pp. 1325-1341.

Zhang, X., and Tafti, D. K. (2001) Classification and Effects of Thermal Wakes on Heat Transfer in Multilouvered Fins, Int'l Journal of Heat and Mass Transfer, Vol. 44, pp. 2461-2473.

Table 3.1: Dimpled fin geometry: Fin dimensions

Case	Fin Pitch H*/H*	Fin Length L*/H*	Fin Thickness b*/H*	Stream-wise Pitch P*/H*	No. of Cells (10^6)
1	1.0	1.0	0.1	2.0	1.77
2	1.0	1.0	0.1	2.0	1.77
3	1.0	1.0	0.1	2.0	1.88

Table 3.2: Dimpled fin geometry: Dimple dimensions

Case	Dimple depth δ^*/H^*	Dimple diameter D^*/H^*	Hole Size d^*/H^*
1	0.1	0.4	0
2	0.1	0.3	0
3	0.1	0.4	0.2

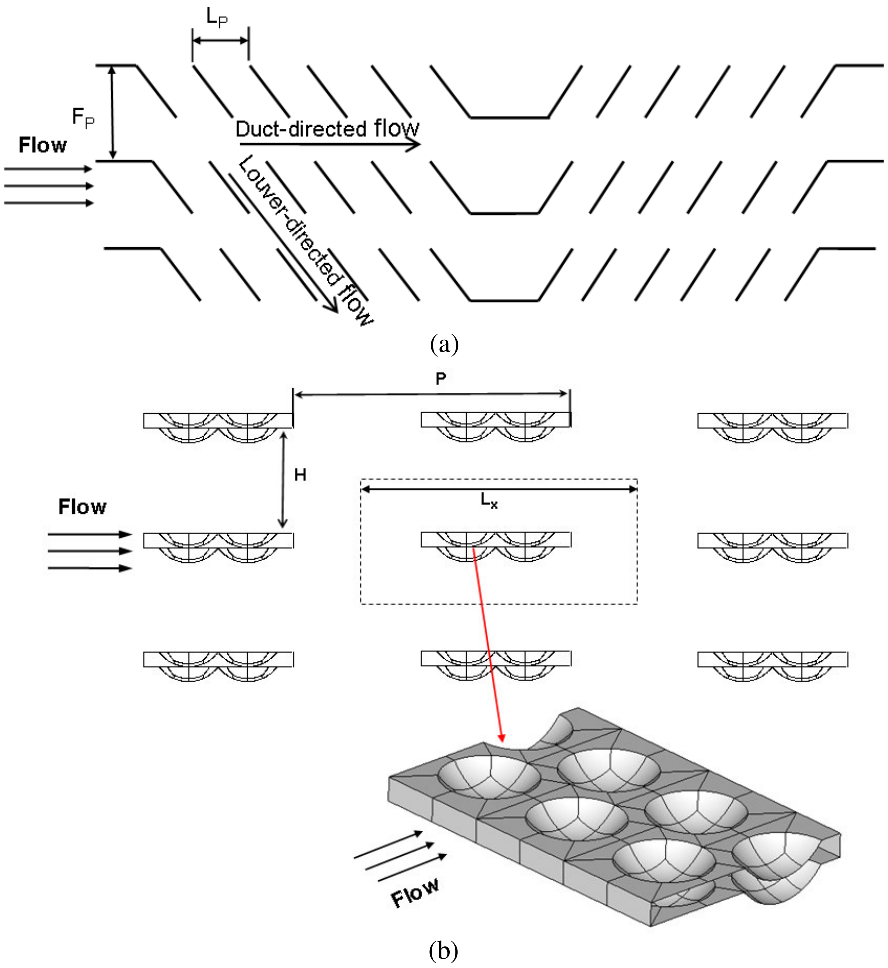

Figure 3.1: Dimpled louvered fin geometry: a) Louvered fin; b) Dimpled-louvered fin combination.

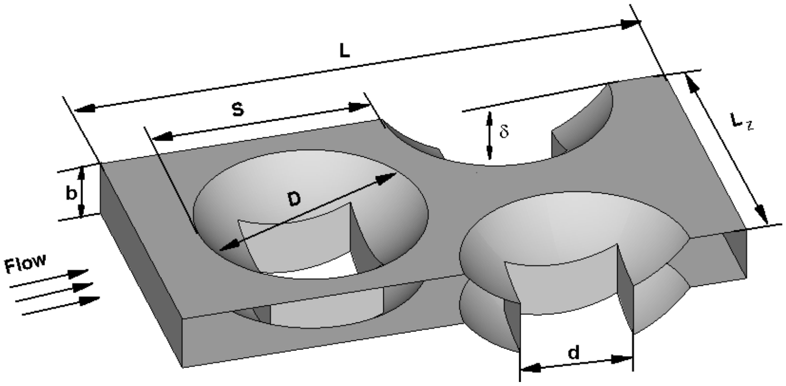

Figure 3.2: Periodic dimpled fin geometry dimensions.

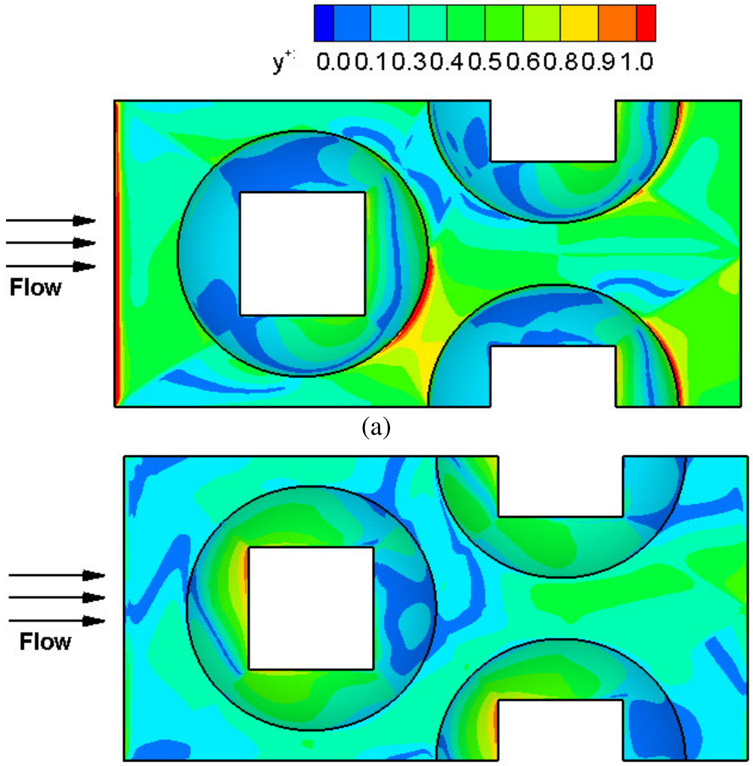

(a)

(b)

Figure 3.3: y_1^+ distribution on the fin surface for Case 3 at $Re_H = 1770$; a) Top surface; b) Bottom surface.

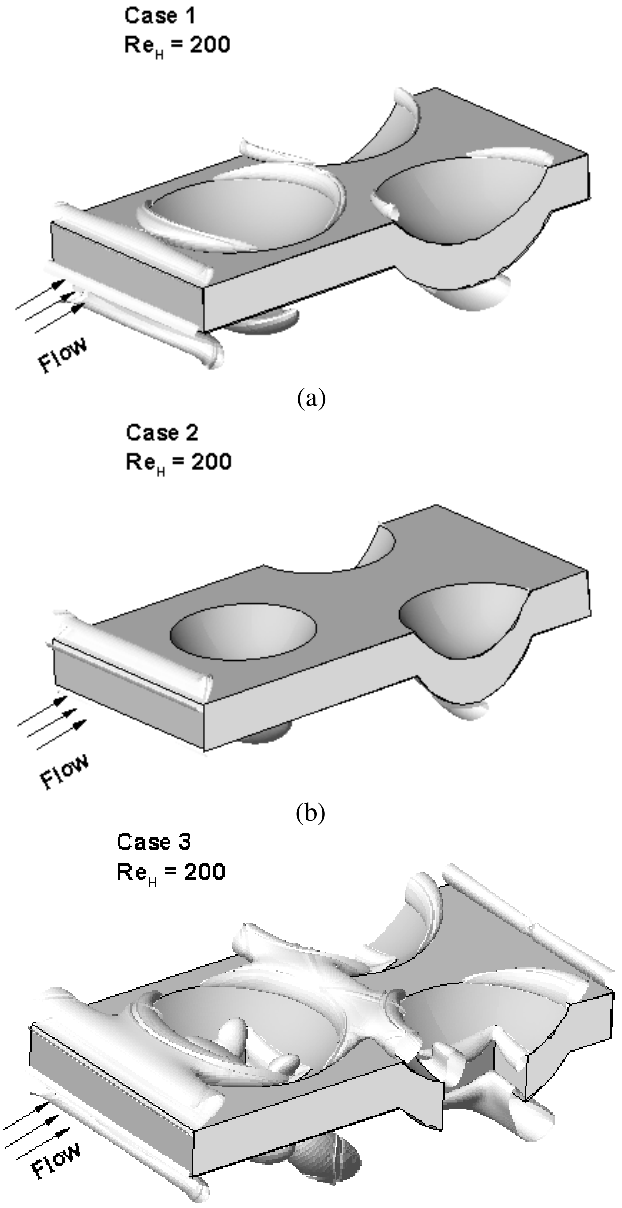

(a)

(b)

(c)

Figure 3.4: Iso-surfaces of the coherent vorticity on the top side of the dimpled fin with isosurface level = 10 at Re$_H$ = 200; a) Case 1; b) Case 2; c) Case 3

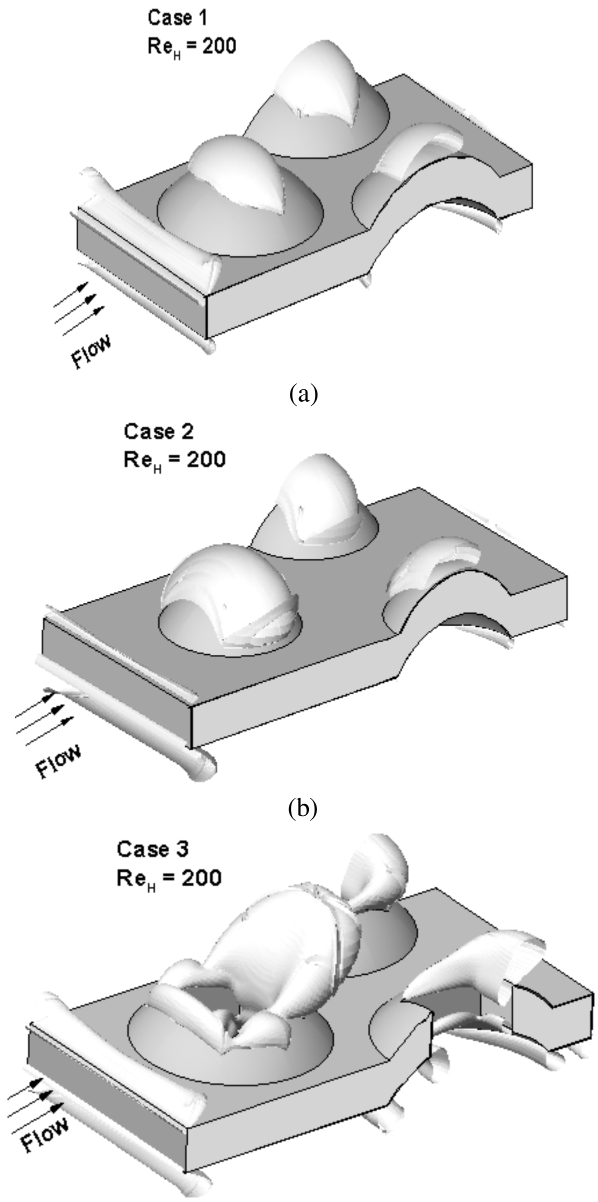

(a)

(b)

(c)

Figure 3.5: Iso-surfaces of the coherent vorticity on the bottom side of the dimpled fin with isosurface level = 10 at $Re_H = 200$; a) Case 1; b) Case 2; c) Case 3.

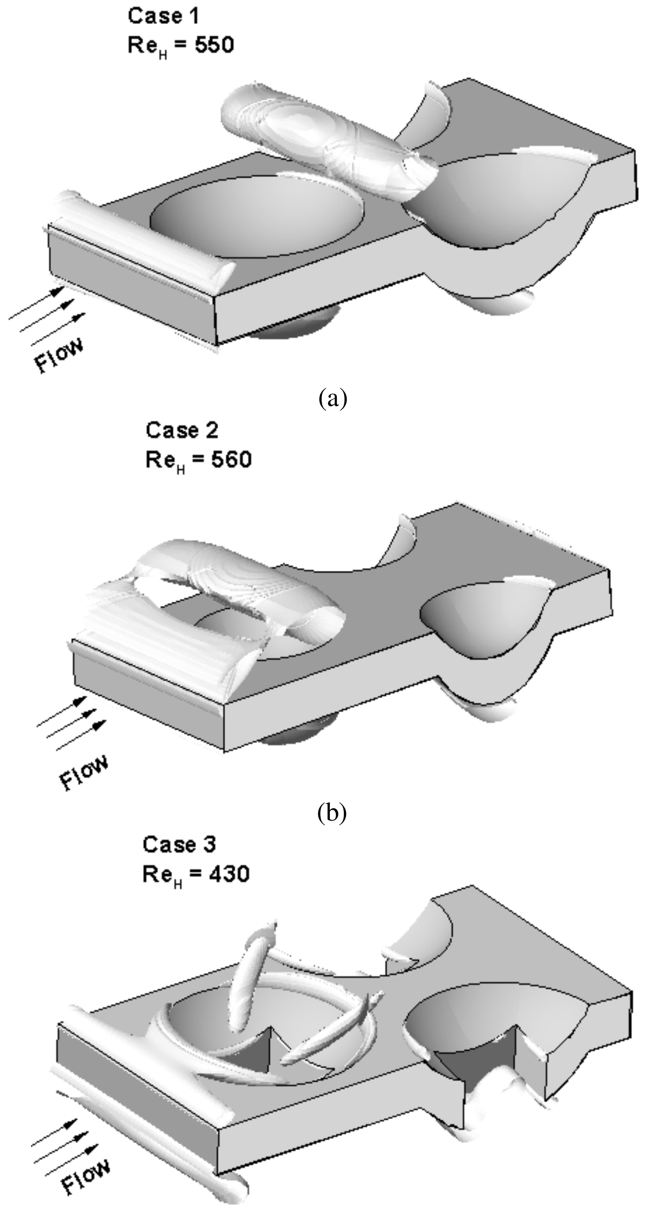

(a)

(b)

(c)

Figure 3.6: Iso-surfaces of the coherent vorticity on the top side of the dimpled fin with isosurface level = 18 at Re_H ~ 500; a) Case 1; b) Case 2; c) Case 3.

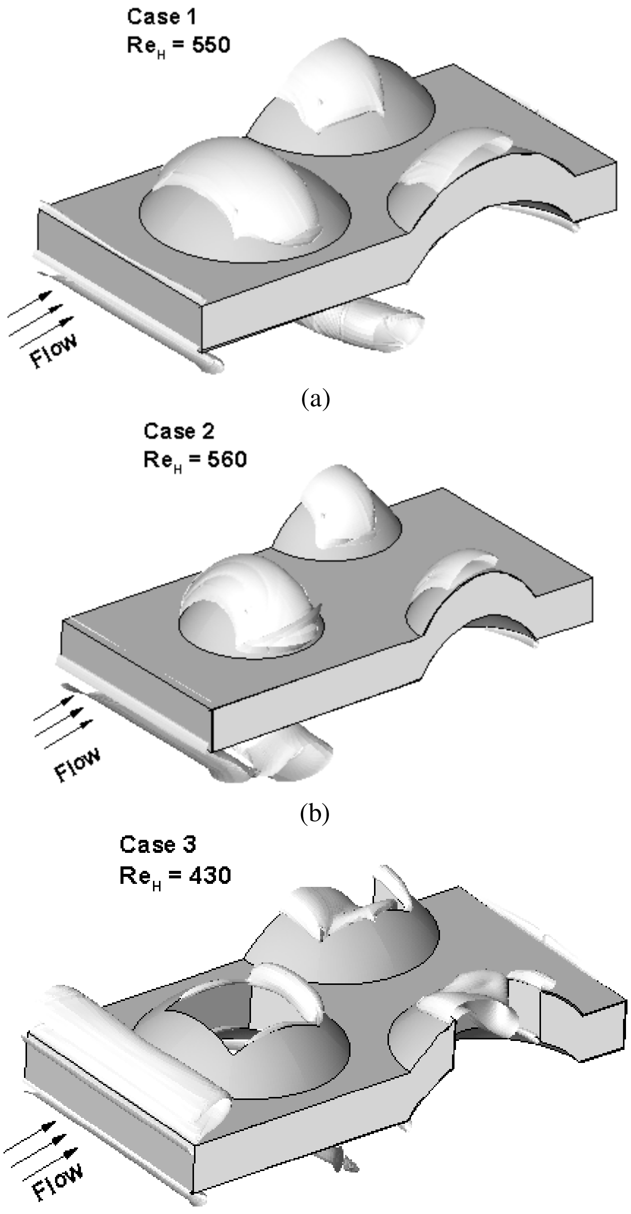

(a)

(b)

(c)

Figure 3.7: Iso-surfaces of the coherent vorticity on the bottom side of the dimpled fin with isosurface level = 18 at Re_H ~ 500; a) Case 1; b) Case 2; c) Case 3.

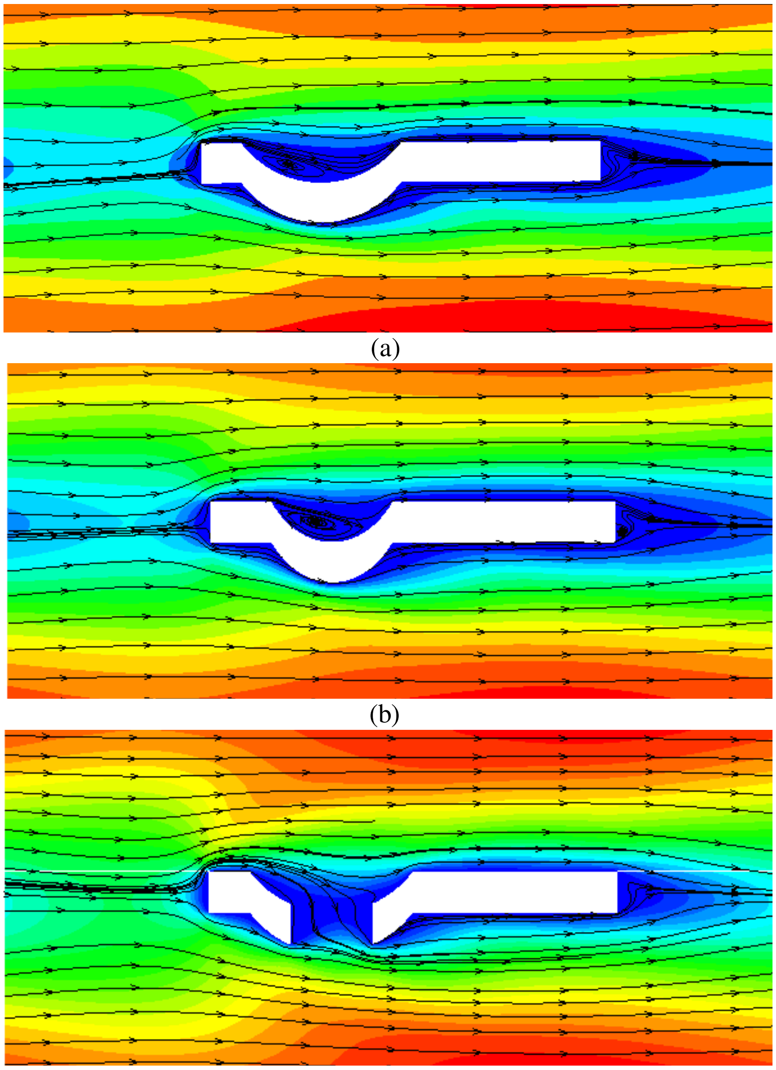

(a)

(b)

(c)

Figure 3.8: Mean velocity streamlines at stream-wise plane across centerline of domain (Z=0) at $Re_H = 200$ for: a) Case 1; b) Case 2; c) Case 3. (Stream-wise velocity contours).

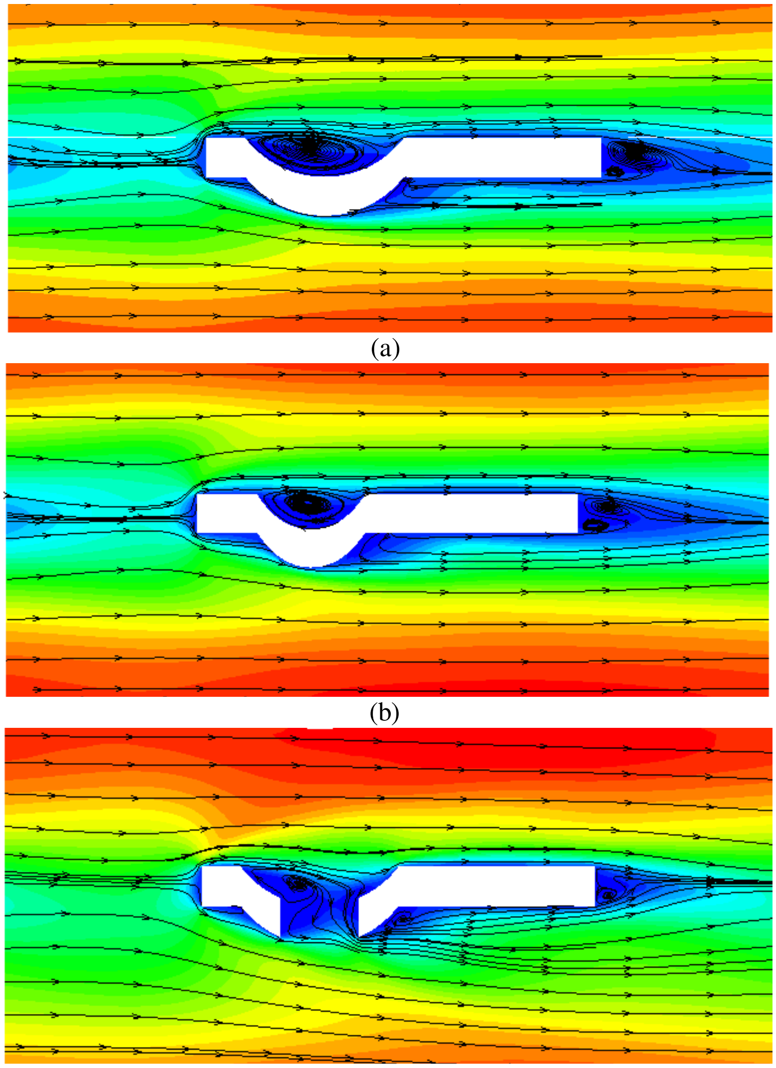

(a)

(b)

(c)

Figure 3.9: Mean velocity streamlines at stream-wise plane across centerline of domain (Z=0) of fin at Re_H ~ 900 for: a) Case 1; b) Case 2; c) Case 3. (Stream-wise velocity contours).

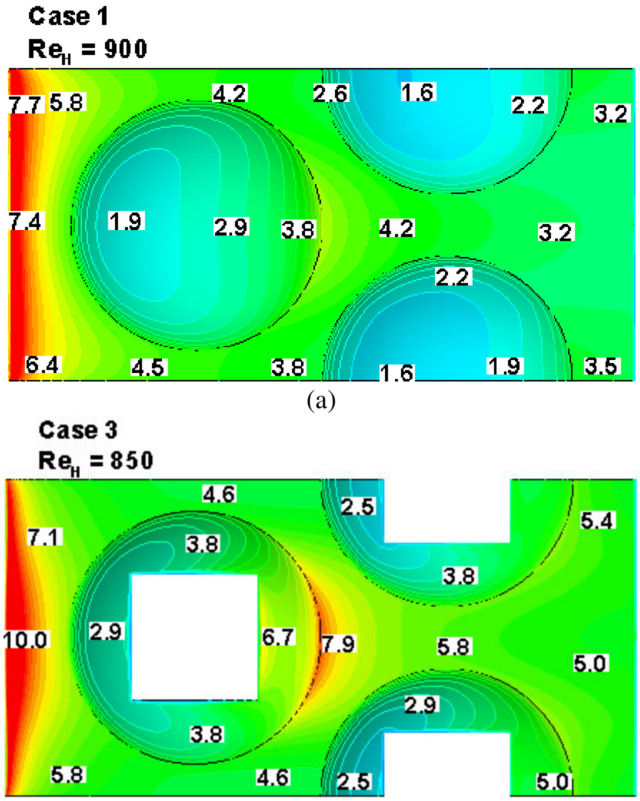

(a)

(b)

Figure 3.10: Nusselt number augmentaiton distribution on the top fin surface at Re_H ~ 900 for: a) Case1; b) Case 3.

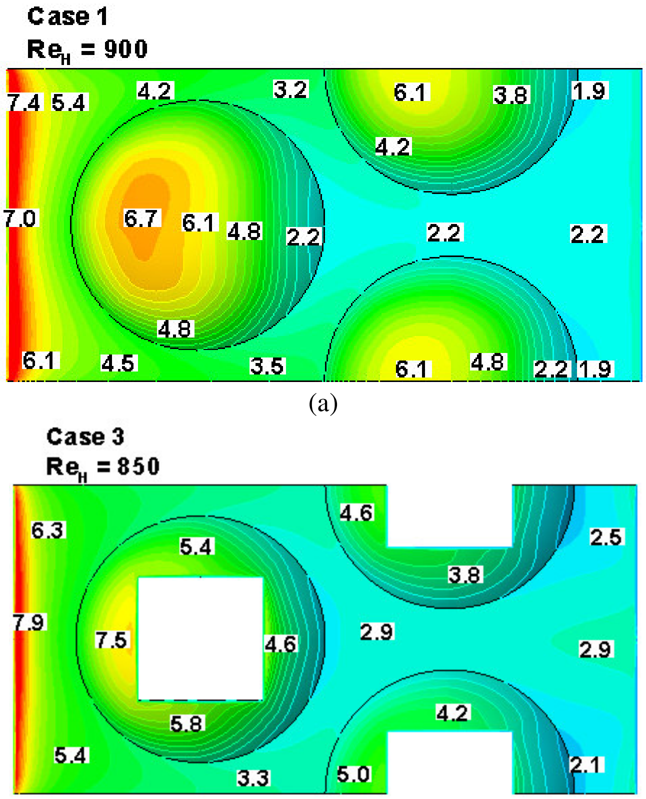

(a)

(b)

Figure 3.11: Nusselt number augmentation distribution on the bottom fin surface at Re_H ~ 900 for: a) Case1; b) Case 3.

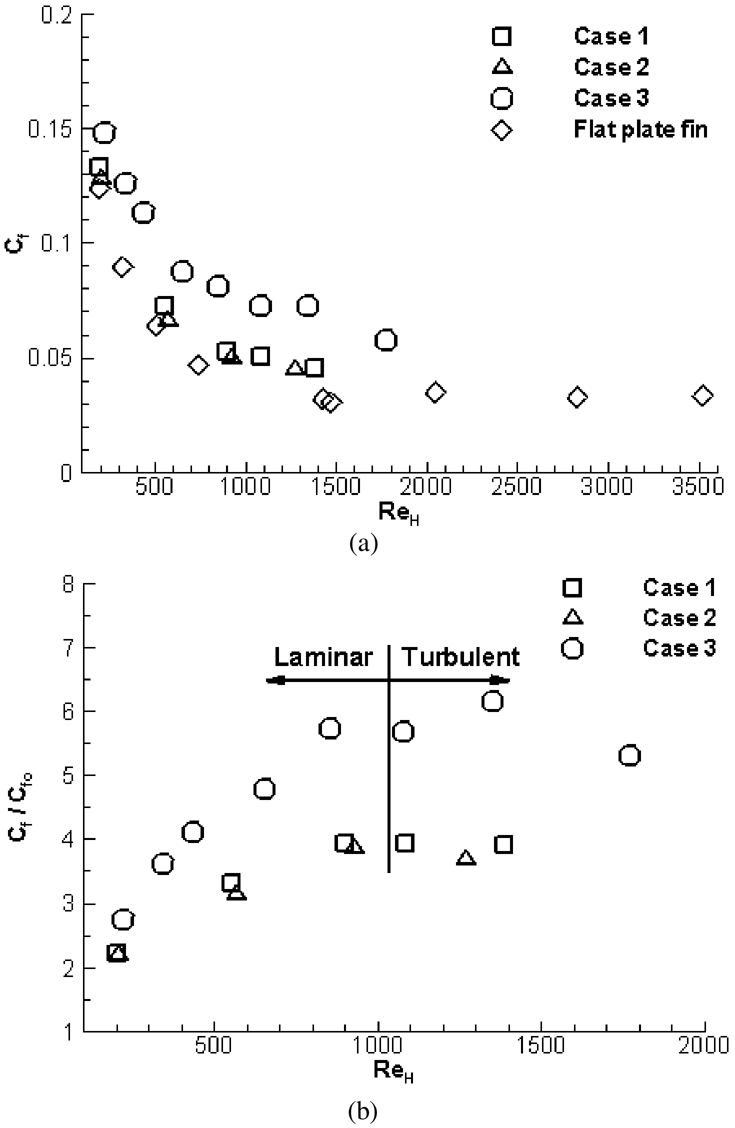

Figure 3.12: Profile of: a) C_f; b) C_f augmentation; variation with Reynolds number for the three fin cases.

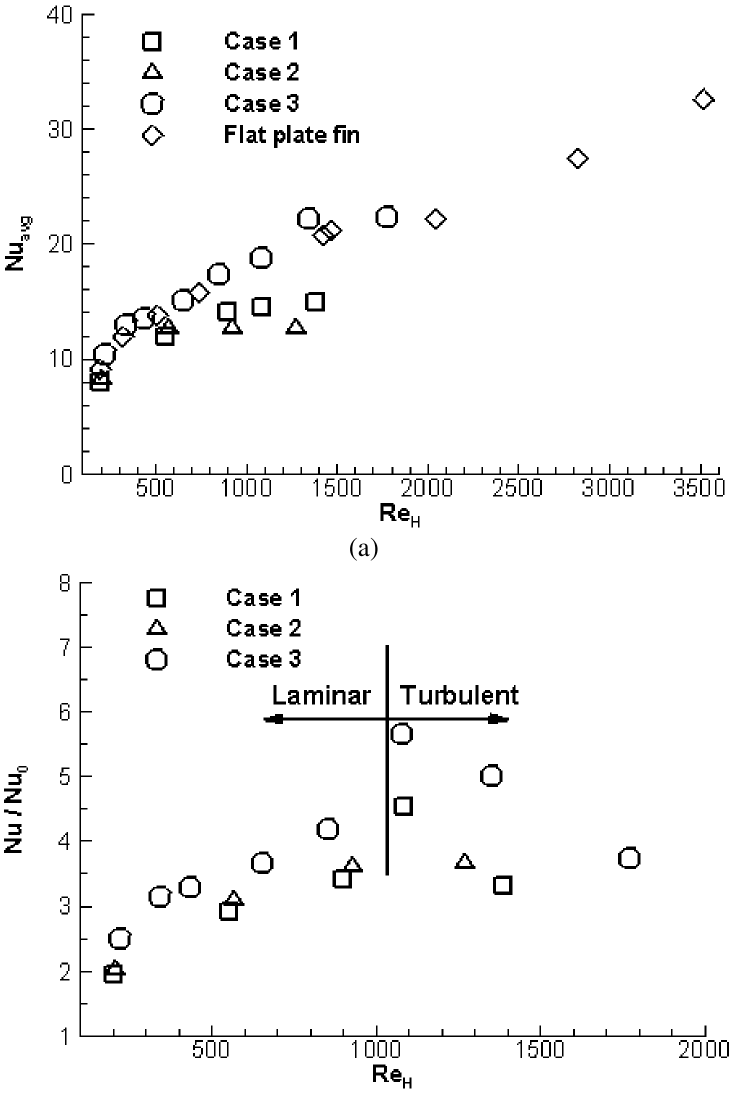

(a)

(b)

Figure 3.13: Profile of: a) Average Nu; b) Nu augmentation; variation with Reynolds number for the three fin cases.

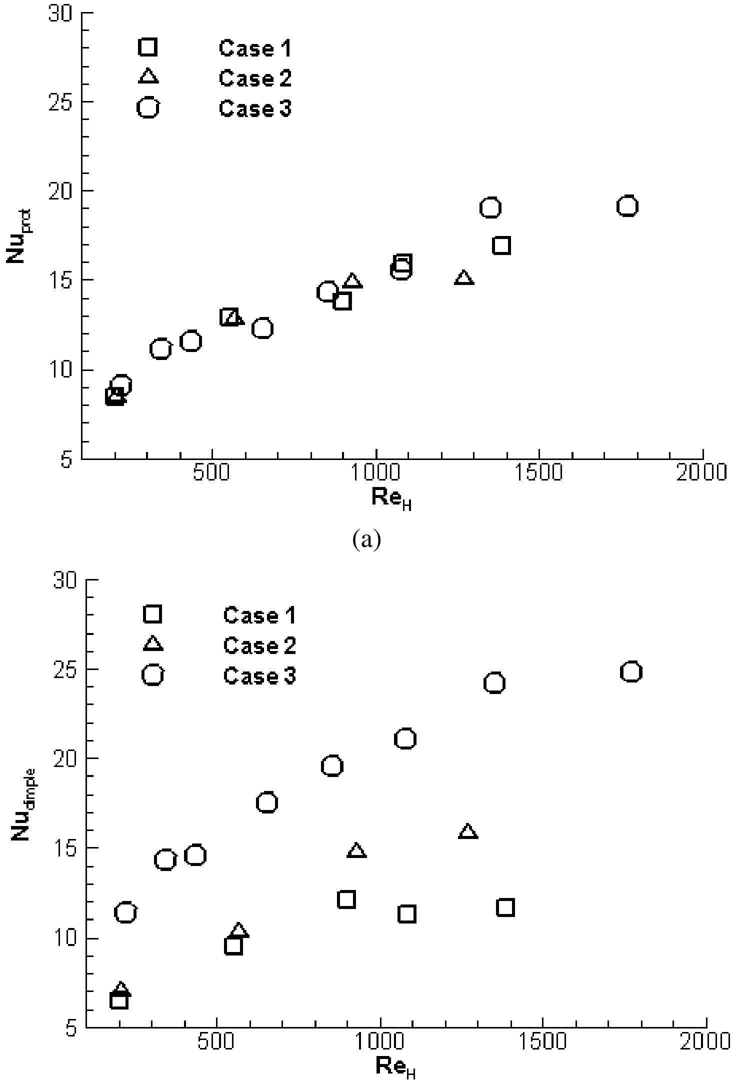

(a)

(b)

Figure 3.14: Nussselt number variation with Reynolds number for the three fin cases on: a) Protrusion surface; b) Dimple surface.

Chapter 4: A Novel Split-dimple Interrupted Fin Configuration for Heat Transfer Augmentation[1]

4.1 Abstract

The use of an interrupted plate-fin with surface roughness in the form of split-dimples is investigated. High-fidelity time-dependent calculations are performed for a wide range of Reynolds number ranging from Re_H=240 to 4000, covering the laminar to fully turbulent flow regimes. The split-dimples provide an additional mechanism for augmenting heat transfer by perturbing continuous boundary layer formation on the fin surface and generating energetic shear layers. High heat transfer regions are observed at the fin and split-dimple leading edges as a result of boundary layer restarts, in regions of flow acceleration between protrusions, and flow impingement on the protrusion surface. While the protruding geometry of the split-dimple also aids in augmenting heat transfer from the fin surface by generating unsteady or turbulent wakes, it also increases pressure losses. The split-dimple fin results in a heat conductance that is 60%-175% higher than a plain interrupted plate-fin, but at a cost of 4-8 times the frictional losses.

Keywords: Heat enhancement, fin, split-dimple, compact heat exchangers, LES.

Nomenclature

D	dimple imprint diameter
D_h	hydraulic diameter
C_f	Fanning friction coefficient
f	non-dimensional frequency based on mean velocity and fin pitch
g^{ij}	contravariant metric tensor

---

[1] This chapter is reprinted from the Int. J. Heat Mass Transfer, "A Novel Split-dimple Interrupted Fin Configuration for Heat Transfer Augmentation Investigation," Elyyan, M.A., and Tafti, D.K., doi:10.1016/j.ijheatmasstransfer.2008.07.046, with permission from Elsevier.

k	thermal conductivity
S	stream-wise pitch
H	channel Height or fin pitch (characteristic length scale)
L_x	periodic length
$\vec{n}$	surface normal vector
Nu	Nusselt number
P	span-wise pitch
p	fluctuating, modified, or homogenized pressure
Pr	Prandtl number
q''	constant heat flux on channel walls
Q_x	flow rate in the stream-wise direction
Re_τ	Reynolds number based on friction velocity (u_τ)
Re_H	Reynolds number based on mean flow velocity (u_b) and H
t	non-dimensional time based on u_τ and H
$Time$	non-dimensional time based on u_b and H
$\vec{u}$	Cartesian velocity vector
u_τ	friction velocity (characteristic velocity)
u_b	mean flow velocity
$\vec{x}$	physical coordinates
β	mean pressure gradient
δ	dimple depth
γ	mean temperature gradient
θ	fluctuating, modified, or homogenized temperature

Ω	heat transfer surface area
$\vec{\xi}$	computational coordinates

Subscripts

b	bulk
D_h	based on the channel's hydraulic diameter
f	fin surface
H	based on channel height
o	smooth channel
t	turbulent parameters
τ	based on friction velocity

Superscripts

+	wall coordinates
*	dimensional quantities

4.2 Introduction

Airside thermal resistance constitutes up to 80% of the total thermal resistance of heat exchangers. To improve the heat transfer capacity, fins are employed to increase the surface area as well as to increase the heat transfer coefficient. Fins, more often than not, use enhanced surfaces, which can broadly be classified into continuous fins with roughness or surface enhancements (e.g. wavy fins, dimpled fins)[1, 2, 3, 4, 5] or interrupted surface (e.g. offset strip, louvered, slit) [6, 7, 8]. Both surfaces are designed to disrupt the thermal boundary layer and increase mixing with the gas. At low Reynolds numbers typical of the laminar regime, surfaces interruptions are more effective than surface roughness in augmenting heat transfer.

Figure 4.1 shows the heat transfer augmentation ratio of a 2D corrugated louvered fin (without tube effects) [7, 9] compared to a continuous fin surface with dimples and protrusions as roughness elements [10]. Three typical louver geometries with varying louver angles are plotted versus two dimple geometries, which vary in dimple depth (characteristic roughness scale). Case 1 has a dimple depth of 0.2 times the channel height and Case 2 with dimple depth of 0.4. It is clear that in the low Reynolds number regime, louvered fins or more generally interrupted surfaces are far superior to the use of dimples and protrusions or more generally uninterrupted fins with roughness elements. In the example above, Case 1 with roughness depth less than the boundary layer thickness (half fin pitch for fully developed flow) shows no augmentation till the development of self-sustained flow oscillations at approximately Re_H=1000. Case 2, which has a larger dimple depth of the same order as the boundary layer thickness, induces self-sustained oscillations in the flow much earlier and as a result is successful in augmenting the heat transfer coefficient. However, in spite of this, the augmentation in heat transfer coefficient is much lower than that in louvered fins. Louvered fins, in spite of operating in the laminar regime over most of the Reynolds number range in Figure 4.1, result in high augmentation by constantly regenerating the thermal boundary layer at each louver.

Since interrupted surfaces are superior in augmenting heat transfer at low Reynolds numbers, this paper investigates the use of a hypothetical fin geometry which consists of an interrupted inline fin surface combined with the dimple geometry. However, instead of using conventional dimples and protrusions, the dimple is split into two halves which are punched in opposite directions to produce what is called a split-dimple. The geometry is shown in Figure 4.2. The objective of the paper is twofold: the first is to investigate the friction and heat transfer characteristics of the augmented geometry, and the second is to highlight the application of Large-Eddy Simulations (LES) to the complex geometrical configuration.

4.3 Governing Equations and Computational Model

The computational model assumes the flow to be fully developed hydrodynamically and thermally to allow the simulation of a periodically repeating spatial unit. Heat is applied to the fin surfaces by using a constant heat flux (q''^{*})

boundary condition at the fin walls. A characteristic length taken as the fin pitch (H^*), a characteristic velocity taken as the friction velocity, $u_\tau^* = \sqrt{\tau_{weq}^*/\rho^*}$), and a characteristic temperature given by $q''^* H^*/k$, are used to non-dimensionalize the Navier-Stokes and energy equations. Periodicity of the domain in the stream-wise (x) direction is accommodated by decomposing the stream-wise flow pressure and temperature into mean and fluctuating components. Pressure and temperature decomposition are given by

$$\begin{aligned} P^*(\vec{x},t) &= P^*_{in} - \beta^* x^* + p^*(\vec{x},t) \\ T^*(\vec{x},t) &= T^*_{in} + \gamma^* x^* + \theta^*(\vec{x},t) \end{aligned} \tag{1}$$

where β^* and γ^* are the mean gradients of pressure and temperature, respectively. On substitution into the flow and energy governing equations, the *non-dimensional* time-dependent equations in transformed coordinates $\vec{\xi} = \vec{\xi}(\vec{x})$ take the following conservative form[1]:

Continuity:

$$\frac{\partial}{\partial \xi_j}\left(\sqrt{g}U^j\right) = 0 \tag{2}$$

Momentum:

$$\frac{\partial}{\partial t}\left(\sqrt{g}u_i\right) + \frac{\partial}{\partial \xi_j}\left(\sqrt{g}U^j u_i\right) = -\frac{\partial}{\partial \xi_j}\left(\sqrt{g}(\vec{a}^{\,j})_i\, p\right) + \frac{\partial}{\partial \xi_j}\left(\left(\frac{1}{Re_\tau} + \frac{1}{Re_{t\tau}}\right)\sqrt{g}\, g^{jk}\frac{\partial u_i}{\partial \xi_k}\right) + \sqrt{g}\beta\delta_{i1} \tag{3}$$

---

[1] Henceforth, all usage is in terms of non-dimensionalized values.

Energy:

$$\frac{\partial}{\partial t}\left(\sqrt{g}\theta\right)+\frac{\partial}{\partial \xi_j}\left(\sqrt{g}U^j\theta\right)=\frac{\partial}{\partial \xi_j}\left(\left(\frac{1}{Pr\ Re_\tau}+\frac{1}{Pr_t\ Re_{t\tau}}\right)\sqrt{g}\,g^{jk}\frac{\partial \theta}{\partial \xi_k}\right)-\sqrt{g}\gamma u_1$$

(4)

where $\vec{a}^i$ are the contravariant basis vectors[1], $\sqrt{g}$ is the Jacobian of the transformation, g^{ij} are the elements of the contravariant metric tensor, $\sqrt{g}U^j = \sqrt{g}(\vec{a}^j)_i u_i$ is the contravariant flux vector, $\vec{u}_i$ is the Cartesian velocity vector, and θ is the modified temperature. The non-dimensional mean pressure and temperature gradients are found from mean momentum and energy balances, respectively, as

$$\beta=\frac{4}{D_h}$$

$$\gamma=\frac{\Omega}{Re_\tau\ Pr\ Q_x L_x}$$

(5)

More details about the modified fully developed treatment can be found in Zhang *et al.* [[24]].

Re_{t_τ} is the inverse of the non-dimensional turbulent eddy-viscosity and it is modeled by the Smagorinsky model as

$$\frac{1}{Re_{t_\tau}}=C_s^{\,2}(\sqrt{g})^{2/3}\left|\overline{S}\right|$$

(6)

where $\left|\overline{S}\right|$ is the magnitude of the resolved strain rate tensor given by $\left|\overline{S}\right|=\sqrt{2\overline{S_{ik}}\,\overline{S_{ik}}}$. The Smagorinsky constant ($C_s^{\,2}$) is obtained via the dynamic subgrid stress model [[25]]. The turbulent Prandtl number is assumed to have a constant value of 0.5 [[26]].

A conservative finite-volume formulation using a second-order central difference scheme on a non-staggered grid topology is used to discretize the governing equations. In this scheme, the flow velocity and scalar variables are calculated and stored at the cell center, whereas the contravariant fluxes are calculated and stored at the cell faces. Temporal advancement is performed using a two-step projection method. An

---

[1] The notation $\left(\vec{a}^j\right)_k$ is used to denote the *k-th* component of vector $\vec{a}^j$. $(\vec{a}^j)_k = \partial\xi_j/\partial x_k$

intermediate velocity field is calculated at the predictor step, which is then updated at the corrector step by satisfying discrete continuity.

The computer program GenIDLEST (Generalized Incompressible Direct and Large-Eddy Simulations of Turbulence) is used for the current study. GenIDLEST has been applied extensively to air-side heat transfer augmentation calculations and validated with experimental results in the literature, e.g. Cui and Tafti [27], Sewall *et al.* [28] and Elyyan *et al.* [10]. Details about the algorithm, functionality, and capabilities can be found in Tafti [29].

4.4 Calculation of Friction and Heat Transfer Coefficients

Low pressure drop and high heat transfer rate are the goals of any new fin shape design, and in order to quantify these characteristics the Fanning friction coefficient and Nusselt number are used to evaluate the performance of the split-dimple fin. The Fanning friction coefficient is calculated as

$$C_f = \frac{\tau_s^*}{\rho^*(u_b^*)^2/2} = \frac{-(\Delta \overline{p}_x^* / L_x^*) D_h^*}{2\rho^*(u_b^*)^2} \tag{7}$$

where D^*_h is the dimensional hydraulic diameter of the fin. Non-dimensionalizing with the corresponding characteristic length and velocity and substituting for the mean pressure gradient from equation (5) result in

$$C_f = \frac{D_h}{2u_b^2} \tag{8}$$

The fin surface heat transfer is characterized by a surface averaged Nusselt number, Nu, which is calculated as

$$Nu = \frac{h^* H^*}{k^*} = \frac{q''^* H^* \Omega_f^*}{k^* \int (T_s^* - T_{ref}^*) d\Omega_f^*} \tag{9}$$

where h^* is the average convective heat transfer coefficient of the surface, k^* is the thermal conductivity, q''^* is the wall heat flux, T_s^* is the fin surface temperature, and T_{ref}^* is a reference temperature, respectively. Non-dimensionalizing with the corresponding characteristic length and temperature scales the Nusselt number can be rewritten as

$$Nu_{avg} = \frac{\Omega_f}{\iint(\theta_s - \theta_{ref})d\Omega_f} \tag{10}$$

where θ_s and θ_{ref} are the local modified non-dimensional fin surface and reference temperatures, respectively. The reference temperature is the volume-averaged temperature of the domain found by integrating the heat flux over the entire volume

$$\theta_{ref} = \frac{\int\iint |u|\, \theta\, dA_x\, dx}{\int\iint |u|\, dA_x\, dx} \tag{11}$$

4.5 Baseline Friction and Heat Transfer Coefficients

The performance of the new fin geometry is evaluated by comparing its friction coefficient and Nusselt number to that of a smooth parallel-plate channel. The laminar friction coefficient and Nusselt number for a smooth parallel-plate channel with fin pitch (H^*) are given by

$$C_{fo}=12/Re_H; \quad Re_H<1500 \tag{12}$$

$$Nu_0=4.12; \quad Re_H<1500 \tag{13}$$

and for the turbulent regime, the Peutokhov and Gnielinski correlations for the friction coefficient and Nusselt number, respectively, are used [[30]]

$$C_{f_0} = (1.580 \ln Re_H - 2.185)^{-2} \qquad ;1500 \le Re_H \le 2.5\times10^6 \tag{14}$$

$$Nu_0 = \frac{(C_{f_0}/2)(Re_H - 500)Pr}{1 + 12.7(C_{f_0}/2)^{1/2}(Pr^{2/3} - 1)} \qquad ;1500 \le Re_H \le 2.5\times10^6 \tag{15}$$

Note that the hydraulic diameter for a smooth parallel-plate channel is equal to twice the fin pitch ($D_h^* = 2H^*$), i.e. ($Re_{Dh} = 2Re_H$). Thus, the original Peutokhov and Gnielinski correlations are rewritten here in terms of Re_H rather than Re_{Dh}.

4.6 Fin Geometry, Computational Domain, and Grid Independency

The fin geometry is composed of a parallel inline fin array, which is assumed to be infinite in the span-wise direction. Two rows of split-dimples modify the fin surface as shown in Figure 4.2. Figure 4.2-b shows the fin's smallest repeatable spatial unit that can be used to represent the fin geometry; this spatial unit is used in the current study. The computational domain is assumed to be periodic in the span-wise, stream-wise, and transverse directions. Table 4.1 summarizes the computational domain's geometry specifications non-dimensionalized by the fin pitch ($Fp^* = H^*$).

A grid independency study is conducted for the split-dimple fin geometry; where three grid resolutions have been tested. All of the grid cases used 288 structured/unstructured grid blocks to represent the fin geometry, Figure 4.2-c. In order to resolve the near wall turbulence at the fin surface, a fine mesh resolution is placed in the vicinity of the surface. The same grid distribution was used in the direction normal to the fin surface for all three cases. While the finest grid consisted of 3.6 million cells, the next level was constructed by coarsening in the span-wise direction to 1.93 million cells, and the coarsest level of 1.16 million cells was obtained by coarsening both the span-wise and stream-wise directions. All grid cases are tested at a nominal Reynolds number of 4000, which is the highest Reynolds number considered in this paper. Calculations are started with an initial guess for the velocity and temperature fields in the domain and allowed to develop in time under the specified pressure drop until the flow is fully developed and stationary, after which temporal averaging for mean and turbulent quantities is initiated.

Table 4.2 summarizes the friction coefficient and surface averaged Nusselt number values for the split-dimple fin for the three grids, with Case 3, the finest mesh case, taken as a reference for comparison. It is found that the difference in the friction coefficient and Nusselt number for the three grid cases is less than 1.5%. In spite of this, due to the complexity of the fin shape and the desire to perform a very accurate analysis of the flow structures, turbulent statistics, and heat transfer distribution in the domain, the finest grid of 3.6 million cells is used for all the calculations.

In addition to the grid independency study, the sufficiency of the 3.6 million resolution was further verified by checking the y^+ distribution obtained through an *a-*

posteriori calculation of the local friction velocity at the highest Reynolds number simulated in this study (Re_H=4000). Figure 4.3 shows the y_1^+ distribution of the first grid point normal to the wall surface at the top and bottom sides of the fin. The distribution shows that the condition of $y_1^+<1$ is satisfied for most of the fin surface except for small regions at the bottom where the maximum y_1^+ value is 4.9. This guarantees the existence of at least one point inside the laminar sublayer of the flow. The wall parallel mesh distribution maintains a maximum value of $\Delta^+_{//} = 40$ at the highest Reynolds number simulated.

In order to evaluate the performance of the split-dimple fin, numerical simulations of a smooth plate fin are conducted. The dimensions and boundary conditions of the plate fin are selected to match those of the split-dimple fin with fin pitch of 1, fin length of 1.2, fin thickness of 0.1, and domain length of 2.4. Two computational domains are used in the calculations: (i) a 2D domain constructed using 10 mesh blocks and 46,080 cells used for low Reynolds number flows (Re_H<1400); (ii) a 3D domain constructed with 20 grid blocks and 442,368 cells applied for higher Reynolds number flows (Re_H>1400).

4.7 Results and Discussion

Numerical simulations of the split-dimple fin covered a wide range of Reynolds number flows, Re_H=250–4000, ranging from laminar to fully turbulent flows. Calculations are initiated with an initial guess for the velocity and temperature fields in the domain, and the flow is then allowed to develop with time under the prescribed pressure gradient. At a stage when the velocity or flow rate exhibits a stationary signal, which is constant for steady flow or one with a constant mean value for unsteady flows, temporal averaging is activated to obtain time-mean quantities for unsteady flows. The typical averaging time ranges between 2.5 and 6 time units or between 2 and 5 domain flows through time units. The plate fin calculations covered a Reynolds number range of Re_H=300–3700.

4.7.1 Instantaneous Flow Structure

Figure 4.4 shows the time-history of the stream-wise velocity at Re_H=360, 460, 570, and 1100 at three locations: near the protrusion at the fin's top surface, inside the dimple cavity, and near the protrusion's surface at the fin's bottom side. The velocity signals at Re_H=360 show close to steady laminar flow with some very low amplitude oscillations for the selected locations. These low amplitude oscillations are suspected to be remnants from the higher Re_H run from which the calculation was initiated. For all practical purposes, the flow at Re_H =360 is steady. At Re_H=460, the flow shows signs of unsteady flow with a dominant non-dimensional frequency (fU_b/H) of 0.72. As the Reynolds number increases to Re_H= 570 and 1100, the range of frequencies increase as secondary instabilities develop and the flow becomes chaotic and eventually turbulent. In comparison, the plate fin shows low amplitude periodic oscillations at Re_H=330 signifying the developing instability in the leading edge shear layer at a fundamental non-dimensional frequency of 0.34. These oscillations keep growing till they become chaotic at Re_H=1330, as seen in Figure 4.5.

Figure 4.6 shows the educed coherent-vorticity at Re_H=1100 (level=25) and 4000 (level=50) on the fin's top and bottom sides. The coherent-vorticity is identified by the vortex-eduction technique proposed by Chong *et al.* [18]. Roller or span-wise aligned vortices are shed from the fin's leading edge and the leading edge of the protrusion on the fin's top surface. The shed vortices convect downstream, where some of them impinge at the downstream protrusion's inner surface and are redirected to the fin's bottom side through the split-dimple opening. On the fin's bottom surface, once again roller vortices are shed from the leading edge of the fin. These roller vortices are deformed by the flow accelerating around the protrusion and form a horseshoe like vortex at the leading edge of the protrusion. There is considerable vorticity ejected out of the split-dimple opening. At the lower Re_H=1100, the ejected vortices take an elongated hairpin like shape, which degenerates to small scale vorticity (turbulence) at Re_H=4000.

4.7.2 Mean Flow Structure

Figure 4.7 shows three-dimensional mean flow features by injecting mean velocity streamlines close to the fin's top (left) and bottom (right) surfaces at Re_H = 240, 1100 and 4000, covering laminar to fully turbulent regimes.

Figure 4.8 plots the streamlines in a 2D stream-wise plane (z = 0). Several important flow features which influence heat transfer are present in the domain.

- Large flow recirculation zone in the wake of the protrusion at the fin's top side. As the Reynolds number increases, the reattachment length of the wake decreases due to higher flow momentum and turbulence.
- Recirculation region inside the dimple cavity on the fin's top side as the flow separates at the upstream edge of the dimple at Re_H=1100 and 4000. As the Reynolds number increases from Re_H=1100–4000, the recirculation zone's size shrinks. A much smaller recirculation zone is observed for the laminar flow at Re_H=240.
- Flow impingement at the protrusion's front surface on the fin's bottom side, and at the inner protrusion's surface on the fin’s top side.
- A swirling jet issuing from the split-dimple cavity as seen at the fin's bottom side. The flow redirection from the fin's top side to its bottom side through the dimple cavity results from the low pressure in the wake of the protrusion at the bottom. Swirl is imparted to the flow by the curved edges of the dimple cavity. Due to the partial blocking of the dimple cavity by the recirculating flow inside it, the redirected flow through the split-dimple opening eject in an-almost normal direction to the main flow. Upon exiting the split-dimple opening, the redirected flow is partially realigned by the mainstream flow. Due to the larger blocking and faster redirected flow as the Reynolds number increases, flow realignment becomes weaker.
- A horseshoe type vortex is observed at the upstream rim of the protrusion on the bottom side of the fin for Re_H=1100 and 4000. This horseshoe vortex is formed by the separated shear layer from the fin's leading edge, which accelerates and elongates around the protrusion's surface. The 3D horseshoe vortex is seen in Figure 4.6 and as a small recirculating region in Figure 4.7.

- Flow acceleration through the narrow passage between protrusions at the fin's top and bottom sides.

4.7.3 Turbulent Statistics

Turbulent kinetic energy (TKE) levels give a good indication of the heat transfer rate from the fin's surface, where high TKE values indicate strong flow mixing and high heat transfer, and vice versa. Figure 4.9 shows the TKE distribution, normalized by the mean bulk velocity squared, for the fully turbulent flow at Re_H=4000 at stream-wise locations starting from the downstream edge of the dimple cavity, x=-0.15, to the next dimple cavity's downstream edge, x=0.45. The main sources of turbulent kinetic energy production are the separated shear layers, which form at the leading (labeled A in Figure 4.8) and trailing edges of the protrusion (labeled B) on the fin's top and bottom sides, respectively, and through the shear imparted to the jet issuing from the dimple cavity (labeled C). While the TKE produced in A stays close to the surface of the fin due to reattachment, the TKE in B and C is transported away from the fin surface.

Figure 4.10 shows the normalized TKE profile at selected stream-wise locations along the fin's centerline (z=0) for the flow at Re_H=1100, 2000 and 4000. The TKE profiles peak at the flow separation from the protrusion's surface on the fin's top surface, x=-0.15 (A in Figure 4.8). This peak occurs at almost the same y-location for the three flows (y=0.3), and the highest value occurs for the fully turbulent flow of Re_H=4000. As the flow moves downstream, the TKE peak diffuses towards the fin surface. Note that the TKE levels at Re_H=2000 approach those at Re_H=4000 in the flow reattachment region downstream of the protrusion, (x=0, and 0.15). The maximum TKE ranges between 20 and 30% at Re_H=4000.

On the bottom side of the fin, dual peaks appear at the split-dimple opening for the fully turbulent flows at Re_H=2000 and 4000, while a single rather weak peak exists for the flow at Re_H=1100. The dual peaks result from the shear imparted to the flow exiting the split-dimple cavity (C) and the interaction of the outer flow and flow issuing from the cavity (B). These peaks convect downstream of the split-dimple's opening (x=0, and 0.3), where they diffuse and move away from the fin's surface.

4.7.4 Heat Transfer Distribution

Heat transfer augmentation results from the disruption of the thermal boundary layer, flow impingement, and flow instabilities or turbulence. Boundary layer regeneration is the dominant mechanism at low Reynolds numbers, which is augmented by flow instabilities as the Reynolds number increases. The temperature difference ($\theta_s - \theta_{ref}$) is an indicator of the local variation in heat transfer coefficient as given by equation 9, where low values indicate regions of high heat transfer coefficients, and larger values occur in regions of low heat transfer coefficients.

Figure 4.11 and Figure 4.12 show ($\theta_s - \theta_{ref}$) distribution on the top and bottom fin surfaces, respectively, for the flow at Re_H=240, 1100 and 4000. Regions of high heat transfer, small ($\theta_s - \theta_{ref}$), exist at (i) boundary layer regeneration at the leading edge of the fin, leading edge of the protrusion on the top surface, and downstream of dimple on the bottom surface, (ii) velocity acceleration zone in the narrow passage between protrusions, especially at high Reynolds numbers, (iii) flow impingement region at the protrusion's outer and inner faces, (iv) flow reattachment region in the wake of the protrusion on the top surface, and (v) the junction eddy at the protrusion's leading edge at the fin's bottom surface for the turbulent flows at Re_H=1100 and 4000.

Conversely, regions of low heat transfer, large ($\theta_s - \theta_{ref}$), exist at (i) flow recirculation region inside the dimple cavity and downstream of the protrusion, and (ii) in the wake of the split-dimple opening at the fin's bottom side. Note that the size of the high ($\theta_s - \theta_{ref}$) zone in the wake of the protrusion shrinks with increasing Reynolds number of the flow, and it is almost unnoticeable at the fully turbulent flow case at Re_H=4000. This agrees with the early flow reattachment observed earlier for the fully turbulent flows, Figure 4.7-c and Figure 4.8 (Re_H=4000). In general, as the Reynolds number increases, the ($\theta_s - \theta_{ref}$) range becomes smaller and more uniform in distribution, which indicates strong flow mixing for turbulent flows.

4.7.5 Average Friction and Heat transfer Coefficient

Figure 4.13 shows the Nusselt number and its augmentation for the split-dimple and plate fin. Better heat transfer performance is obtained with the split-dimple fin over the plate fin with 40−120% increase of Nusselt number. Moreover, the split-dimple fin has a heat transfer area that is 45% larger than the plate fin, which results in an additional increase of split-dimple fin heat conductance ($h\Omega$). Thus, the conductance is increased between 60 and 175% over the plate fin.

Figure 4.14 shows the friction coefficient and its augmentation ratio compared to a plain channel flow for both the split-dimple and plate fins. As expected, the split-dimple fin produces much larger pressure drop than the plate fin; where the extra protuberances introduced into the flow by the split-dimple fin geometry produce a significant increase in flow resistance. The split-dimple fin's friction coefficient is 4–8 times that of the plate fin.

4.8 Summary and Conclusions:

Time-dependent high-fidelity calculations have been conducted for a hypothetical fin shape, combining an interrupted plate fin with surface roughness in the form of split-dimples covering a wide range of Reynolds numbers Re_H=250–4000. Detailed investigation of the transient and fully turbulent flow structures, turbulent statistics, and heat transfer distribution showed the following major flow and thermal features:

- The split-dimple geometry augments the overall effectiveness of the interrupted fin by disrupting the thermal boundary layer which forms on the fin surface.
- Shear layers induced by the split-dimple geometry enhance turbulence levels in the flow and heat transfer from the fin surface. TKE levels as high as 30% are observed in the vicinity of the split-dimple.
- The windward surfaces of the split-dimple also contribute to heat transfer augmentation through the mechanism of flow impingement. High heat transfer is also observed at the flow acceleration zone between protrusions.
- Flow separation and large wakes are induced by the protruding split-dimple geometry, which reduce heat transfer and increase pressure losses in the flow. The fin surface downstream of the protrusion on both sides, and the surface inside the dimple cavity are examples of these regions. As the Reynolds number increases, these regions become smaller due to enhanced mixing.

- Overall, the split-dimple fin has 60%−175% higher heat transfer capacity than the plate fins, but with 4−8 times the frictional losses.

Future work should focus on modifications for reducing the friction penalty.

4.9 Acknowledgments

This work is a result of support provided by the US Army RDECOM, Fort Belvoir, VA and Modine Manufacturing Co., Passenger Thermal Management, Racine, WI for air-side heat transfer enhancement in next generation compact heat exchangers. The support is gratefully acknowledged. The calculations were performed on Virginia Tech's Advanced Research Computing facility, System-X.

4.10 Reference

1. Wang, C.C., Fu, W.L., Chang, C.T., Heat Transfer and Friction Characteristics of Wavy Fin-and-Tube Heat Exchangers. Experimental Thermal and Fluid Sciences 14 (1998) 174-186.
2. Junqi, D., Jiangping, C., Zhijiu, C., Yimin, Z., Wenfeng, Z., Heat Transfer and Pressure Drop Correlations for the Wavy Fin and Flat Tube Heat Exchangers. Applied Thermal Engineering 27 (2007) 2066-2073.
3. Ligrani, P.M., Harrison, J.L., Mahmood, G.I., Hill, M.L., Flow Structure Due To Dimple Depressions on a Channel Surface. Physics of Fluids 13 (11) (2001) 3442-3451.
4. Moon, H.K., O'Connell, T.O., Sharma, R., Heat Transfer Enhancement Using a Convex-Patterned Surface. Journal of Turbomachinery 125 (2003) 274-280.
5. Burgess, N.K., Oliveira, M.M., Ligrani, P.M., Nusselt Number Behavior on Deep Dimpled Surfaces within a Channel. Journal of Heat Transfer 125 (2003) 11-18.
6. Dong, J., Chen, J., Chen, Z., Zhou, Y., Air-side Thermal Hydraulic Performance of Offset Strip Fin Aluminum Heat Exchangers. Applied Thermal Engineering 27 (2007) 306-313.

7. Tafti, D.K., Zhang, L.W., Wang, G., Geometry Effects on Flow Transition in Multilouvered Fins – Onset, Propagation, and Characteristics of Frequencies. Int. J. Heat Mass 44 (2001) 4195-4210.
8. Wang, C.C., Tao, W.H, Chang, C.J., An Investigation of the Airside Performance of the Slit fin-and-tube Heat Exchangers. Int. J. of Refrigeration 22 (1999) 595-603.
9. Zhang, X. Tafti, D.K., Classification and Effects of Thermal Wakes on Heat Transfer in Multilouvered Fins. Int. J. Heat Mass Transfer 44 (2001) 2461-2473.
10. Elyyan, M.A., Rozati, A., Tafti, D.K., Investigation of Dimpled Fins for Heat Transfer Enhancement in Compact Heat Exchangers. Int. J. Heat Mass Transfer, 51 (2008) 2950-2966.
11. Zhang, L., Tafti, D., Najjar, F., and Balachander, S., Computations of Flow and Heat Transfer in Parallel-plate Fin Heat Exchangers on the CM-5: Effects of Flow Unsteadiness and Three-dimensionality. Int. J. Heat Mass Transfer 40 (66) (1997) 1325-1341.
12. Germano, M., Piomelli, U., Moin, P., and Cabot, W.H., A Dynamic Subgrid-Scale Eddy Viscosity Model. Phys. Fluids 3 (1991) 1760-1765.
13. Moin, P. Squires, K., Cabot, W., Lee, S., A Dynamic Sub-Grid-Scale Model for Compressible Turbulence and Scalar Transport. Phys. Fluids A 3 (11) (1991) 2746-2757.
14. Cui, J. and Tafti, D. K., Computations of Flow and Heat Transfer in a Three-Dimensional Multilouvered Fin Geometry. Int. J. Heat Mass Transfer 45 (2002) 5007-5023.
15. Sewall, E.A., Tafti, D.K., Graham, A.B., Thole, K.A., 2006. Experimental validation of large eddy simulation of flow and heat transfer in a stationary ribbed duct. Int. J. Heat and Fluid Flow 27 (2) (2006) 243-258.
16. Tafti, D.K., GenIDLEST – A Scalable Parallel Computational Tool for Simulating Complex Turbulent Flows. Proc. ASME Fluids Engineering Division, FED 256 (2001) 346-357.
17. Incropera, F., and DeWitt, Fundamentals of Heat and Mass Transfer, fifth ed., Wiley, New York, 2001, pp. 463-493.

18. Chong, M., Perry, A, and Cantwell, B. J. A General Classification of Three-Dimensional Flow Fields. Physics of Fluids A 2 (1990) 765-777.

Table 4.1: Split-dimple fin geometry specifications.

Fin Geometry Specifications			
Fin Pitch H	Domain Length L_x	Fin Length L	Fin Thickness b
1.0	2.4	1.2	0.1

Split-dimple Specifications				
Dimple Outer Diameter d_o	Dimple Inner Diameter d_i	Dimple Streamwise Pitch S	Dimple Spanwise Pitch P	Dimple Depth δ
0.5	0.3	1.2	0.6	0.15

Table 4.2: Grid independency test results.

Case	No. of Cells	Re_H	C_f	%Diff	Nu_{avg}	Max %Diff
1	1.16E+06	4022	0.283	0.55	69.6	1.22
2	1.93E+06	4033	0.281	1.10	70.4	0.10
3	3.58E+06	4011	0.284	**Ref.**	70.4	**Ref.**

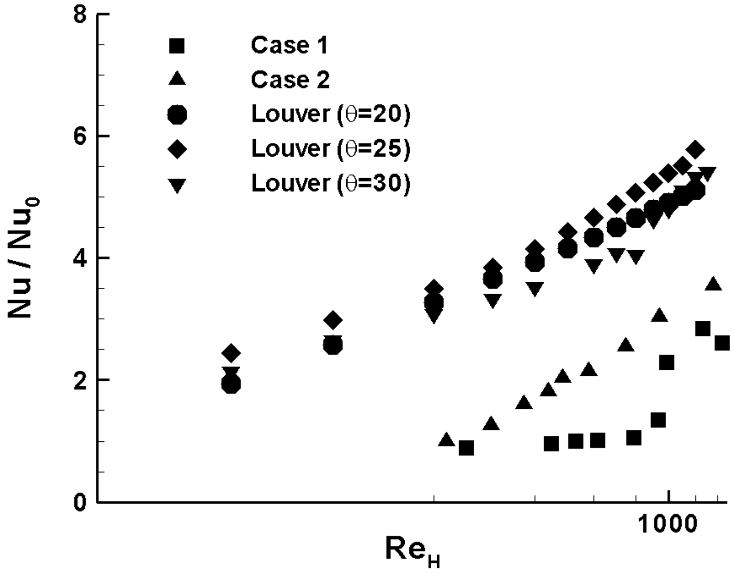

Figure 4.1: Nusselt number augmentation for dimpled channel (Case 1 and Case 2) and typical louvered fin configuration.

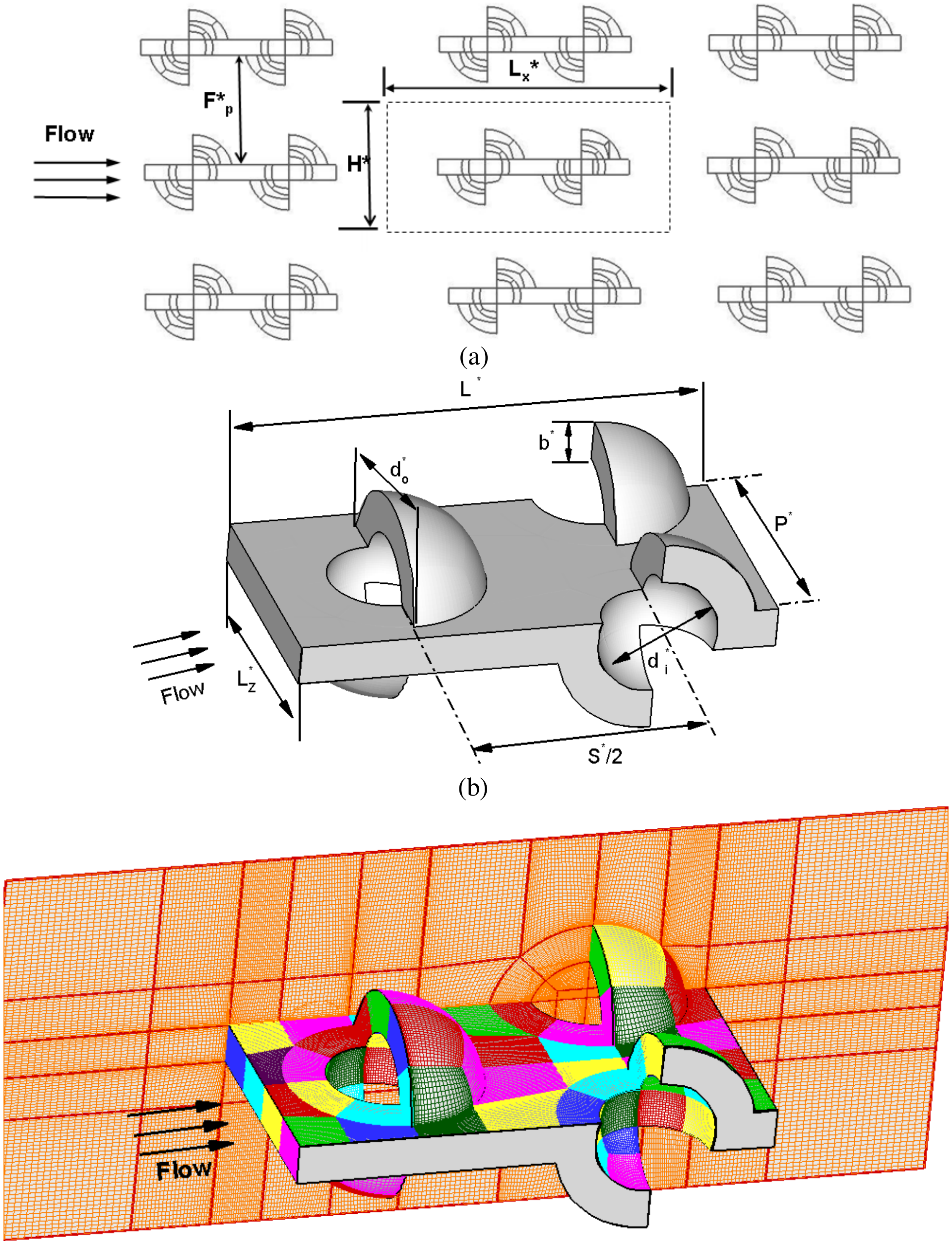

(a)

(b)

(c)

Figure 4.2: Split-dimple fin: a) arrangement; b) geometry; c) domain mesh.

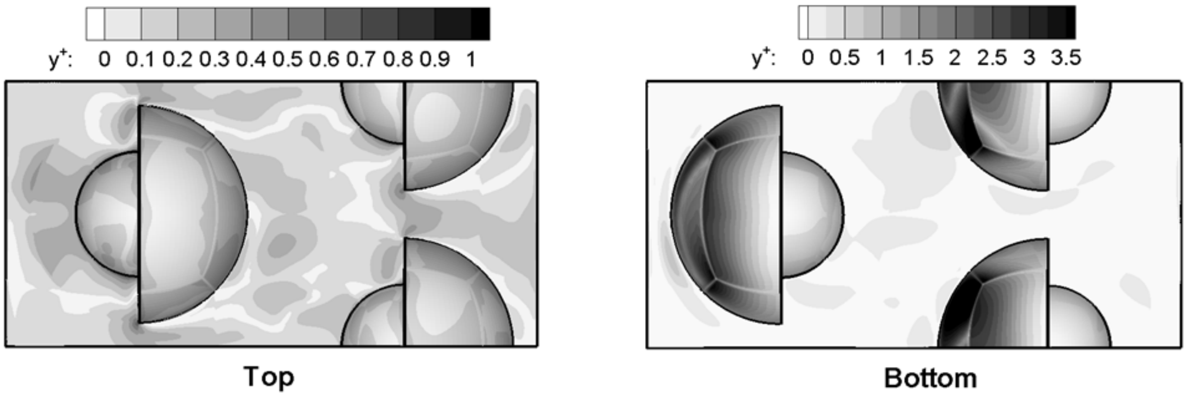

Figure 4.3: y^+ distribution at the top and bottom fin surfaces of the split-dimple fin at Re_H=4000.

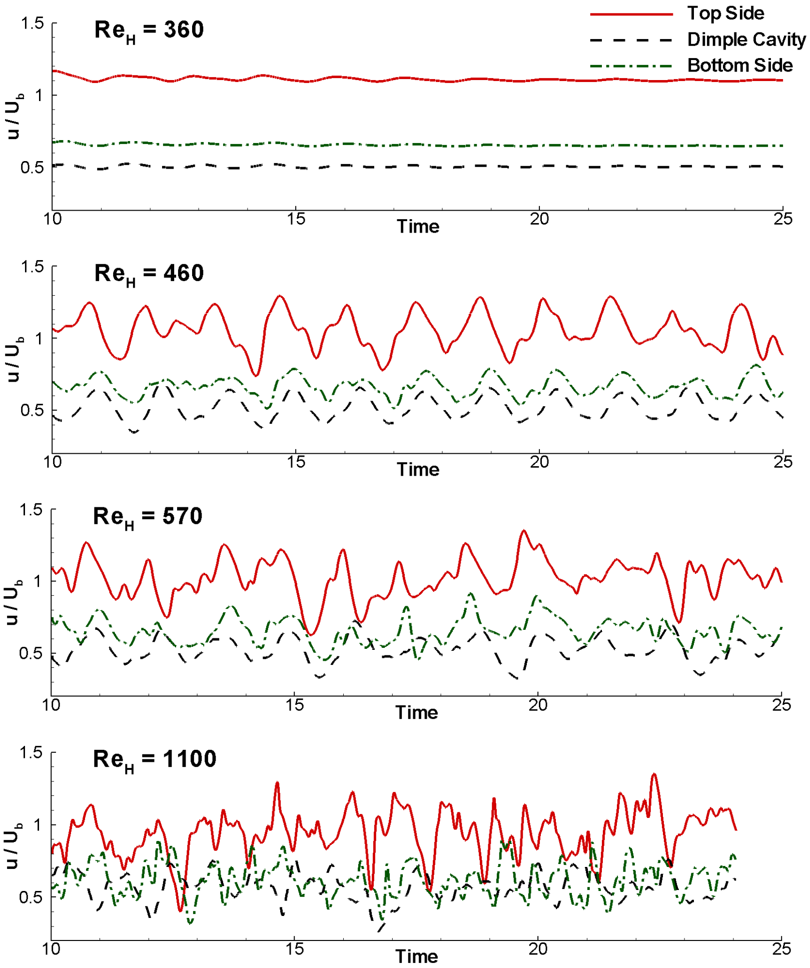

Figure 4.4: Split-dimple's instantaneous streamwise velocity signals normalized with the bulk velocity for Re_H=360, 460, 570 and 1100.

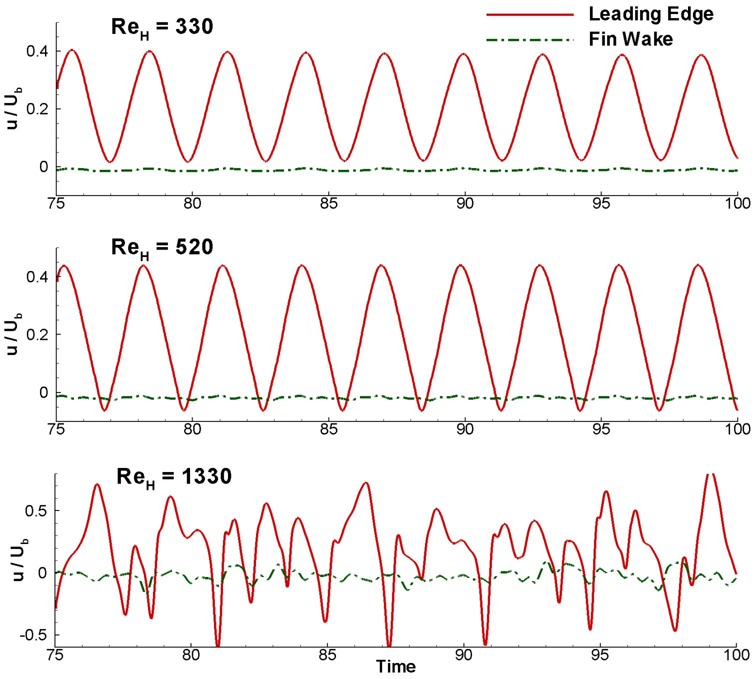

Figure 4.5: Plate fin's instantaneous streamwise velocity signals normalized with bulk velocity for Re_H=330, 520, and 1330.

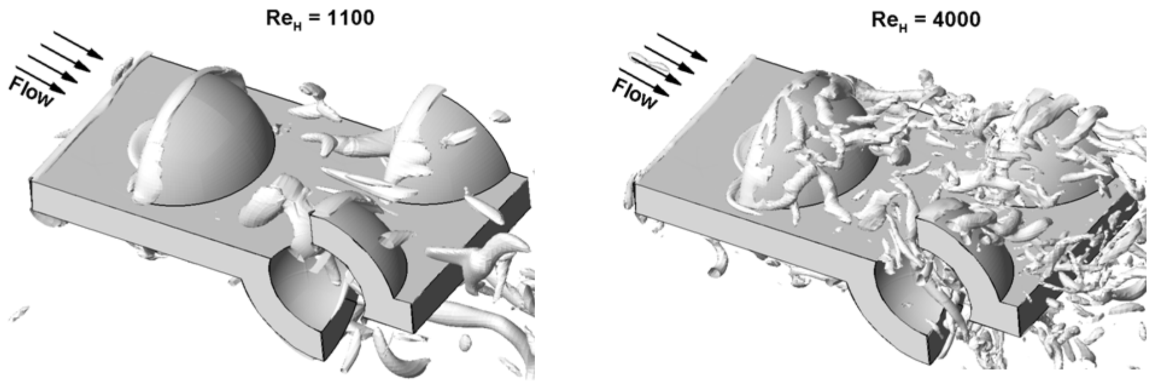

Top

(a)

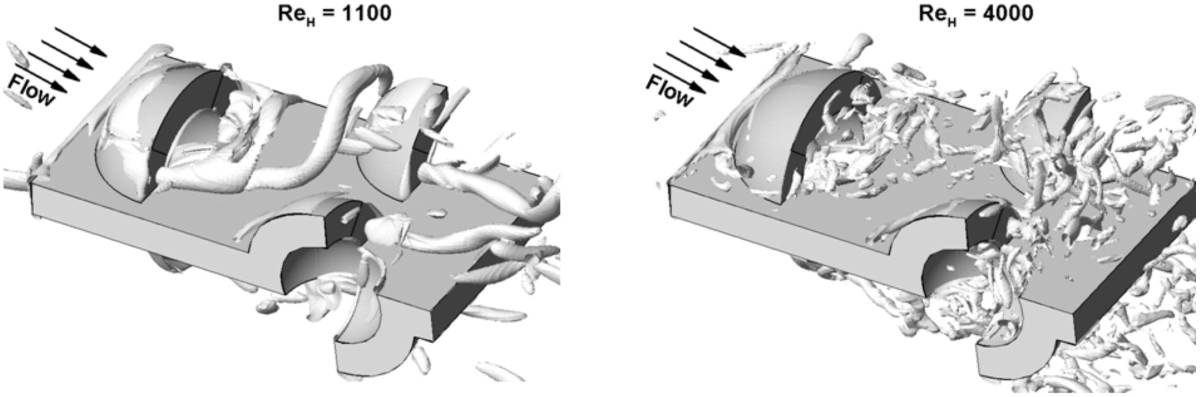

Bottom

(b)

Figure 4.6: Isosurfaces of coherent vorticity for the split-dimple fin for Re$_H$=1100 (left), isosurface level=25, and 4000 (right), isosurface level=50, on the: a) Top side; b) Bottom side.

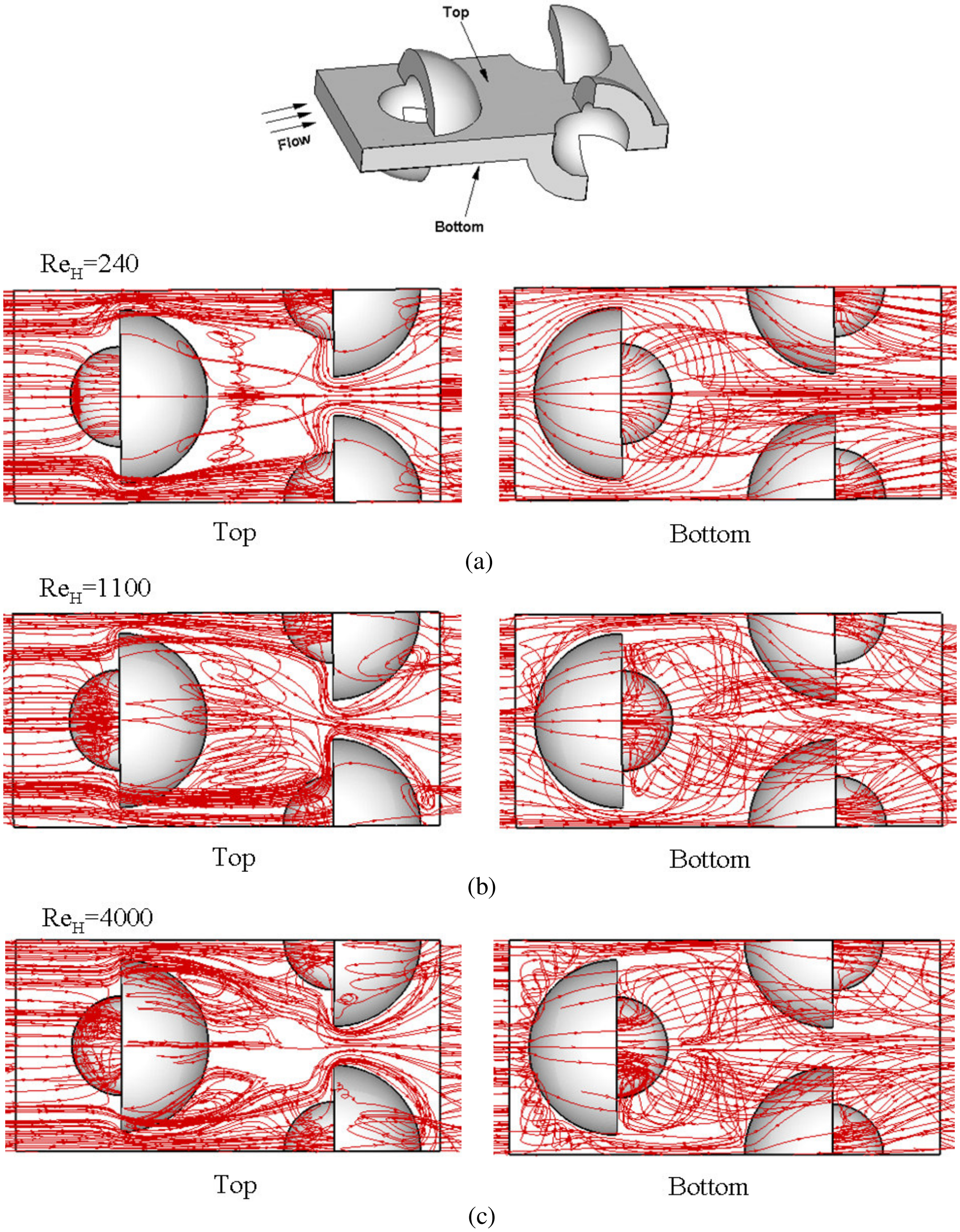

Figure 4.7: Mean velocity stream lines at top (left) and bottom (right) sides of fin at Re_H = a) 240; b) 1100; c) 4000. (Flow from left to right).

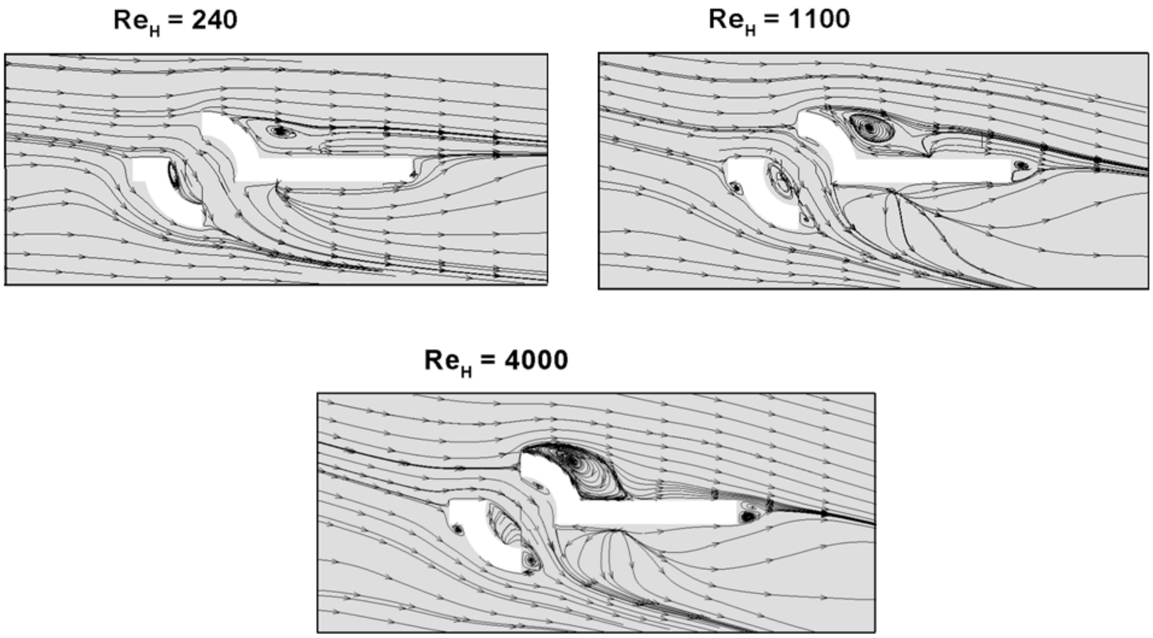

$Re_H = 240$

$Re_H = 1100$

$Re_H = 4000$

Figure 4.8: Mean velocity streamlines at a stream-wise plane crossing the center of the domain (Z=0) for Re_H = 240, 1100, and 4000.

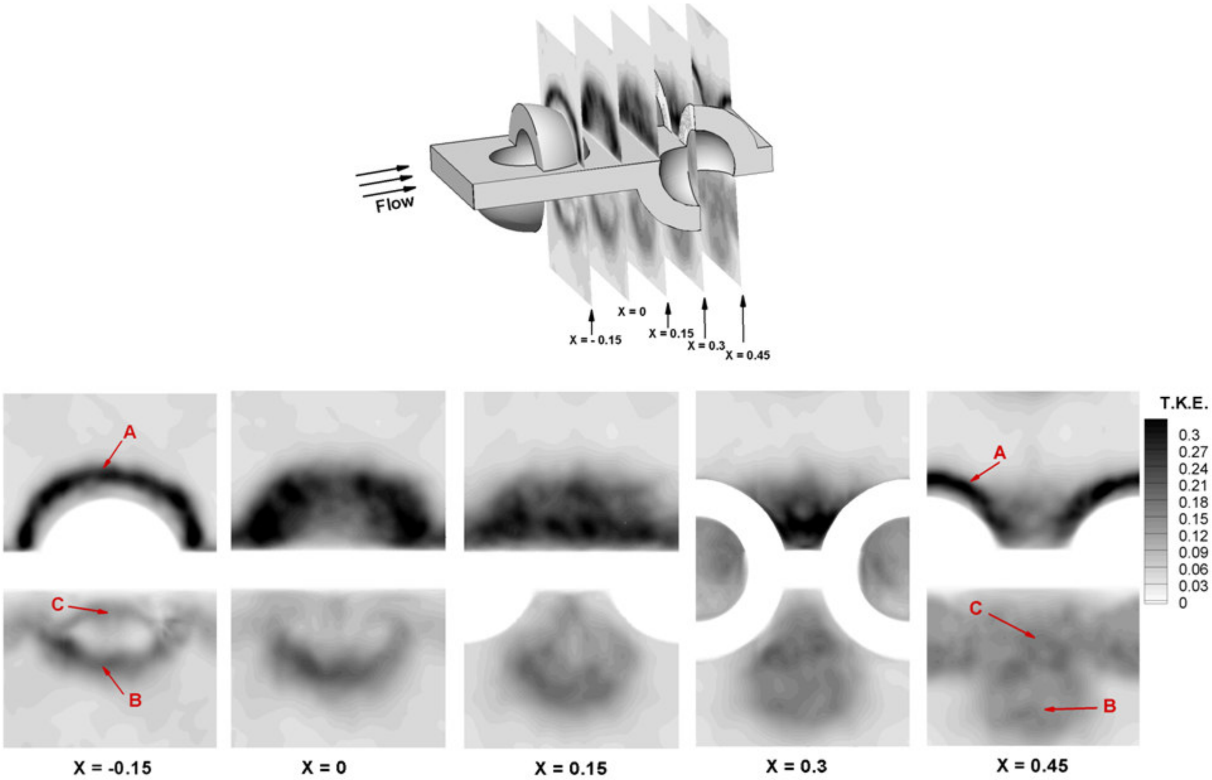

Figure 4.9: Normalized T.K.E. distribution at selected streamwise locations in the split-dimple fin at Re_H=4000.

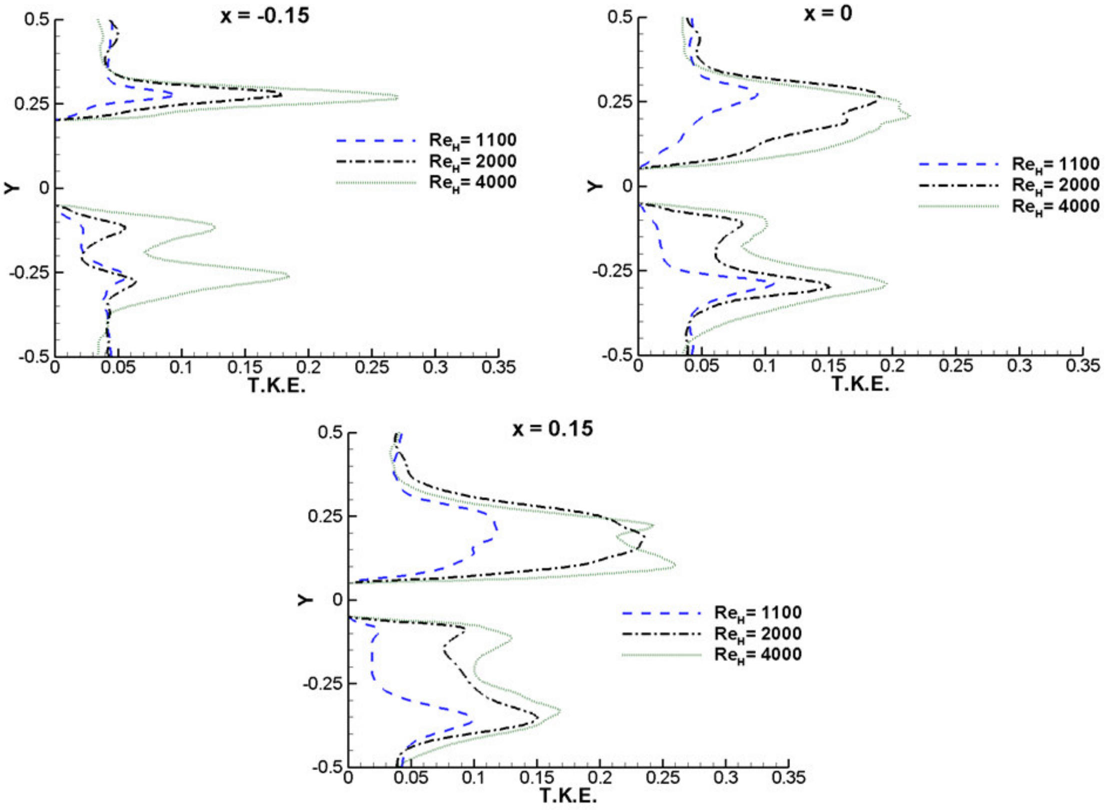

Figure 4.10: Normalized T.K.E. profile for the flow at Re_H=1100, 2000 and 4000 at selected stream-wise locations across the center line of the fin (z=0).

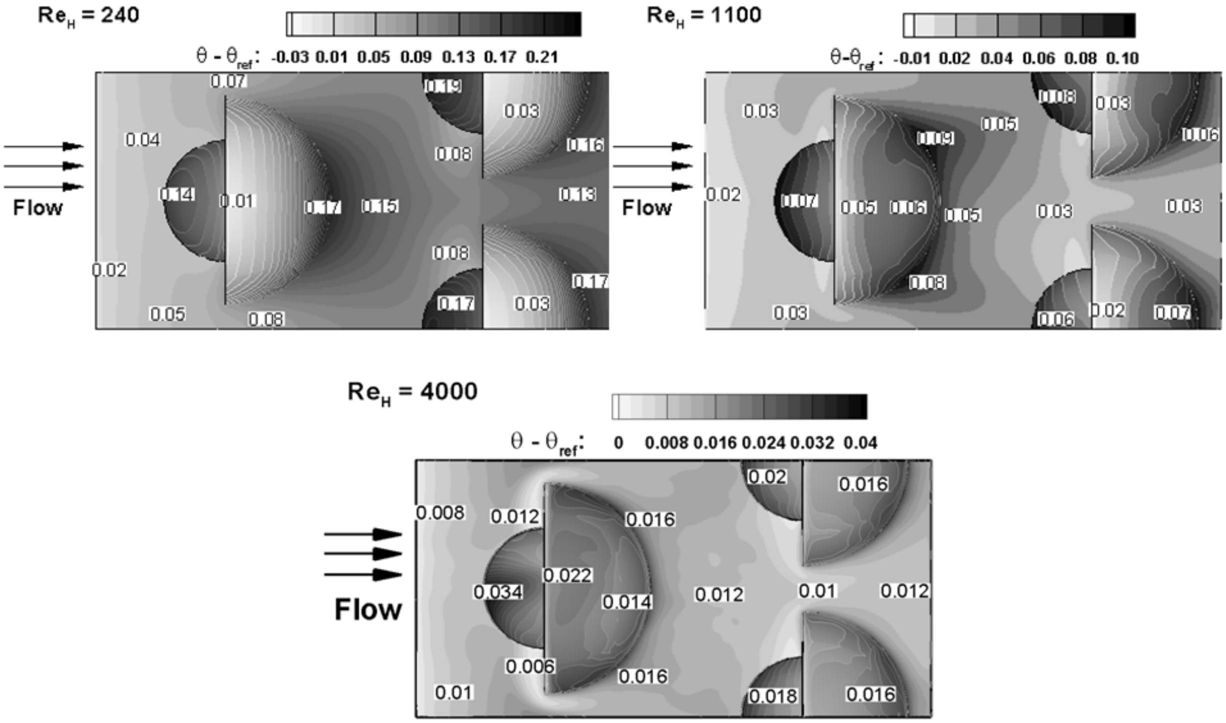

Figure 4.11: Heat transfer distribution at the top fin surface represented by (θ - θ$_{ref}$) for Re$_H$ = 240, 1100, and 4000.

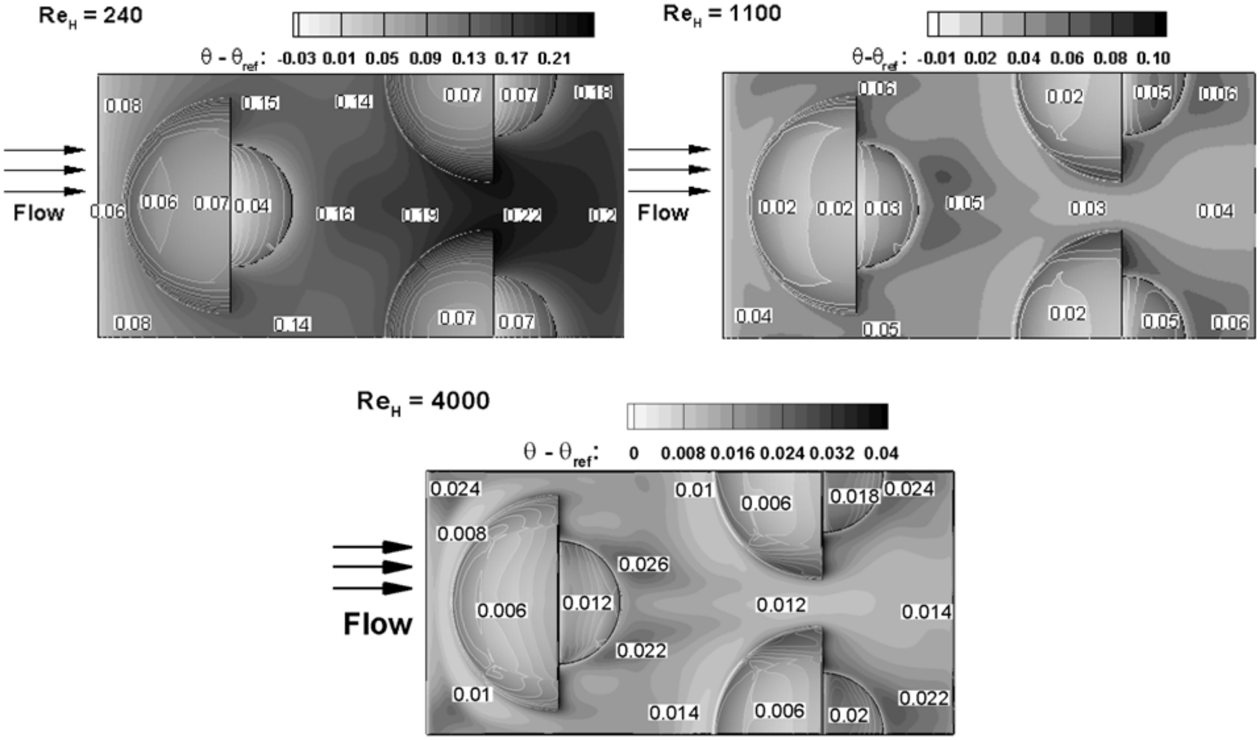

Figure 4.12: Heat transfer distribution at the bottom fin surface represented by (θ - θ$_{ref}$) for Re$_H$ = 240, 1100, and 4000.

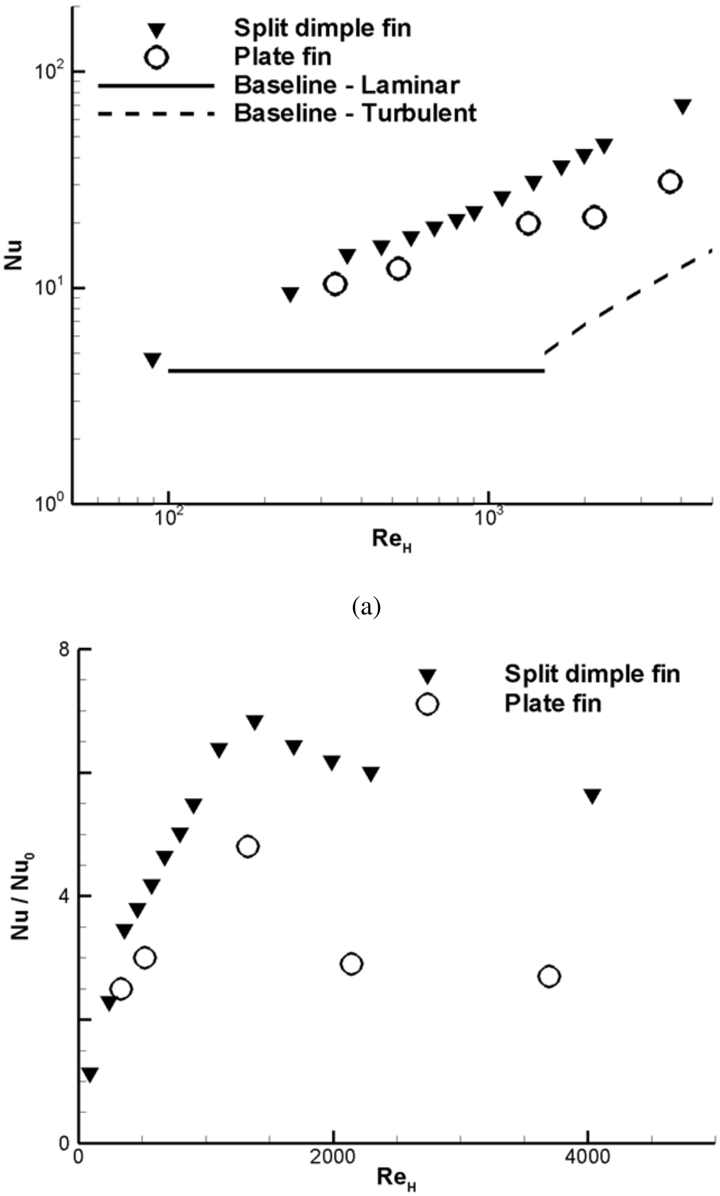

(a)

(b)

Figure 4.13: Comparison of the Nusselt number and Nusselt number ratio for the split-dimple fin and flat plate fin: a) Nu; b) Nu/Nu_0.

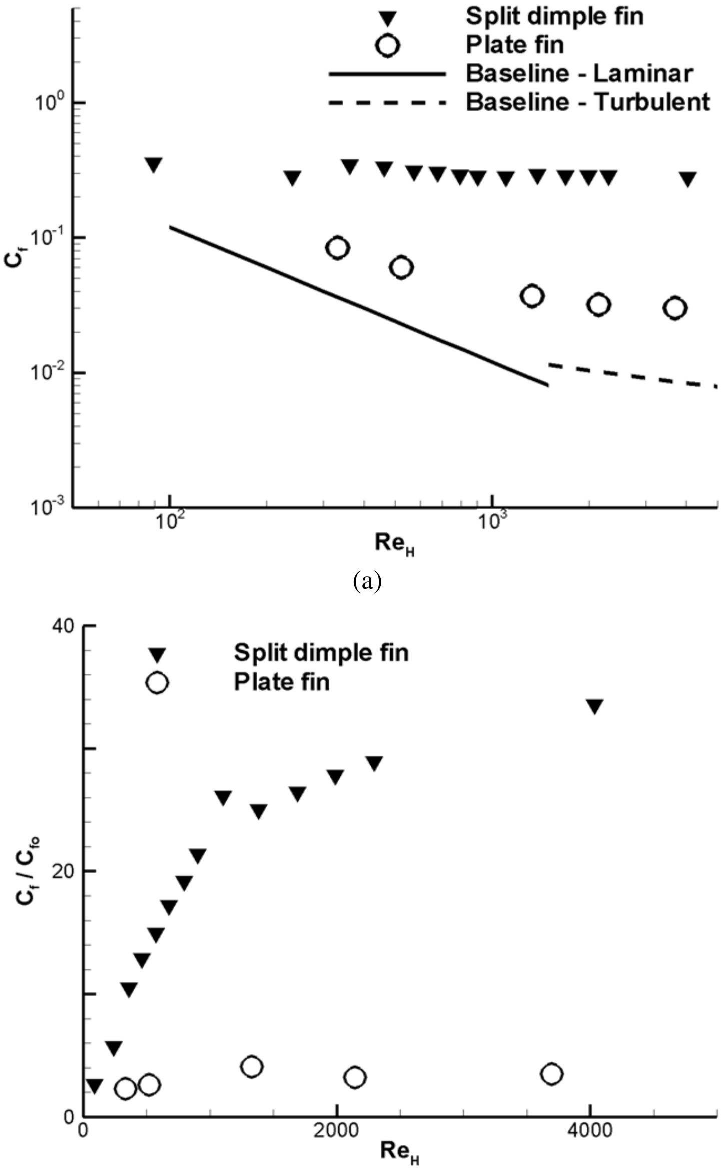

(a)

(b)

Figure 4.14: Comparison of the friction coefficient and friction coefficient ratio for the split-dimple and flat plate fin: a) C_f; b) C_f/C_{fo}.

Chapter 5: Effect of Coriolis forces in a rotating channel with dimples and protrusions

5.1 Abstract

Large-eddy simulations are used to investigate the effect of Coriolis forces and dimple depth on heat transfer and friction in a channel with dimples and protrusions on either side. Two geometries with two different dimple-protrusion depths, δ=0.2 and 0.3 of channel height are investigated over a wide range of rotation numbers, Ro_b = -0.77 to 1.10 based on mean velocity and channel height. It is found that the dimple side of the channel is much more sensitive to destabilizing rotational Coriolis forces than the protrusion side of the channel, although both dimples and protrusions react to the stabilizing effects of Coriolis forces on the leading side. The dimpled surface on the trailing side experiences a large increase in heat transfer coefficient from an augmentation ratio of 1.9 for stationary flow to 3.5 at Ro_b=0.77 for δ=0.2, and from 2.3 to a maximum of 3.8 for δ=0.3. Placing protrusion on the trailing side, however, only increases the augmentation ratio to between 3.25 and 3.7 from the stationary values of 3.0 and 3.4 for δ=0.2 and 0.3, respectively. The dimpled leading side experiences a large drop in heat transfer to between augmentation ratios of 1.1 and 1.4 for the two dimple depths. The protrusion surface on the leading side also experiences a large drop in augmentation from 3.0 for a stationary channel to 1.3 at Ro_b=0.77 for δ=0.2 and from 3.4 to 1.8 at Ro_b=1.1 for δ=0.3. The results lead to the conclusion that for low rotation numbers $|Ro_b|<0.2$, placing protrusions on the trailing side is advantageous, whereas for $|Ro_b|>0.2$, dimples on the trailing side of the duct give better overall performance. Between the two depths, the deeper dimple/protrusion (δ=0.3) gives higher heat transfer augmentation at the price of more frictional losses ranging from 6 to 10 versus 3 to 5 for depth δ=0.2.

5.2 Introduction

Modern gas turbine blades are exposed to increasingly higher gas temperatures which exceed the melting point of the blade material. Thus active cooling plays a critical role in maintaining the structural integrity of the blade. Blades are cooled by extracting bleed air from the compressor and passing it through internal passages inside the airfoil and then ejecting it through holes on to the blade surface to form a protective layer between the hot mainstream gases and the blade surface.

In order to enhance internal cooling, different techniques that increase the heat transfer area and promote turbulence inside the channels are applied. The most common surface enhancements used for heat transfer augmentation of internal cooling are pin fins and ribs, which produce acceptable levels of heat transfer augmentation but the pressure drop penalty can be significant. Friction ratios (C_f/C_{fo}) and Nusselt augmentation (Nu/Nu_o) of 10-20 and 2-5, respectively are common for rib turbulators and pin fins, Ligrani et al. [1].

Flow structure inside rotating channels is quite complex under the action of the turbulence promoters and rotational Coriolis forces. The flow structure and heat transfer distribution inside rotating channels have been thoroughly investigated in the past three decades; where the rotation number, centrifugal buoyancy, and passage geometry were found to be the dominant factors affecting the heat transfer in the channel (Wagner et al. [2] and Wagner et al. [3]). Under the action of rotation, heat transfer from trailing surface increases due to flow destabilization with rotation number, and it decreases at the leading surface due to flow stabilization (Fann et al. [4], Johnson et al. [5], El-Husayni et al. [6], Parson et al. [7], Dutta et al. [8], Griffith et al. [9], Al-Hadhrami et al. [10], Hseih and Chin [11], and Sewall and Tafti [12]). El-Husayni et al. [6] and Parson et al. [7] studied the heating condition effect on the performance of 60^o and 90^o ribbed square ducts, respectively. Moreover, the model orientation was reported to have an impact on the performance of the channel, where the 45^o (or 135^o) orientation of the channel was found to provide better performance of the channel ([6], [7], [8], [9], and [10]).

Murata and Mochizuki [13] and Abdel-Wahab and Tafti [14] studied the effect of Coriolis forces in rotating ribbed duct using LES, where they reported the heat transfer levels to decrease and increase on the leading and trailing sides, respectively. By isolating Coriolis forces from centrifugal buoyancy effects, Abdel-Wahab and Tafti [14] showed that Coriolis forces had a stronger effect on heat transfer from the channel than centrifugal buoyancy. They reported that centrifugal buoyancy yielded an increase of about 10% in the overall augmentation over the Coriolis forces alone, which agrees with the conclusion of Johnson et al. [5] that centrifugal buoyancy does not have a large impact in well mixed flows.

In the present study, new surface geometries based on dimples and protrusions are proposed and investigated for internal blade cooling applications. Heat augmentation using spherical indentations (dimples) has received wide attention lately due to their good heat transfer characteristics and low pressure drop penalty (Afansyev et al. [15]). Several researchers have investigated the effect of different geometry parameters on heat transfer characteristics of the channels, where they reported that the channel height (H/D) and dimple depth (δ/D) have the largest impact on the heat characteristics of dimpled surfaces (Moon et al. [16], Ligrani et al. [17], Mahmood and Ligrani [18], and Won et al. [19]).

The use of dimples/protrusions on opposite sides for heat augmentation in a channel was investigated by Ligrani et al. [20] and Mahmood et al. [21], where they have reported higher friction and Nusselt number than the dimple/dimple case. Elyyan et al. [22] used LES to investigate the flow structure and heat transfer distribution in a stationary channel with dimple-protrusion in the laminar to fully turbulent regime; in addition they also investigated the effect of dimple depth with respect to channel height where they reported a large impact in the low Reynolds number regime.

Despite their good heat transfer characteristics in stationary channels, the work of Griffith et al. [23] is the only experimental study in the literature that has investigated the use of spherical indentations for cooling of rotating turbine blades. They studied the effect of rotation on heat transfer enhancement in a dimpled-dimpled channel with aspect ratio (AR=4) at Reynolds number range Re_{Dh}=5000-40000 and low rotation number range (Ro_b=0.01-0.3), where they have reported a behavior similar to that of a ribbed channel. No detailed flow structure, heat transfer distribution, or pressure drop data was reported.

Elyyan and Tafti [24] used LES to perform a detailed investigation of the Coriolis forces effect on flow structure and heat transfer distribution in a rotating channel with dimples on the trailing side and protrusions on the leading side. They showed the existence of secondary flow structures induced by the Coriolis forces acting on the domain and flow destabilization/stabilization near the trailing/leading surfaces, which lead to about 90% increase of heat transfer near the trailing (dimple) surface and about 50% drop in heat transfer near the leading (protrusion) surface.

In this paper, we extend our analysis of the Coriolis forces effect on a rotating channel with dimples and protrusion to investigate the effect of rotation direction and dimple depth on flow structure, turbulent statistics, and heat transfer distribution on the channel surfaces. Two dimple (protrusion) depths (δ/H=0.2 and 0.3) are considered in the current study. We cover a wide range of rotation numbers from Ro_b= -0.77-1.1, at a nominal Reynolds number of 12,000. The paper describes in detail the mean and turbulent structure of the flow and the subsequent friction and heat transfer characteristic over the full range of rotation numbers.

Nomenclature

D	dimple imprint diameter
C_f	Fanning friction coefficient
g^{ij}	contravariant metric tensor
k	thermal conductivity
H	channel Height
L_x	periodic length
Nu	Nusselt number
P	span-wise pitch
p	fluctuating, modified or homogenized pressure
Pr	Prandtl number
q''	constant heat flux on channel walls
Q_x	mass flow rate in the streamwise direction
Re	Reynolds number ($= u_b H/\nu$)

Ro_b	rotation number ($= \omega_z H / u_b$)
Ro_{Dh}	rotation number based on hydraulic diameter ($= \omega_z D_h / u_b$)
S	stream-wise pitch
$\vec{u}$	cartesian velocity vector
$\vec{x}$	physical coordinates
β	mean pressure gradient
γ	mean temperature gradient
δ	dimple depth
$\vec{\xi}$	computational coordinates
ω_z	rotation speed of the channel around the z-axis
θ	fluctuating, modified or homogenized temperature
Ω	heat transfer surface area

Subscripts

b	bulk
o	smooth channel
t	turbulent parameters
τ	values based on friction velocity

Superscripts

*	dimensional quantity
$^+$	wall units
–	grid filtered quantity
^	test filtered quantity

5.3 Channel Geometry, Computational Domain, and Governing Equations

Figure 5.1 shows the channel geometry used in this study which consists of aligned dimples and protrusions on opposite surfaces. Since dimple depth was found to have a strong impact on the flow structure and heat transfer in stationary channels, we consider two dimple depths: Case 1 with δ=0.2 and Case 2 with δ=0.3. Both geometry cases have a dimple and protrusion stream-wise and span-wise pitch of S=P=1.62, and dimple imprint diameter D=1.0. Note that all channel dimensions are non-dimensionalized by the channel height (H^*).

The computational domain simulates two parallel plates roughened by dimples and protrusions on opposite sides and assumes fully-developed hydrodynamic and thermal flow, Figure 5.1. For stationary ribbed ducts it is known that a nominally fully-developed flow is reached within 3-4 rib pitches from the duct entrance [25]. However, the developing length is much longer in a rotating duct and takes up to 8-9 rib pitches for the Coriolis driven effects to reach a spatially stationary state [26]. Hence the assumption of fully-developed flow and heat transfer may not exactly represent an actual cooling passage in a rotating blade. However, the assumption does not distort the physics of rotational effects and is a valid assumption in evaluating different geometries at different rotation numbers without much loss of generality in extending the conclusions to a developing flow. Using the fully-developed assumption, the channel is assumed to be periodic in the stream-wise and span-wise directions, and rotating at a uniform angular velocity (ω_z^*) orthogonal to an axis aligned with the z-axis. Channel surfaces exposed to the flow, i.e. dimple and protrusion surfaces, are heated with a constant heat flux (q''^*). The channel height (H^*)[1], friction velocity ($u_\tau^* = \sqrt{\tau_{w-eq}^*/\rho^*}$), and a temperature scale given by ($q''^* H^*/k^*$) are used to non-dimensionalize the governing equations of the system as will be shown later.

A special treatment of the pressure and temperature variables is required to accommodate the periodicity boundary condition of the channel [27]. In this treatment, the pressure and temperature variables are decomposed into mean and fluctuating parts as shown in the following non-dimensional equation

$$P^*(\overrightarrow{x^*}, t^*) = P_{in}^* - \beta^* x^* + p^*(\overrightarrow{x^*}, t^*) \qquad (1a)$$

$$T^*(\overrightarrow{x^*}, t^*) = T_{in}^* + \gamma^* x^* + T'^*(\overrightarrow{x^*}, t^*) \qquad (1b)$$

where the mean pressure and temperature gradients, β^* and γ^*, are found by performing momentum and energy balances, respectively. The non-dimensional pressure and temperature gradients are given as

$$\beta = \frac{4}{D_h} \qquad (2)$$

---

[1] The asterisk (*) is used to denote dimensional quantities

$$\gamma = \frac{\Omega}{Re_\tau \Pr Q_x L_x} \tag{3}$$

The non-dimensional[1] continuity, momentum and energy equations in transformed coordinates after incorporating the modified variables take the form

Continuity:

$$\frac{\partial}{\partial \xi_j}\left(\sqrt{g}\,\overline{U}^j\right) = 0 \tag{4}$$

Momentum:

$$\frac{\partial}{\partial t}\left(\sqrt{g}\,\overline{u}_i\right) + \frac{\partial}{\partial \xi_j}\left(\sqrt{g}\,\overline{U}^j\,\overline{u}_i\right) = -\frac{\partial}{\partial \xi_j}\left(\sqrt{g}\left(\vec{a}^j\right)_i \overline{p}\right) + \frac{\partial}{\partial \xi_j}\left(\left(\frac{1}{Re_\tau} + \frac{1}{Re_t}\right)\sqrt{g}\,g^{jk}\,\frac{\partial \overline{u}_i}{\partial \xi_j}\right) + F_I \tag{5}$$

Energy:

$$\frac{\partial}{\partial t}\left(\sqrt{g}\,\overline{\theta}\right) + \frac{\partial}{\partial \xi_j}\left(\sqrt{g}\,\overline{U}^j\,\overline{\theta}\right) = \frac{\partial}{\partial \xi_j}\left(\left(\frac{1}{Pr\ Re_\tau} + \frac{1}{Pr_t\ Re_t}\right)\sqrt{g}\,g^{jk}\,\frac{\partial \overline{\theta}}{\partial \xi_j}\right) - \sqrt{g}\,\gamma\,\overline{u}_1 \tag{6}$$

where $\vec{a}^i$ are the contravariant vectors[2], $\sqrt{g}$ is the Jacobian of transformation, g^{ij} are the elements of the contravariant metric tensor, $\sqrt{g}U^i = \sqrt{g}(\overrightarrow{a^j})_i u_i$ is the contravariant flux vector, $\overline{u_i}$ is the Cartesian velocity vector, Re_τ is the Reynolds number based on the friction velocity (u_τ), and θ is the modified temperature. The overbar denotes grid filtered quantities; where $\bar{G}$ is the implicit top hat filter given by

$$\bar{G}(x_i - x'_i) = \begin{cases} \frac{1}{\overline{\Delta x_i}}; & |x_i - x'_i| \le \overline{\Delta x_i}/2 \\ 0; & otherwise \end{cases} \tag{7}$$

where $\overline{\Delta x_i}$ is the grid spacing. Re_t is the inverse of the non-dimensional turbulent eddy-viscosity

1

---

[1] Henceforth, all usage is in terms of non-dimensional quantities unless qualified with an asterisk.

[2] The notation $\left(\vec{a}^j\right)_k$ is used to denote the k-th component of vector $\vec{a}^j$. $\left(\vec{a}^j\right)_k = \partial\xi_j/\partial x_k$

$$\frac{1}{Re_t} = C_s^2\left(\sqrt{g}\right)^{2/3}|\overline{S}| \tag{8}$$

where $|\overline{S}|$ is the magnitude of the strain rate tensor given by $|\overline{S}| = \sqrt{2\overline{S_{ik}S_{ik}}}$; and the strain rate tensor is given by

$$\overline{S_{ij}} = \frac{1}{2}\left(\frac{\partial \overline{u_i}}{\partial x_j} + \frac{\partial \overline{u_j}}{\partial x_i}\right) \tag{9}$$

and the Smagorinsky constant C_s^2 is calculated using the Dynamic subgrid stress model [28]. To calculate this constant, a second filter, test filter, denoted by $\hat{G}$, is applied to the filtered governing equations with the characteristic length of $\hat{G}$ being larger than that of the grid filtered, $\overline{G}$. The test filtered quantity is obtained from the grid filtered quantity by a second-order trapezoidal filter which is given by $\widehat{\overline{\emptyset}} = \frac{1}{4}(\overline{\emptyset}_{i-1}+2\overline{\emptyset}_i+\overline{\emptyset}_{i+1})$ in computational coordinates in one dimension. The resolved turbulent stresses, representing the energy scales between the test and the grid filters, $L_{ij} = \widehat{\overline{u_i}\overline{u_j}} - \widehat{\overline{u}}_i\widehat{\overline{u}}_j$, are then related to the subtest, $T_{ij} = \widehat{\overline{u_i u_j}} - \widehat{\overline{u}}_i\widehat{\overline{u}}_j$, and subgrid-scale stresses $\tau_{ij} = \overline{u_i u_j} - \overline{u}_i\overline{u}_j$, through the identity $L_{ij} = T_{ij} - \hat{\tau}_{ij}$.

The anisotropic subgrid and the subtest-scale stresses are then formulated in terms of the Smagorinsky eddy viscosity model as

$$\hat{\tau}_{ij} = -2C_s^2\left(\sqrt{g}\right)^{2/3}\widehat{|\overline{S}|\overline{S}_{ij}} \tag{10}$$

$$T_{ij}^a = -2C_s^2 \propto \left(\sqrt{g}\right)^{\frac{2}{3}}|\widehat{\overline{S}}|\widehat{\overline{S}}_{ij} \tag{11}$$

Using the identity

$$L_{ij}^a = L_{ij} - \tfrac{1}{3}\delta_{ij}L_{kk} = -2C_s^2 \propto \left(\sqrt{g}\right)^{\frac{2}{3}}\left(|\widehat{\overline{S}}|\widehat{\overline{S}}_{ij} - \widehat{|\overline{S}|\overline{S}_{ij}}\right)$$

$$= -2C_s^2 \propto \left(\sqrt{g}\right)^{\frac{2}{3}}M_{ij} \tag{12}$$

Here α is the square of the ratio of the characteristic length scale associated with the test filter to that of the grid filter and is taken to be $\propto = \left[\frac{\hat{\overline{\Delta}}_i}{\overline{\Delta}_i}\right]^2 = 6$ for a three dimensional test filtering operation (Najjar and Tafti [29]). Using the least-square minimization procedure presented by Lilly [30], the dynamic Smagorinsky constant can be calculated as:

$$C_s^2 = -\frac{1}{2}\left(1/(\sqrt{g})^{\frac{2}{3}}\right)\left(\frac{L_{ij}^a.M_{ij}}{M_{ij}.M_{ij}}\right) \tag{13}$$

Where the local value of C_s^2 is constrained to positive values. The turbulent Prandtl number is assumed to have a constant value of 0.5 [31] in equation(6).

The Coriolis forces and mean pressure gradients effect (β) are included in the momentum equation through an external force term, F_i:

$$F_i = \sqrt{g}\beta\delta_{i1} - 2\sqrt{g}(Ro_\tau)\overline{u_m}\epsilon_{i3m} \tag{14}$$

Note that the mean centrifugal buoyancy term is implicitly absorbed into the mean pressure term in the x-momentum equation. No slip and constant heat flux boundary condition are imposed at the domain walls

$$\vec{u} = 0 \tag{15a}$$

$$\nabla\theta.\vec{\mathrm{n}} = 1 - \gamma\vec{e}_x.\vec{\mathrm{n}} \tag{15b}$$

and periodic boundary conditions are applied at the stream-wise and span-wise edges of the domain

$$\emptyset(\mathrm{x_i} + \mathrm{L_i}) = \emptyset(\mathrm{x_i}),\ \emptyset = \vec{\mathrm{u}}, \mathrm{p}, \text{and } \theta, \text{and i} == 1 \text{ and } 3. \tag{15c}$$

5.4 Numerical Method

The non-dimensional generalized Navier-Stokes and energy equations are solved on a non-staggered grid topology, where the pressure, temperature and Cartesian velocities are solved and stored at the cell centers and the fluxes are calculated at the cell faces. Conservative finite-volume formulation with a second-order accurate central difference scheme is used to discretize the governing equations. A predictor-corrector scheme is used for time advancement of the solution, where an intermediate velocity is calculated at the predictor step which is then corrected by satisfying discrete continuity at the corrector step. Advancement in time for the energy equation is performed using the predictor step.

Simulations are performed using the computer program GenIDLEST (Generalized Incompressible Direct and Large Eddy Simulation of Turbulence). GenIDLEST has been used to study flow structure and heat transfer in compact heat exchangers [32] and in stationary and rotating ribbed ducts ([25] and [33],) and has been validated extensively with experimental results. Details about the computer program and its capabilities can be found in Tafti [34].

5.5 Calculation of Nusselt Number and Friction Coefficient

Pressure drop and heat transfer of the channel are evaluated by using the friction coefficient, C_f, and Nusselt number, Nu, of the domain. The friction coefficient and Nusselt number are calculated as (the asterisk indicates dimensional quantities)

$$C_f = \frac{\tau_{weqv}^*}{\frac{1}{2}\rho^* U_b^{*2}} = \frac{\beta D_h}{2U_b^2} \tag{16}$$

$$Nu = \frac{q''^* H^*}{k_f^*\left(T^* - T_{ref}^*\right)} = \frac{1}{\left(\theta - \theta_{ref}\right)} \tag{17}$$

where θ_{ref} is the mean-mixed temperature of the flow defined as

$$\theta_{ref} = \frac{\iiint |u_x| \theta \, dA_x dx}{\iiint |u_x| dA_x dx} \tag{18}$$

The surface-averaged Nusselt number at the two channel walls is calculated by integrating over the surface (S)

$$Nu_{avg} = \frac{\iint dS}{\iint (\theta - \theta_{ref}) dS} \tag{19}$$

and the overall average Nusselt number of the channel is calculated by taking the mean of the leading and trailing surface Nusselt numbers.

Nusselt number and friction coefficient of a smooth channel are used as to evaluate the augmentation ratios of Nusselt number and friction coefficient. Those are obtained using the Petukhov and Gielinski correlations for C_f and Nu [35], respectively:

$$C_{f_o} = (1.580 \ln(Re_H) - 2.185)^{-2} \; ; 1500 \leq \mathrm{Re_H} \leq 2.5 \times 10^6 \tag{20}$$

$$Nu_o = \frac{(C_{f_o}/2)(Re_H - 500)Pr}{1 + 12.7 (C_{f_o}/2)^{\frac{1}{2}} (Pr^{2/3} - 1)}^{-2} \; ; 1500 \leq \mathrm{Re_H} \leq 2.5 \times 10^6 \tag{21}$$

Note that the original Petukhov and Gnielinski correlations are rewritten here in terms of Re_H rather than Re_{Dh}, where $Re_{Dh} = 2Re_H$ for smooth parallel plates.

5.6 Domain and Grid Independency Studies

A domain independency study is conducted to obtain the smallest spatial unit capable of capturing the relevant flow structures which impact friction and heat transfer predictions. Elyyan *et al.* [22] conducted a domain independency study for a stationary channel that is identical to Case 1 (δ=0.2) of the current study, where we have considered three domain sizes: domain 1 which is the minimum available spatial unit with domain size (1×P/2×S), domain 2 (1×P×S) which is twice domain 1 in the span-wise direction, and domain 3 (1×P/2×2S) which is twice domain 1 in the stream-wise direction, Figure 5.2. The study showed that the maximum difference in the friction ratio (C_f/C_{fo}) and Nusselt number augmentation (Nu/Nu_o) from that of Case 1 was 3.5% and 5.55%, respectively, which proved the sufficiency of domain 1 (1×P/2×S) for capturing the relevant flow modes.

To further investigate the sufficiency of domain 1 for capturing the additional flow complexity induced by Coriolis forces (rotating channel), we have conducted an additional domain independency study for the same domains considered earlier, domain 1, 2, and 3, at a nominal rotation number, Ro_b=0.64, and a nominal Reynolds number, Re_H=11,000. The domain independency test results summarized in Table 5.1 further confirm the sufficiency of Domain 1 (1×P/2×S) in capturing the relevant flow structures in the domain, where the time mean Nusselt number and friction coefficient of Domain 2 are 1.9% and 3.2% different from those of Domain 1, and those of Domain 3 have differences of 2.7% and 1.4% from those of Domain 1.

Once a computational domain size was selected (Domain 1), we have performed a grid independency study using four mesh resolutions: Mesh 1 is the coarsest grid with 466,944 cells, Mesh 2 is finer than Mesh 1 in the cross-stream direction with total no. of cells of 933,888, Mesh 3 is three times finer than Mesh 1 in the cross-stream direction with 1,400,832 cells, and Mesh 4 is three times Mesh 1 in the cross-stream direction and twice as fine in the wall parallel directions with a total of 5,603,328 cells. All cases are constructed using 28 grid blocks with finer mesh resolution placed in the vicinity of solid surfaces of the channel. Calculations are performed at a nominal Reynolds number, Re_H=11,000, and rotation number, Ro_b=0.64. Table 5.2 summarizes the results of the grid independency test, where the finest mesh case (Mesh 4) is taken as a reference for comparison. While the error on the coarsest mesh is 9% and 6% in time mean Nusselt number and friction coefficient, these reduce to 3% and 1% on Mesh 3. Due to the relatively small gain in accuracy but at a much larger cost between Mesh 3 and 4, Mesh 3 is selected for performing the calculations in the current study with a domain size 1×P/2×S.

Figure 5.3 shows the surface mesh distribution at the wall and in the cross-stream direction. Fine grid resolution is placed in the cross-stream direction in the vicinity of the solid walls of the channel with the first grid point placed at an average distance of $\Delta y = 4.0\times10^{-4}$ from the walls. An *a-posteriori* calculation of the friction velocity showed the grid to be fine enough with the first grid point at $y^+_1 < 0.5$ at the dimples and protrusion surfaces and 5-6 grid points located within $y^+ = 10$.

5.7 Results and Discussion

Table 5.3 and Table 5.4 summarize the calculations conducted for Case 1 (δ=0.2) and Case 2 (δ=0.3). The friction Reynolds number Re_τ is held constant (Re_τ=2000 for δ=0.2 and Re_τ=3000 for δ =0.3), whereas the rotation number Ro_τ is varied from –4.5 to +4.5. Based on the balance between friction losses and the applied mean pressure gradient β, a bulk mean flow velocity is obtained from the calculation. The calculated mean velocity is then used to define Re_H and Ro_b for each calculation, which range between $10000 \le Re_H \le 14000$ and $-0.80 \le Ro_b \le 1.10$. During positive or counter-clockwise (CCW) rotation, the dimpled surface of the channel is on the trailing side, whereas during clockwise (CW) rotation, the protrusion side is on the trailing side of the duct. To maintain uniformity in the interpretation of data, all results are non-dimensionalized by the calculated mean bulk velocity in the channel (u_b). Nusselt numbers and friction coefficients are normalized by the baseline values given by equation (11) and (12) at their respective Re_H. While the absolute values of friction coefficient and Nusselt numbers are sensitive to the Reynolds number, the augmentation ratios have negligible sensitivity to the Reynolds number variations in the range between $10000 \le Re_H \le 14000$.

Each calculation is initiated with an initial best guess of velocity and temperature fields and allowed to develop under the influence of the prescribed pressure gradient. When the flow shows a statistically stationary state, temporal averaging is conducted for a typical sampling time between 5 to 10 non-dimensional time units.

5.7.1 Mean flow structure

The relationship between flow structure and surface heat transfer in a stationary channel with dimples and protrusions has been investigated in detail by Elyyan et al. [22]. It was established that heat augmentation on the dimpled surface was chiefly brought about by separation induced vortex impingement in the reattachment region of the dimple cavity. The ejection and redirection of these vortices and additional vortex shedding at the rim of the dimple was responsible for the high heat transfer augmentation on the flat landing downstream of the dimple. On the other hand, on the protrusion side, flow impingement on protrusions and acceleration between protrusions played an important role in augmenting heat transfer. Wake turbulence also playing a role in augmenting heat transfer on the flat landing downstream of the protrusion.

Coriolis forces modify momentum transfer by adding force terms into the momentum equations. For orthogonal rotation about the z-axis, additional terms $2\mathrm{Ro_b v}$ and $-2\mathrm{Ro_b u}$ act as additional force terms in x- and y-momentum transfer, respectively. For positive or CCW rotation, the first-order effect is an additional net downward force in the y-momentum equation which tends to push the fluid towards the trailing wall of the channel increasing the flow rate in the bottom half. This first-order effect gives rise to secondary flow cells within the channel cross-section. The secondary flow increases in magnitude with rotation number and at high rotation numbers is found to counter the first-order effect of Coriolis forces by transporting fluid from the trailing to the leading side of the duct. An additional effect is the impact of Coriolis forces on turbulence production. Although Coriolis forces do not make a direct contribution to the production of turbulent kinetic energy, they do affect its magnitude indirectly through their action on normal stress components and the primary shear stress $\overline{\mathrm{u'v'}}$. In turbulent channel flow, through phenomenological reasoning it can be shown that on the trailing side of the channel, terms attributed to Coriolis forces reinforce third quadrant ($\overline{\mathrm{u'v'}} < 0$) turbulence generation mechanisms of bursts and sweeps while having an opposite effect on the leading side. These are often referred to as the “destabilizing” and “stabilizing” effects of Coriolis forces. Whereas the phenomenological effects of Coriolis forces do not change from one geometry to another, its non-linear interactions with the base stationary flow and resulting impact on heat transfer augmentation through flow field modification is different from one geometry to another.

The effect of rotation on the mean flow is characterized in Figure 5.4, Figure 5.5 and Figure 5.6. Figure 5.4 shows the velocity streamlines at a stream-wise plane along the dimple/protrusion centerline at z=-0.81 (see Figure 5.3) for the stationary and rotating cases for Case 1 with dimple depth, δ=0.2. Figure 5.5 and Figure 5.6 plot the friction lines (or streamlines very close to the surface) on the dimple and protrusion sides of the channel, respectively to give an additional perspective on the mean flow. In a stationary duct, flow approaching the protrusion impinges and accelerates around it producing high wall shear at the sides and at the end wall between protrusions (Elyyan et al.[22]). The shear layer on the protrusion separates as it encounters an adverse pressure gradient to form a turbulent wake region behind the protrusion, which reattaches on the flat landing downstream of the protrusion. A small mean recirculating eddy is also present at the windward junction of the protrusion with the channel wall. Flow on the dimple side of the channel is characterized by turbulent shear layer separation at the windward (leading) rim of the dimple with reattachment in the dimple cavity. As the flow from the dimple cavity is ejected out along the leeward (trailing) rim of the dimple, it separates once again and reattaches on the flat landing.

The action of Corilois forces has the following mean effect on the flow field:

- As the channel is rotated in the counter-clockwise (CCW) direction, the dimpled side is oriented as the trailing edge with the protrusions on the leading side of the channel. The action of Coriolis forces leads to a more energetic flow on the trailing side of the channel which results in the progressive shrinking of the recirculation zone in the dimple cavity as the turbulent separated shear layer reattaches faster. The structure of the recirculation region in the dimple cavity changes from covering most of the lateral radius of the dimple to an elongated structure mostly concentrated in the center of the dimple cavity. Further, by early and more energetic reattachment in the dimple cavity, the flow ejection at the leeward rim of the dimple cavity is strengthened. Conversely, on the protrusion side of the channel, Coriolis forces make the flow less energetic resulting in a gradual growth of the wake region as the rotation number increases. Close inspection of Figure 5.4 and Figure 5.5 reveals that there is an increase in the extent of the wake region up to CCW2 (Ro_b=0.39) after which the wake shrinks in size.

- For clockwise (CW) rotation, the flow shifts towards the protrusion side of the channel which acts as the trailing edge. The action of Coriolis forces is not as strongly evident on the flow structure as it is at the dimpled surface for counter-clockwise rotation (CCW). There is some effect on the extent of the protrusion wake which shrinks in size initially (Ro_b=-0.35, CW2 in Figure 5.6), but which does not change significantly as rotation increases to Ro_b=-0.70 (CW4 in Figure 5.6). An additional visible modification to the flow field is the disappearance of the junction eddy in front of the protrusion. On the leading dimpled surface, the effects of rotation are much more evident. The attenuation of turbulence leads to a less energetic flow which results in delayed reattachment of the separated shear layer in the dimple cavity and the recirculation zone extends across the whole dimple at Ro_b=-0.70 (CW4 in Figure 5.4). There is also a noticeable weakening of the flow ejection out of the dimple cavity (CW2 and CW4 in Figure 5.5) indicated by the absence of separation and reattachment around the leeward rim of the dimple. Rotation also changes the structure of the recirculating region in the dimple cavity. As the rotation number increases, two counter-rotating vortex structures become prominent inside the cavity (CW2 and CW4 in Figure 5.5) and the structure of the flow in the dimple cavity approaches that observed in stationary flows at lower Reynolds numbers (Ligrani et al. [17] and Elyyan et al. [22]).

In order to indentify the secondary flow structures induced by the Coriolis forces, mean cross-sectional streamlines 0.2D downstream of the dimple/protrusion are examined in Figure 5.7. For counter-clockwise (CCW) rotation, two counter-rotating flow structures appear in the span-wise plane, one over the dimple and the other above the flat landing downstream of the dimple. The smaller structure at the rim of the dimple is a manifestation of the early flow reattachment in the cavity and the more energetic flow ejection at the rim of the dimple which imparts a rotational component to the shear layer. Whereas the larger structures which are present above the dimple and the flat landing extend from the trailing wall to midway through the channel can be attributed to Coriolis induced secondary flow. These secondary flow structures gain definition and magnitude with increasing rotation number. To provide better definition to the secondary flow structures, Figure 5.8 shows selected planes covering the dimple-to-dimple stream-wise pitch at CCW4 (Ro_b=0.77), which shows well-defined secondary flow cells in the cross-section over the full stream-wise pitch. It is noted that the flow cells are clearly biased towards the dimple side of the channel. On the other hand, observing Figure 5.7 for clockwise rotation (CW) rotation shows no major change in the flow structure in the channel cross-section. Examination of different stream-wise planes at CW4 reveals differences with similar planes in the stationary channel, but does not reveal any differentiating organized secondary flow cells which can be clearly attributed solely to rotational effects.

Whereas streamlines give a structural view of the cross-stream flow, to obtain some quantitative measure of the secondary flow and its effect on the bulk flow, Figure 5.9 shows the stream-wise (u) and cross-stream (v) velocities normalized by the bulk velocity for the CCW and CW cases at the centerline just downstream of the dimple and protrusion. It is observed that at low rotation numbers $|Ro_b|<0.2$, the first-order effect of Coriolis forces to push the bulk flow towards the trailing wall is evident for both CCW (dimple side) and CW (protrusion side). However, in both cases (CCW and CW) as the rotation number increases above 0.2, the trend in the u-velocity profiles is reversed as the bulk flow shifts towards the leading side of the channel. This is attributed to the stronger Coriolis induced secondary flows set-up in the cross-section – as can be deduced from the cross-stream velocities in Figure 5.9(b), which increase with rotation number.

5.7.2 Turbulent Kinetic Energy

Turbulent Kinetic Energy (TKE) levels are of special interest, since they are closely connected to the rate of heat transfer from surfaces. Figure 5.10 shows the TKE distribution, normalized by the bulk velocity squared, at a span-wise plane 0.2D downstream of the dimple/protrusion at different rotation numbers. For the stationary channel, high TKE levels exist in the separated shear layer inside the dimple cavity (labeled A), the turbulent wake region downstream of the protrusion (labeled B), and region C, which is the carry-over of wake turbulence from the upstream protrusion. With rotation in the positive or counter-clockwise direction (CCW), the TKE contours show: i) concentrated high TKE levels in the separated shear layer inside the dimple cavity (labeled A); ii) diminishing TKE levels in the wake of the protrusion (labeled B) and in region C due to the slower flow movement near the leading (protrusion) surface; iii) higher TKE levels in the flow ejection zone at the lateral rim of the dimple cavity, which coincides with the location of the secondary flow structure identified in Figure 5.7 and Figure 5.8 at the same location. Note that the high TKE levels in region A that represent the separated shear layer inside the dimple cavity move closer to the dimple surface as the rotation number increases (CCW1-CCW4), which corroborates with the early reattachment observed in Figure 5.4. Moreover, the TKE levels for CCW3 (Ro_b=0.64) and CCW4 (Ro_b=0.77) are lower than those at the lower rotation numbers. This is due to the action of the Coriolis induced secondary structures which drives the flow away from the dimple surface and corroborates with the observation made for the stream-wise velocity profile for the CCW cases, in Figure 5.9.

With the protrusion on the trailing side (CW cases), the TKE contours show: i) lower TKE levels that diminish with increasing rotation number in the separated shear layer inside the dimple cavity (region A); ii) a smaller concentrated TKE zone in the wake of the protrusion (B) and a magnification of region (C); and iii) attenuation of TKE inside the dimple cavity. Note that, similar to the CCW cases, the TKE levels become weaker as the rotation number increases to Ro_b=-0.58 (CW3) and -0.77 (CW4) especially in the wake of the protrusion. This observation corroborates with the mean velocity profiles in Figure 5.9, which indicate that as rotation number increases, flow is pushed away from the trailing towards the leading side of the channel.

Figure 5.11 shows the TKE profiles at the centerline of the dimple (z=0) at a plane 0.2D downstream of the dimple/protrusion (x=-0.2) for the CCW and CW cases. Two main peaks appear in the TKE profile. Near the dimple wall, the peak in TKE is representative of the turbulent characteristics of flow ejecting out of the dimple cavity which after separation at the rim of the dimple, reattaches in this region, and the peak at the protrusion side representing the turbulent wake of the protrusion. As the channel rotates in the CW direction (protrusion on trailing side), the maximum value of TKE increases in the wake of the protrusion at Ro_b=-0.15 (CW1), but starts decreasing thereafter on further increase in the rotation number. The leading side of the channel (dimples) experience a monotonic decrease in the peak value near the surface as the flow stabilizes. For counter-clockwise (CCW) rotation the opposite effects come into play. There is a steady decrease in TKE in the turbulent wake of the protrusion, while on the dimple side, the peak TKE increases initially for CCW1 but then decreases as the rotation number increases further.

Figure 5.12 shows the volume averaged TKE values for the two dimple/protrusion depths of 0.2 and 0.3. Since the heat transfer rate is strongly dependent on the TKE, volume-averaged TKE provides a concise indicator of heat transfer behavior. As we would expect, the deeper dimple depth geometry (δ=0.3) results in higher TKE values than the shallower dimple depth (δ=0.2). What is quite revealing though, are the predicted trends of TKE. For CCW rotation when dimples are on the trailing wall, the TKE increases up to about Ro_b=0.6 for δ=0.3 and Ro_b=0.5 for δ=0.2, after which it decreases as rotation number increases further. On the other hand, for CW rotation the volume averaged TKE decreases with rotation number. This trend implies that CCW rotation is much more successful in augmenting turbulence on the dimpled surface (trailing side) than it is on the protrusion side of the channel during CW rotation. It will be shown later that the averaged heat transfer coefficients closely mimic the trends in volume-averaged TKE.

5.7.3 Heat Transfer Distribution

Figure 5.13 and Figure 5.14 show contours of the time averaged Nusselt number augmentation ratio on the protrusion surface for CCW and CW rotation, respectively. In the stationary channel, regions of high heat transfer exist on the windward side of the protrusion due to flow impingement and acceleration and on the flat wall in the passage between protrusions. Low heat transfer regions exist near the location of separation and in the wake region. The presence of the junction eddy at the windward edge of the protrusion also decreases the heat transfer (Figure 5.4). With CCW rotation there is a gradual decrease in the heat transfer distribution as the flow slows down and stabilizes near the leading-protrusion surface (Figure 5.13). The region of maximum heat transfer on the protrusions moves from the side of the protrusion to the center and decreases in magnitude as Ro_b increases. Similar decreases are observed on the wall in the passages between protrusions and in the wake of the protrusion.

With clockwise rotation when the protrusion surface is on the trailing side more pronounced heat augmentation is observed on the front of the protrusion (stronger flow impingement and acceleration), in the passage between protrusions and at flow reattachment downstream of the protrusion (Figure 5.14). Note that these zones of high heat transfer shrink in size for the highest rotation, which is in agreement with the TKE countours and profiles seen earlier in Figure 5.10 and Figure 5.11. Moreover, the low heat transfer region at flow separation at the back of the protrusion become smaller as the rotation number increases, which is due to the smaller wake and earlier flow reattachment discussed in Figure 5.4.

Figure 5.15 and Figure 5.16 show contours of the time averaged Nusselt number ratio on the dimple surface for the CCW (trailing) and CW (leading) rotation, respectively. In the stationary channel, high heat transfer regions are mostly observed in the dimple cavity in the region of shear layer reattachment and acceleration of the flow as it ejects out of the dimple cavity at the leeward rim. This is followed by a region of low heat transfer immediately downstream of the rim periphery which is caused by shear layer separation of the ejected flow followed by a region of high heat transfer when the shear layer reattaches back on the flat landing and is consistent with observations made in Figure 5.5. The region of flow recirculation in the upstream half of the dimple incurs the largest heat transfer penalty. On CCW rotation, the most visible effect is the higher heat transfer in the dimple cavity as the recirculation zone shrinks in size as seen earlier in Figure 5.4. A counter-effect is the increase in the low-heat transfer region surrounding the leeward rim of the dimple as the rotation number increases, which is consistent with the observation of reducing TKE near the surface on the flat landing in Figure 5.10and Figure 5.11. When the dimples are placed on the leading side in CW rotation (Figure 5.16), there is a steady decrease in heat transfer augmentation ratio as the rotation number increases. The attenuation in heat transfer is evident over the whole leading surface especially in the dimple as the recirculation region grows to cover the full extent of the dimple cavity (Figure 5.4 and Figure 5.5).

5.7.4 Average Friction Coefficient and Nusselt Number

Figure 5.17 shows the surface averaged Nusselt number variation with Ro_b for the two dimple-protrusion depths considered, i.e. $\delta=0.2$ and 0.3, on the leading and trailing surfaces. The general trends for $\delta=0.3$ follow that of $\delta=0.2$ with some differences which will be highlighted. When the dimple surface is on the trailing side for CCW rotation, there is a sharp increase in the average Nusselt number as the channel starts rotating at $Ro_b<0.2$ when the augmentation ratio increases from 1.8 to 2.96 for $\delta=0.2$ and from 2.3 to 2.9 for $\delta=0.3$. After this point, on a further increase in rotation number to $Ro_b=0.39$, the shallower dimples with $\delta=0.2$ increase to 3.4 and increase gradually thereafter to values in the range of 3.5 at $Ro_b=0.64$ and 0.77. On the other hand, the deeper dimples exhibit a sharp increase in the augmentation ratio to 3.8 as the rotation number increases from $Ro_b=0.19$ to 0.57, and decreases thereafter to values close to 3.65 as the rotation number Ro_b increases further to 0.9 and 1.1. When the dimple surface is on the leading side of the channel (CW rotation), there is a steady drop in the average augmentation ratio for both dimple depths. The augmentation ratio decreases from the stationary values of 1.8 and 2.3 to 1.1 and 1.4, for $\delta=0.2$ and 0.3, respectively at the highest rotation number tested.

When the protrusion surface is on the trailing side during CW rotation, one of the main differences when compared to dimples on the trailing side during CCW rotation is the fact that the heat transfer augmentation does not react as strongly to rotation. At low rotation numbers $Ro_b<-0.2$, the augmentation ratio increases slightly from 3.0 to 3.25 and 3.4 to 3.67 for $\delta=0.2$ and 0.3, respectively. On further increase in rotation number, the heat transfer augmentation increases slightly or remains nearly constant. This is in contrast to when dimples are placed on the trailing surface resulting in a large increase in the augmentation ratio with rotation. However, protrusions on the leading side during CCW rotation behave similar to dimples and experience a large decrease in heat transfer. At low rotation numbers $Ro_b<0.2$, there is a sharp drop in augmentation ratio from the stationary value of 3.0 to 2.3 for δ=0.2, and from 3.43 to 2.43 for δ=0.3. The initial sharp drop is followed by a more gradual monotonic decrease to 1.3 at Ro_b=-0.77 and to 1.8 at Ro_b=1.1 for δ=0.2 and 0.3, respectively.

In summary, in the stationary channel, the augmentation ratio is higher on the protrusion side than the dimple side of the channel. During CCW rotation, the dimpled surface on the trailing side experiences a large increase in heat transfer coefficient whereas the protrusion surface on the leading side experiences a large drop in augmentation. During CW rotation, while the dimpled leading side experiences a large drop in heat transfer, the trailing protrusion side does not benefit much from rotation.

Figure 5.18 shows the average heat transfer augmentation and friction ratio for the two dimple-protrusion depths over the full range of rotation numbers. When protrusions are placed on the trailing side of the channel as during CW rotation, there is a monotonic decrease in the overall Nusselt number augmentation as rotation number increases. However, when dimples are placed on the trailing side as in CCW rotation, the augmentation ratio behaves differently at δ=0.2 and 0.3. For the shallower depth, there is a drop in augmentation ratio with rotation, but the drop is not as steep as when protrusions are at the trailing side and for a given rotation number it would be more advantageous to have a dimpled surface on the trailing side. For the deeper depth of δ=0.3, the trend is no longer monotonic. There is a drop in augmentation ratio at Ro_b=0.19, after which the ratio increases sharply to values above the stationary channel at Ro_b=0.59, and then drops gradually as the rotation number increases further. Hence for the deeper depth, placing the protrusion on the trailing side gives larger overall augmentation at low rotation numbers Ro_b<0.2, whereas for Ro_b> 0.2, dimples on the trailing side would be more advantageous. In summary, for δ=0.2, the overall augmentation ratio ranges between 2.2 and 2.65, whereas for δ=0.3, it ranges from 2.5 to 3.05 over the range of rotation numbers studied. Lastly, it is noted that the trends in overall heat transfer augmentation correlate with the trends in volume-averaged TKE reinforcing the relationship between the turbulent characteristics of the flow and heat transfer augmentation.

Friction ratios range from 8.5 to 10 when dimples are placed on the trailing side versus 6.2 to 8.5 when protrusions are placed on the trailing side for δ=0.3. The increase in friction is much lower for δ=0.2, with values ranging from 3.5 to 5.7 and from 4.2 to 5.7, when protrusions or dimples are on the trailing side, respectively.

To put the current results in perspective, Figure 5.19 shows a comparison of the heat augmentation levels of the dimple/protrusion geometry with the experimental results of El-Husayni et al [6] for 60° staggered ribs, Parson et al. [7] for 90° ribs, Griffith et al. [9] for 45° ribs, and Griffith et al. [23] for dimpled channel plotted against the rotation numbers based on the hydraulic diameter (D_h). These comparisons are not under similar conditions, Table 5.5, but nevertheless give a reasonable assessment of the dimple-protrusion geometry with respect to some of its peers in the literature. Heat augmentation levels on the leading surface, Figure 5.19(a), are lower than those of the skewed ribs (45° and 60°) but are comparable to those of normal ribs and dimpled channel, especially with the dimple on the leading side. On the other hand, the heat augmentation levels on the trailing side, Figure 5.19(b), are comparable to those of ribbed channels, especially for the deeper dimple depth (δ=0.3). While no friction data is provided in the experimental studies, overall it can be concluded that surfaces with dimple/protrusion roughness result in performance comparable to ribbed channels at a lower pressure drop penalty.

5.8 Summary and conclusions

Large-eddy simulations are used to investigate the effect of Coriolis forces and dimple depth on heat transfer and friction in a channel with dimples and protrusions on either side. Two geometries with two different dimple depths, δ=0.2 and 0.3 are investigated for a wide range of rotation numbers, Ro_b = -0.77 to 1.10. During negative or clockwise (CW) rotation, protrusions are on the trailing side of the channel, whereas during positive or counter-clockwise (CCW) rotation, dimples are on the trailing side of the duct.

Rotational Coriolis forces have the following effects on the mean flow and turbulence:

- CCW rotation energizes the flow on the trailing dimple wall and induces early reattachment in the dimple cavity increasing the strength of the flow ejection out of the dimple cavity. On the protrusion side, the less energetic flow results in a gradual growth of the wake region as the rotation number increases. In addition, a secondary flow consisting of two counter-rotating flow structures appear in the cross-section, one over the dimple and the other above the flat landing downstream of the dimple. The secondary flow strengthens as the rotation number increases and plays in important role in transporting cross-stream momentum from the trailing to the leading side. CCW rotation increases the volume averaged TKE values in the domain up to a rotation number of approximately 0.5 to 0.6, after which it decreases.

- The effect of CW rotation on the trailing protrusion surface is not very strong. There is some effect on the protrusion wake which shrinks in size initially but which does not change significantly as rotation increases further. On the leading dimpled surface, the less energetic flow results in delayed reattachment of the separated shear layer with the recirculation zone extending across the whole dimple. No distinct secondary flow structures could be identified in this case and unlike CCW rotation, the volume averaged TKE decreases with rotation number.

The effects on heat transfer are summarized as follows:

During CCW rotation, the dimpled surface on the trailing side experiences a large increase in heat transfer coefficient from an augmentation ratio of 1.9 for stationary flow to 3.5 at Ro_b=0.77 for δ=0.2, and from 2.3 to a maximum of 3.8 for δ=0.3. The protrusion surface on the leading side also experiences a large drop in augmentation from 3.0 for a stationary channel to 1.3 at Ro_b=0.77 for δ=0.2 and from 3.4 to 1.8 at Ro_b=1.1 for δ=0.3. During CW rotation, the dimpled leading side experiences a large drop in heat transfer to between augmentation ratios of 1.1 and 1.4 for the two dimple depths, the trailing protrusion side does not benefit much from rotation - only increasing the augmentation ratio to between 3.25 and 3.7 from the stationary values of 3.0 and 3.4 for δ=0.2 and 0.3, respectively. These results lead to the conclusion that for low rotation numbers $|Ro_b|<0.2$, placing protrusions on the trailing side is advantageous, whereas for $Ro_b>0.2$, dimples on the trailing side of the duct will give better overall performance. Between the two dimple depths, the deeper dimple gives higher heat transfer augmentation at the price of more frictional losses ranging from 6 to 10 for δ=0.3 versus 3 to 5 for δ=0.2.

5.9 Acknowledgments

The calculations were performed on Virginia Tech's Terascale computing facility, System-X. The allocation grant and support provided by the staff is gratefully acknowledged.

5.10 References

[1] Ligrani, P.M., Oliveira, M.M., Blaskovich, T., "Comparison of heat transfer augmentation techniques." AIAA journal, vol. 41, no. 3, pp. 337-362, 2003.

[2] Wagner, J.H., Johnson, B.V., Hajek, T.J., "Heat transfer in rotating passages with smooth walls and radial outward flow." J. Turbomachinery, vol. 113, pp. 42-51, 1991.

[3] Wagner, J.H., Johnson, B.V., Kopper, F.C., "Heat transfer in rotating serpentine passages with smooth walls." J. Turbomachinery, vol. 113, pp. 321-330, 1991.

[4] Fann, S., Yang, W.J., Zhang, N., "Local heat transfer in a rotating serpentine passage with rib-roughened surfaces." Int. J. Heat Mass Transfer, vol. 37, no. 2, pp. 217-228, 1994

[5] Johnson, B.V., Wagner, J.H., Steuber, G.D., Yeh, F.C., "Heat transfer in rotating serpentine passages with trips skewed to the flow." J. Turbomachinery, vol. 116, pp. 113-123, 1994.

[6] El-Husayni, H.A., Taslim, M.E., Kercher, D.M., "Experimental heat transfer investigation of stationary and orthogonally rotating asymmetric and symmetric heated and turbulated channels." J. Turbomachinery, vol. 116, pp. 124-132, 1994.

[7] Parson, J.A., Han, J.C., Zhang, Y.M., "Effects of model orientation and wall heating condition on local heat transfer in a rotating two-pass square channel with rib turbulators." Int. J. Heat Mass Transfer, vol. 38, no. 7, pp. 1151-1159, 1995.

[8] Dutta,S., Han, J.C., "Local heat transfer in rotating smooth and ribbed two-pass square channels with three channel orientations." J. Heat Transfer, vol. 118, pp. 578-584, 1996.

[9] Griffith, T.S., Al-Hadhrami, L., Han, J.C., "Heat transfer in rotating rectangular channels (AR=4) with angled ribs." J. Turbomachinery, vol. 124, pp. 617-625, 2002.

[10] Al-Hadhrami, L., Han, J.C., "Effect of rotation on heat transfer in tow-pass square channels with five different orientations of 45^{o} angled rib turbulators." Int. J. Heat Mass Transfer, vol. 46, pp. 653-669, 2003.

[11] Hseih, S.S., Chin, H.J., "Turbulent flow in a rotating two pass ribbed rectangular channel." J. Turbomachinery, vol. 125, pp. 609-622, 2003

[12] Sewall, E.A., Tafti, D.K., "Large eddy simulation of flow and heat transfer in the developing flow region of a rotating gas turbine blade internal cooling duct with Coriolis and buoyancy Forces." J. Turbomachinery, vol. 130, no. 1, p. 011005, 2008.

[13] Murata, A., Mochizuki, S., "Effect of cross-sectional aspect ratio on turbulent heat transfer in an orthogonally rotating rectangular smooth duct." Int. J. Heat Mass Transfer, vol. 42, pp. 3803-3814, 1999.

[14] Abdel-Wahab, S. and Tafti, D. K., "Large eddy simulations of flow and heat transfer in a 90º ribbed duct with rotation - effect of Coriolis and centrifugal buoyancy forces." J. Turbomachinery 126(4), pp. 627-636, 2004.

[15] Afanasyev, N.V., Chudnovsky, Ya.P., Leontiev, A.I., Roganov, P.S., "Turbulent flow friction and heat transfer characteristics for spherical cavities on a flat plate." Experimental thermal and fluid science, vol. 7, pp. 1-8, 1993.

[16] Moon, H.K., O'Connel, T., Glezer, B., "Channel height effect on heat transfer and friction in a dimpled passage." J. Turbomachinery, vol. 122, pp. 307-313, April 2000.

[17] Ligrani, P.M., Harrison, J.L., Mahmood, G.I., Hill, M.L., "Flow structure due to dimple depressions on a channel surface." Physics of fluids, vol. 13, no. 11, pp. 3442-3451, 2001.

[18] Mahmood, G.I., Ligrani, P.M., "Heat transfer in a dimpled channel: combined influences of aspect ratio, temperature ratio, Reynolds number, and flow structure." Int. J. heat mass transfer, vol. 45, pp. 2011-2020, 2002.

[19] Won, S.Y., Zhang, Q., Ligrani, P.M., "Comparisons of flow structure above dimpled surfaces with different dimple depths in a channel." Physics of Fluids, vol. 17, no. 4, p. 045105, April 2005.

[20] Ligrani, P.M., Mahmood, G.I., Harrison, J.L., Clayton, C.M., Nelson, D.L., "Flow structure and local Nusselt number variation in a channel with dimples and protrusions on opposite walls." Int. J. Heat Mass Transfer, vol. 44, pp 4413-4425, 2001.

[21] Mahmood, G.I., Sabbagh, M.Z., Ligrani, P.M., "Heat transfer in a channel with dimples and protrusions on opposite walls." J. Thermophysics and Heat Transfer, vol. 15, no. 3, pp. 275-283, 2001.

[22] Elyyan, M.A., Rozati, A., Tafti, D.K., "Investigation of dimpled fins for heat transfer enhancement in compact heat exchangers." Int. J. Heat Mass Transfer, vol. 51, pp. 2950-2966, 2008.

[23] Griffith, T.S., Al-Hadrami, L., Han, J.C, "Heat transfer in rotating rectangular cooling channels (AR=4) with dimples." J. Turbomachinery, vol. 125, no. 3, pp. 555-563, July 2003.

[24] Elyyan, M.A., Tafti, D.K., "Effect of Coriolis forces in a rotating channel with dimples and protrusions." Proceedings of ASME-IMECE2008, paper no. IMECE2008-66677.

[25] Sewall, E.A., Tafti, D.K., Graham, A.B., Thole, K.A., "Experimental validation of large eddy simulations of flow and heat transfer in a stationary ribbed duct." Int. J. Heat and Fluid Flow, vol. 27, no. 2, pp. 243-258, 2006.

[26] Sewall, E.A., "Large eddy simulations of flow and heat transfer in the seveloping and 180 bend regions of ribbed gas turbine blade internal cooling ducts with rotation- effect of Coriolis and centrifugal buoyancy forces." PhD dissertation, Virginia Tech, 2005.

[27] Patankar, S.V., Liu, C.H., and Sparrow, E.M., "Fully developed flow and heat transfer in ducts having streamwise-periodic variations of cross-sectional area." J. Heat Transfer, vol. 99, pp. 180-186, 1977.

[28] Germano, M., Piomelli, U., Moin, P., and Cabot, W.H., "A dynamic subgrid-scale eddy viscosity model." Phys. Fluids, vol. 3, pp. 1760-1765, 1991.

[29] Najjar, F.M., Tafti, D.K., "Study of discrete test filters and finite difference approximations for the dynamic subgrid-scale stress models." Phys. Fluids, vol. 8, pp. 1076-1088, 1996.

[30] Lilly, D.K., "A proposed modification of the Germano subgrid-scale eddy viscosity model." Phys. Fluids A, vol. 4, no. 3, pp. 633-635, 1992.

[31] Moin, P. Squires, K., Cabot, W., Lee, S., "A dynamic sub-grid-scale model for compressible turbulence and scalar transport." Phys. Fluids A, vol. 3, no. 11, pp. 2746- 2757, 1991.

[32] J., Cui, D.K.,Tafti, D. K., "Computations of flow and heat transfer in a three-dimensional multilouvered fin geometry." Int. J. Heat Mass Transfer, vol. 45, pp. 5007-5023, 2002

[33] Viswanathan, A. K. and Tafti, D.K., "Detached eddy simulation of turbulent flow and heat transfer in ribbed duct." J. Fluids Engineering, vol. 127, pp. 888-896 Sep. 2005.

[34] Tafti, D.K., "GenIDLEST – A scalable parallel computational tool for simulating complex turbulent flows." Proc. ASME Fluids Engineering Division, FED – Vol. 256, ASME-IMECE, New York, 2001.

[35] Incropera, F.P., DeWitt, D.P., "Fundamentals of heat and mass transfer." 5th Edition, John Wiley, NY, 2002.

Table 5.1: Domain independency study for rotating channel case.

Domain Case	**1**	**2**	**3**
Domain Size	1×P/2×S	1×P×S	1×P/2×2S
# of cells	1,400,800	2,802,00	2,802,00
$\boldsymbol{Re_H}$	10,900	11,100	11,000
$\boldsymbol{Ro_b}$	0.641	0.636	0.636
$\boldsymbol{Nu_{leading}}$	39.8	40.6	40.9
$\boldsymbol{Nu_{trailing}}$	96.3	95.6	94.8
%Max. Diff.	***Ref.***	*1.9*	*2.7*
$\boldsymbol{C_f}$	0.03058	0.02961	0.03014
%Diff.	***Ref.***	*3.2*	*1.4*

Table 5.2: Grid independency results for a dimpled channel at Re_H=11,000 rotating at Rob=0.64.

Mesh	**1**	**2**	**3**	**4**
# of cells	466,944	933,888	1,400,832	5,603,328
Re_H	11,346	11,069	10,926	10,980
Ro_b	0.62	0.63	0.64	0.64
$Nu_{leading}$	39.5	40.3	39.8	38.6
$Nu_{trailing}$	102.5	98.1	96.3	93.7
%Max. Diff.	*9.4*	*4.7*	*3.0*	***Ref.***
C_f	0.02836	0.02979	0.03058	0.03027
%Diff.	*6.3*	*1.6*	*1.0*	***Ref.***

Table 5.3: Rotating channel cases conducted for Case 1 (δ=0.2)

Case	***CW4***	***CW3***	***CW2***	***CW1***	***Stat***	***CCW1***	***CCW2***	***CCW3***	***CCW4***
Ro_b	-0.70	-0.58	-0.35	-0.14	0.0	0.15	0.39	0.64	0.77
Ro_τ	-4.5	-3.5	-2.0	-0.75	0.0	0.75	2.0	3.5	4.5
Re_H	12,900	12,100	11,300	9,700	9,850	10,200	10,200	10,900	11,700
Re_τ	2,000	2,000	2,000	2,000	2,000	2,000	2,000	2,000	2,000

Table 5.4: Rotating channel cases conducted for Case 2 (δ=0.3)

Case	***CW3***	***CW2***	***CW1***	***Stat***	***CCW1***	***CCW2***	***CCW3***	***CCW4***	***CCW5***
$\boldsymbol{Ro_b}$	-0.75	-0.47	-0.19	0.0	0.20	0.34	0.57	0.89	1.10
$\boldsymbol{Ro_\tau}$	-3.5	-2.0	-0.75	0.0	0.75	1.25	2.0	3.5	4.5
$\boldsymbol{Re_H}$	14,000	12,890	12,090	11,590	11,500	11,100	10,590	11,790	12,370
$\boldsymbol{Re_\tau}$	3,000	3,000	3,000	3,000	3,000	3,000	3,000	3,000	3,000

Table 5.5: Experimental heat transfer in rib and dimple roughened channels.

Experimental work	**Surface condition**	**Ro**	**Re**	**Δρ/ρ**
El-Husayni et al (1994) [6]	Square channel with 60^o staggered ribs	0-1.78	5000-23000	
Parson et al (1995) [7]	Square channel with 90^o ribs	0-0.35	2,500-25,000	0.07-0.1
Griffith et al (2002) [9]	Rectangular channel (AR=4) with 45^o ribs	0-0.3	5,000-40,000	0.122
Griffith et al (2003) [23]	Rectangular channel (AR=4) with dimples	0-0.3	5,000-4,0000	0.122

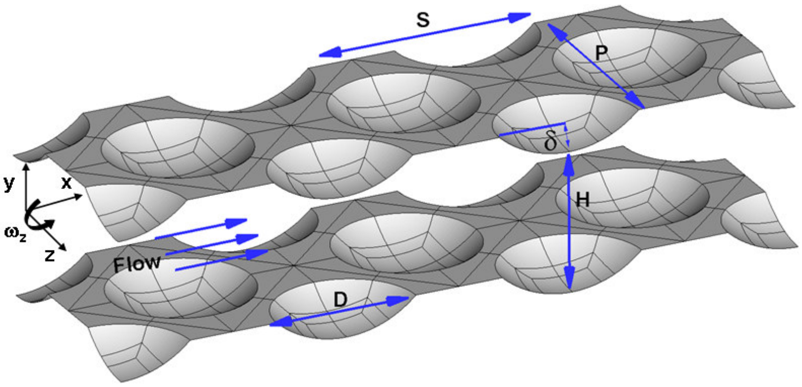

Figure 5.1: Dimpled channel geometry

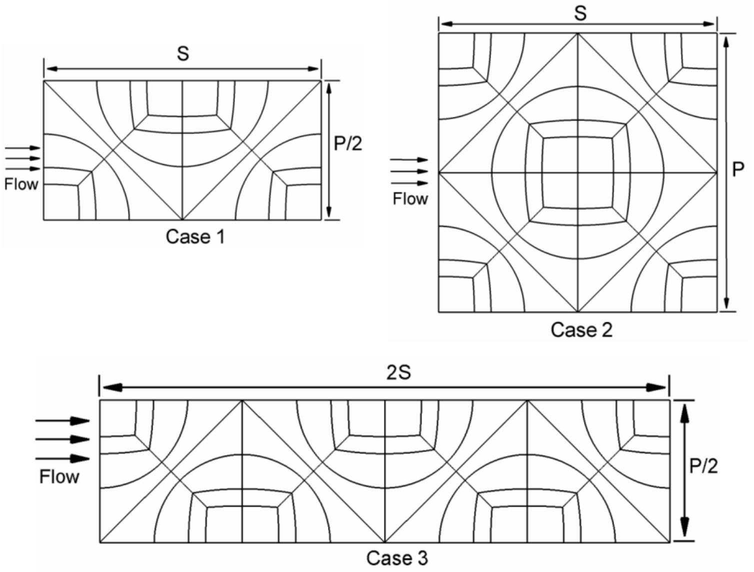

Figure 5.2: Domain independency study domain cases 1, 2, and 3.

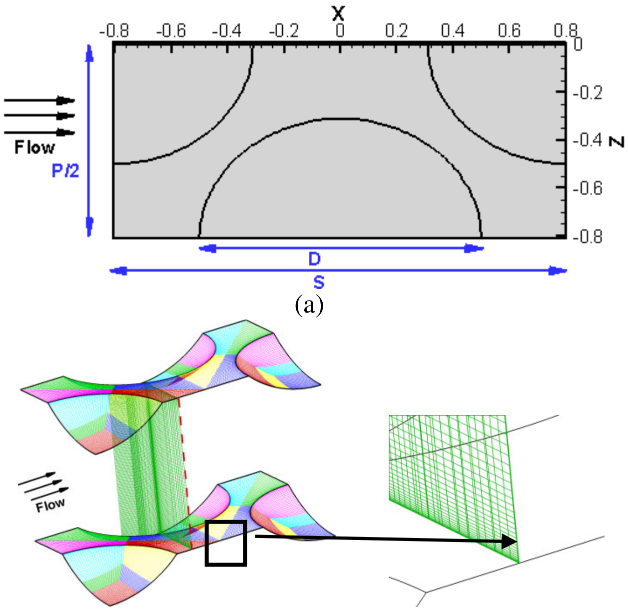

(a)

(b)

Figure 5.3: (a) 2D view of the selected computational domain; b) 3D view of the mesh topology in the domain with a close up view of the grid distribution in the y-direction in the domain very close to the dimple surface.

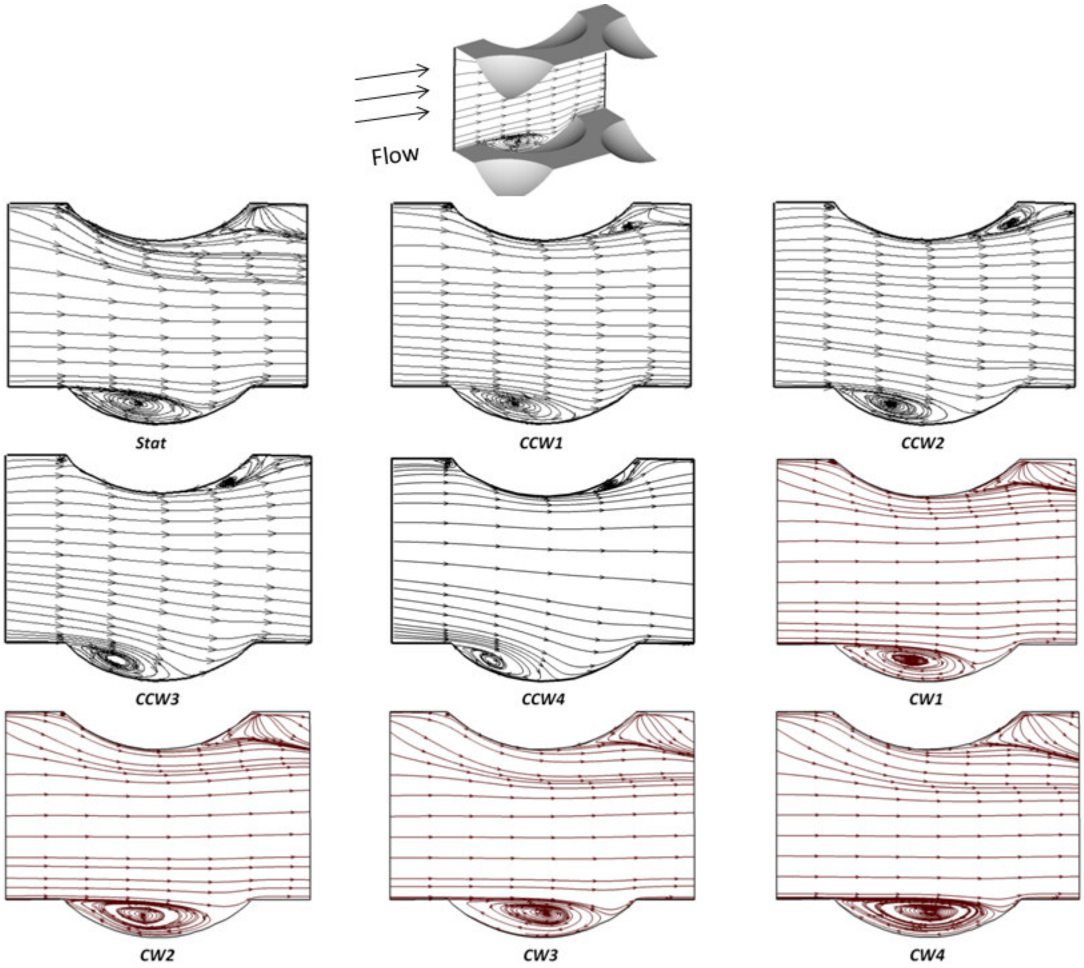

Figure 5.4: Velocity streamlines at a stream-wise plane (z=-0.81) located at the center of the dimple/protrusion at different rotation numbers (x-velocity contours) for the stationary and rotating cases for dimple depth, δ=0.2.

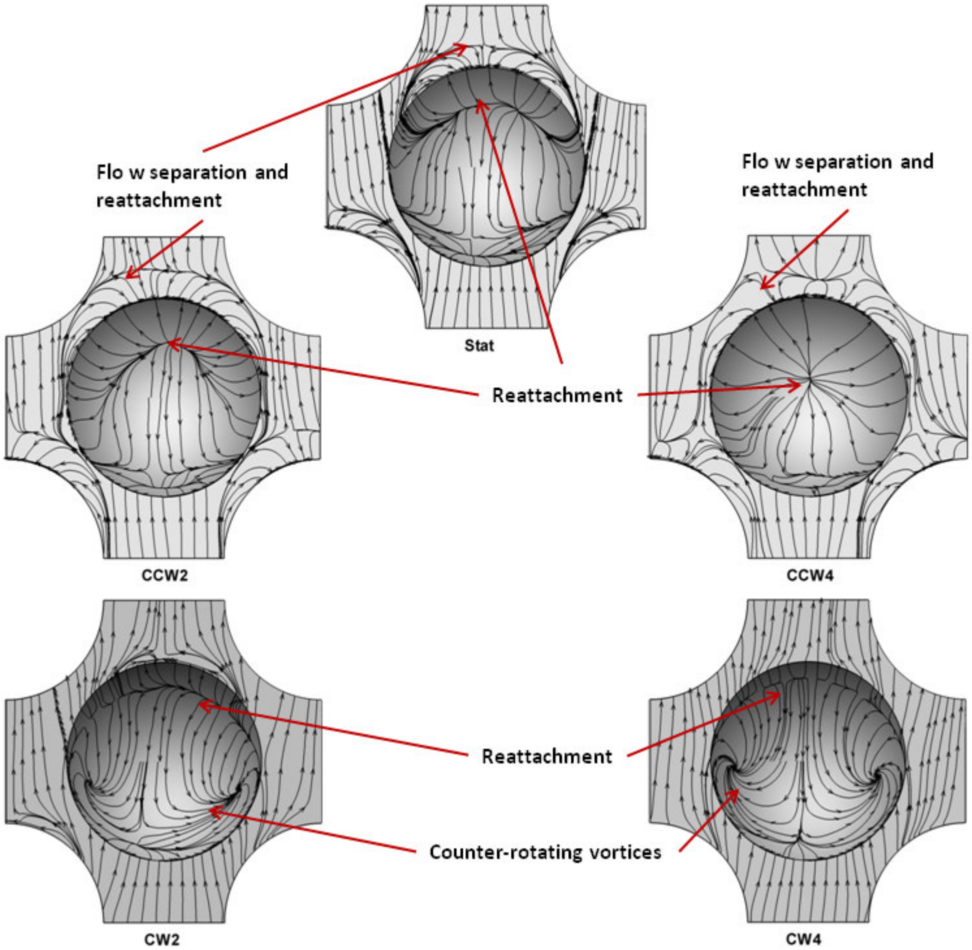

Figure 5.5: Velocity friction lines near the dimple surface for Stat, CCW2, CCW4, CW2, and CW4 cases. Note that the dimple surface is the leading side for Cases CW2 and CW4, and it is the trailing side for cases CCW2 and CCW4. Dimple depth, δ=0.2.

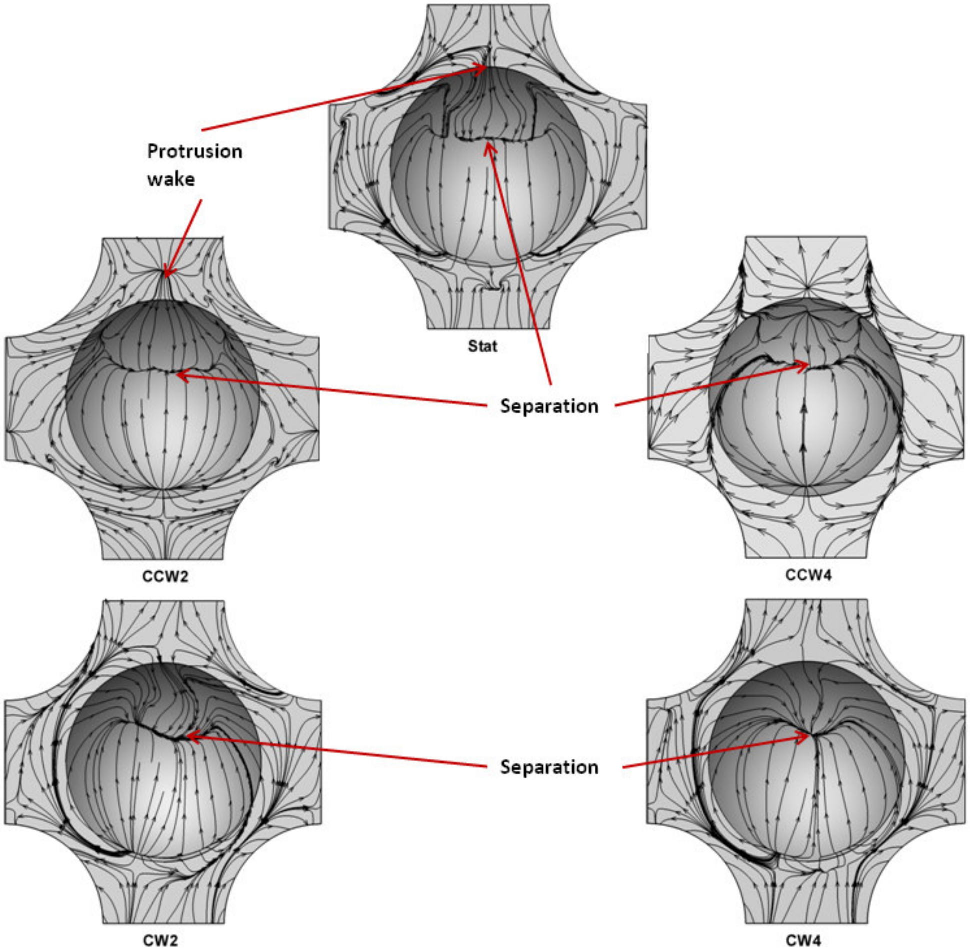

Figure 5.6: Velocity friction lines near the protrusion surface for Stat, CCW2, CCW4, CW2, and CW4 cases. Note that the protrusion surface is the trailing side for Cases CW2 and CW4, and it is the leading side for cases CCW2 and CCW4. Dimple depth, δ=0.2.

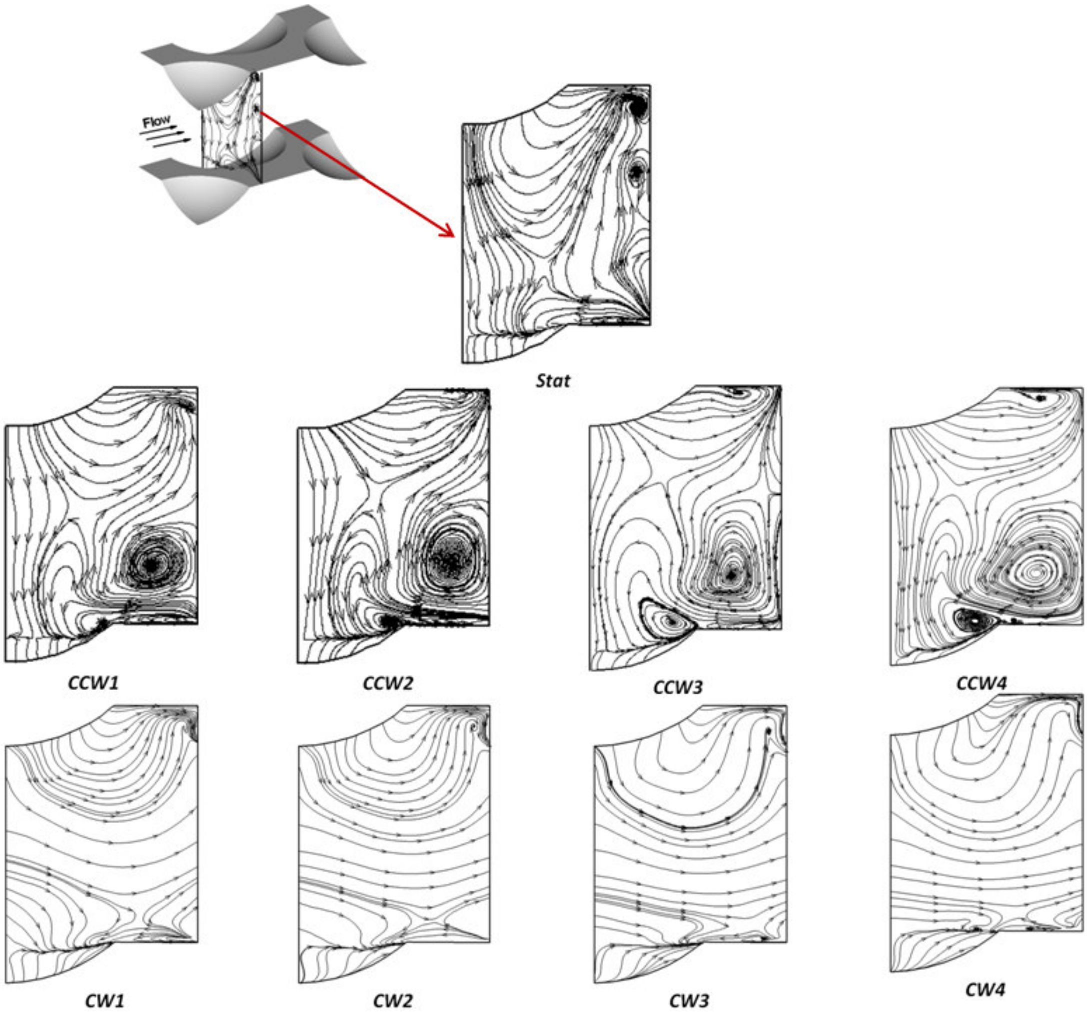

Stat

CCW1 CCW2 CCW3 CCW4

CW1 CW2 CW3 CW4

Figure 5.7: Secondary flow structure at a span-wise plane located 0.2D downstream of dimple for stationary and rotating cases for δ=0.2.

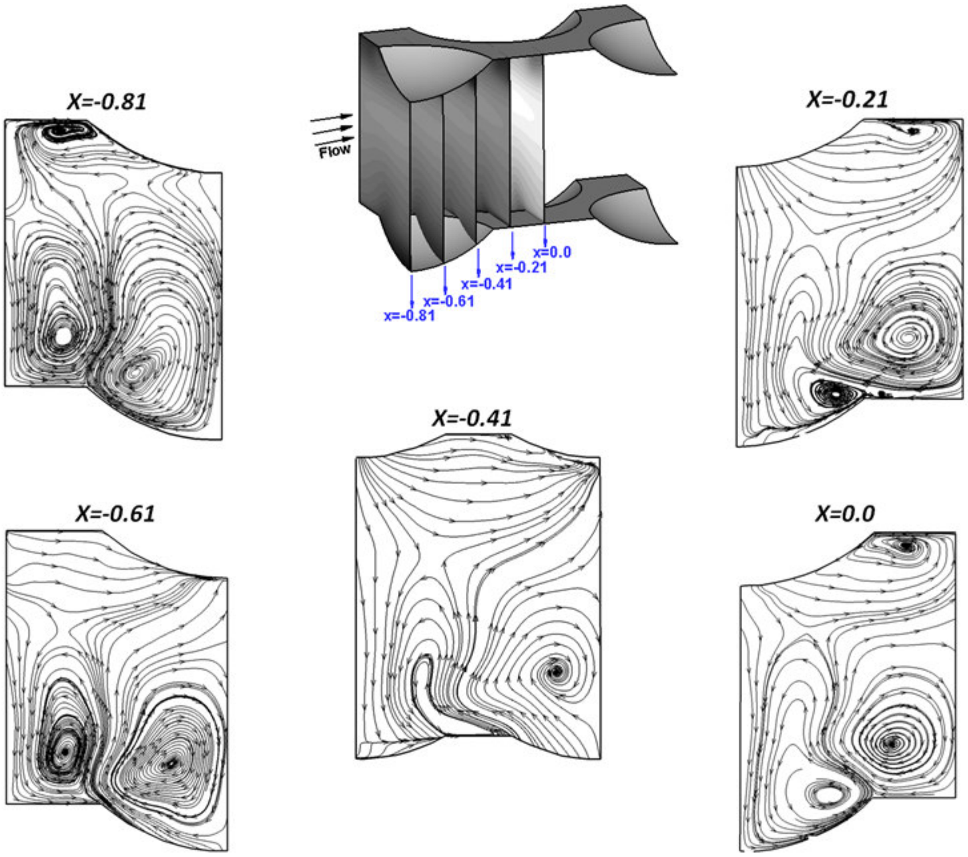

Figure 5.8: Secondary flow structure at selected span-wise planes for CCW4 case for δ=0.2.

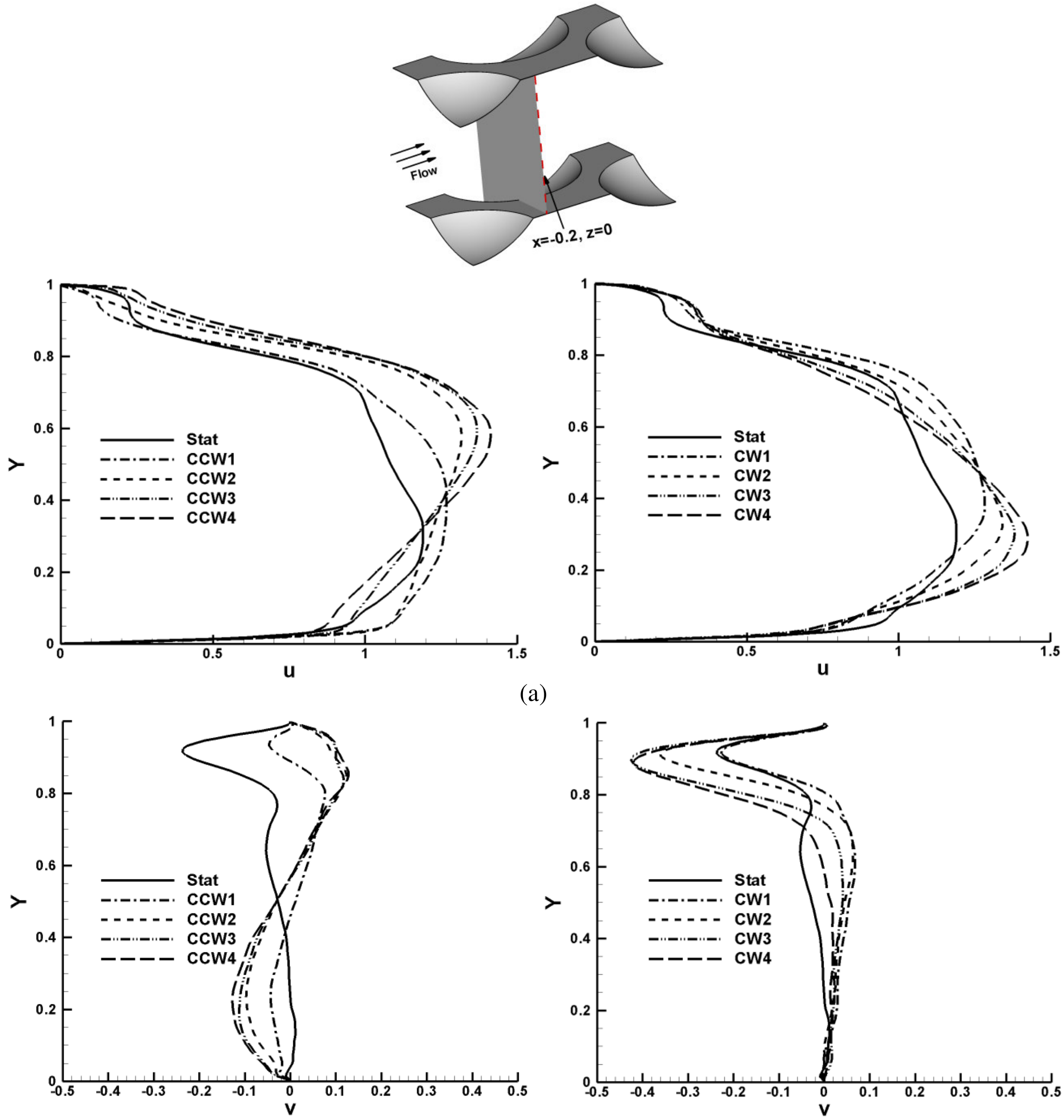

(a)

(b)

Figure 5.9: Stream-wise and cross-stream velocity profiles (normalized by mean bulk velocity) for different rotation numbers at 0.2D downstream of dimple (protrusion) (x=-0.21) and at centerline between dimples (z=0.0) for δ=0.2.

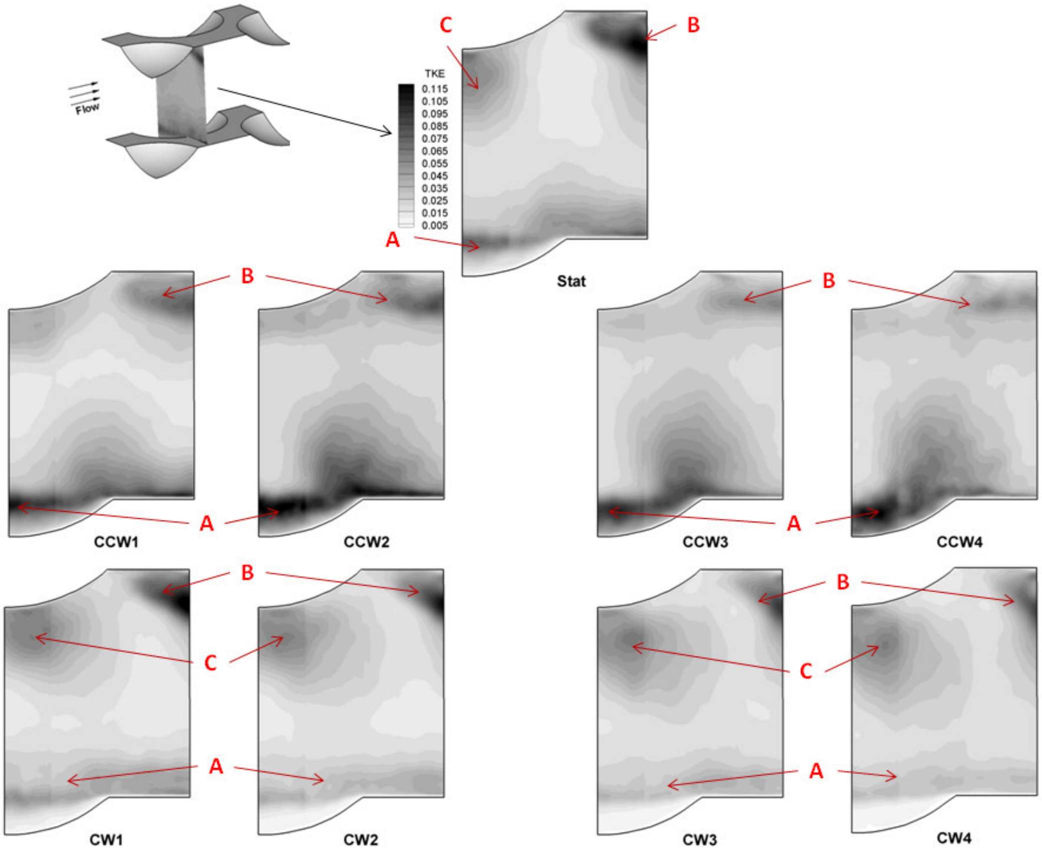

Figure 5.10: Normalized T.K.E. distribution at a span-wise plane 0.2D downstream of dimple (protrusion) (x=-0.2) for all rotation numbers for δ=0.2.

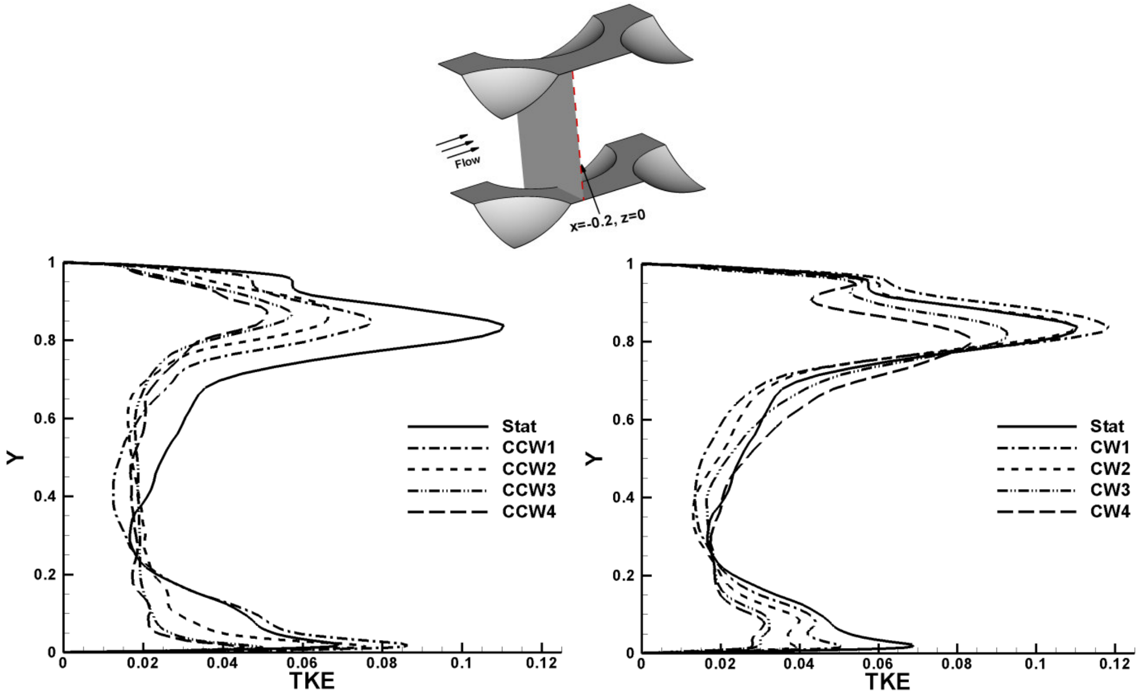

Figure 5.11: TKE profile at stream-wise plane x=-0.21 along the centerline of the dimple/protrusion (z=0) for δ=0.2.

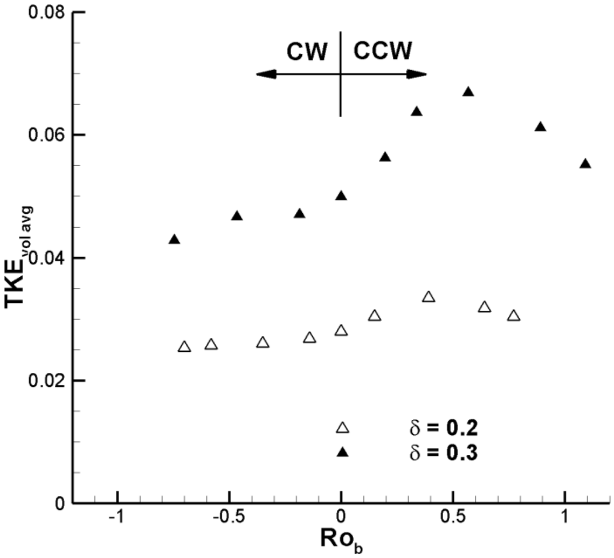

Figure 5.12: Volume averaged TKE values normalized by the bulk velocity squared for all rotation cases.

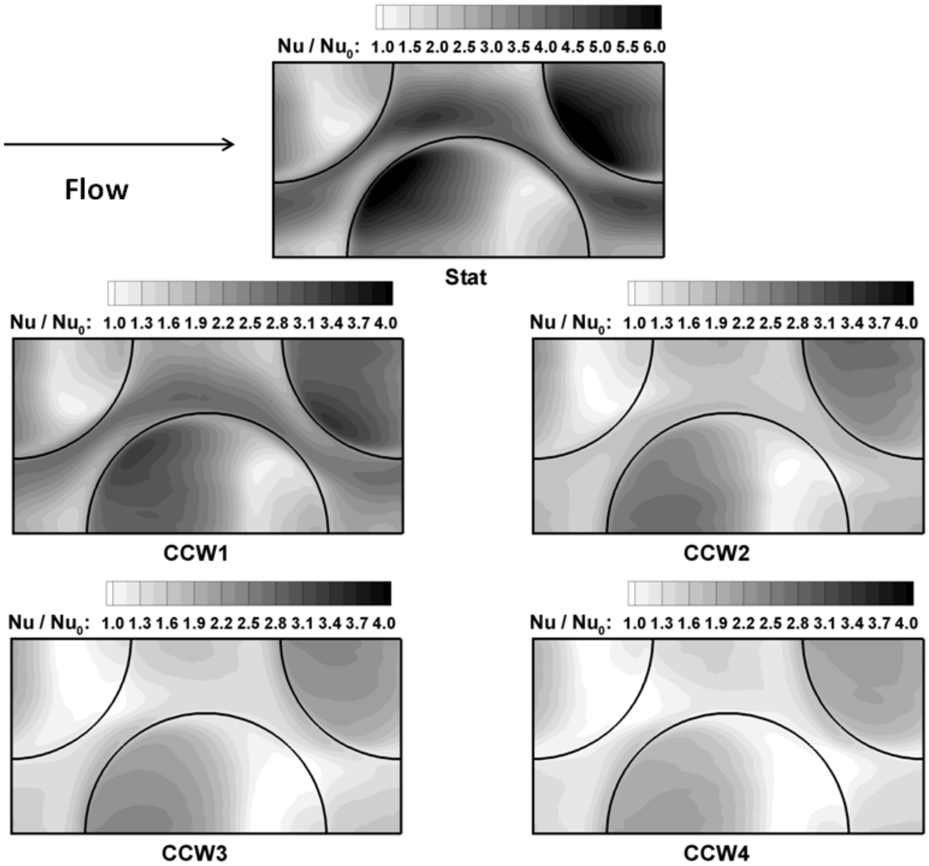

Figure 5.13: Mean Nusselt number augmentation distribution on the protrusion (leading) surface for the CCW rotating channel cases. (Flow from left to right)

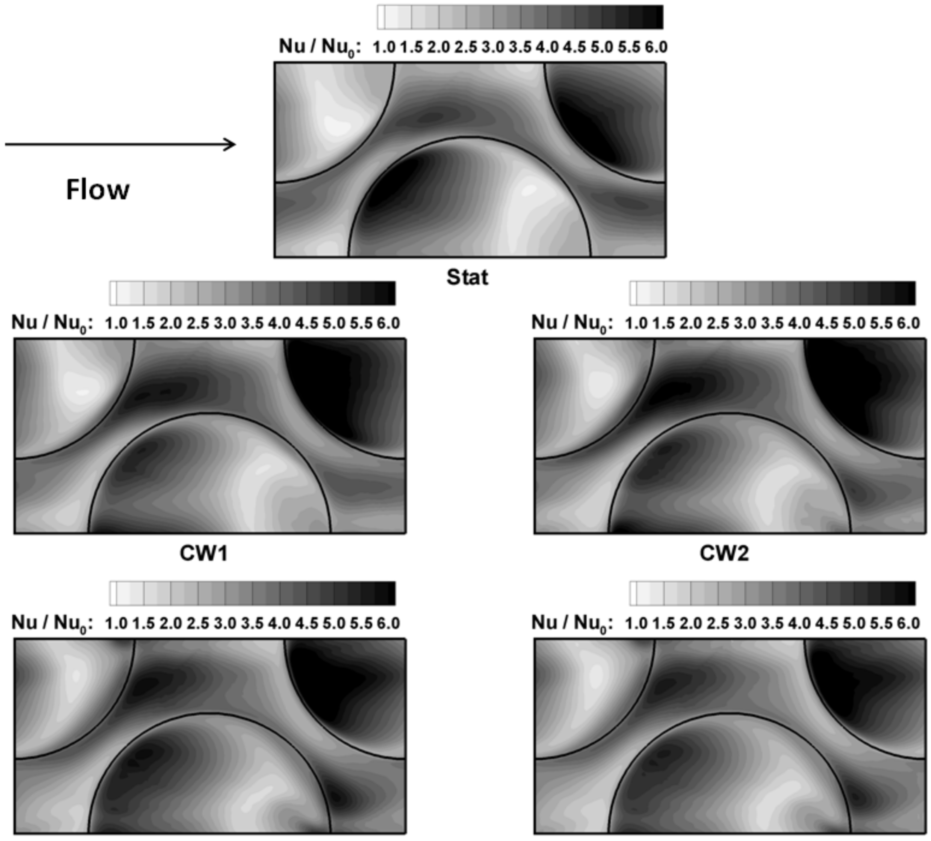

Stat

CW1

CW2

CW3

CW4

Figure 5.14: Mean Nusselt number augmentation distribution on the protrusion (trailing) surface for the CW rotating channel cases. (Flow from left to right)

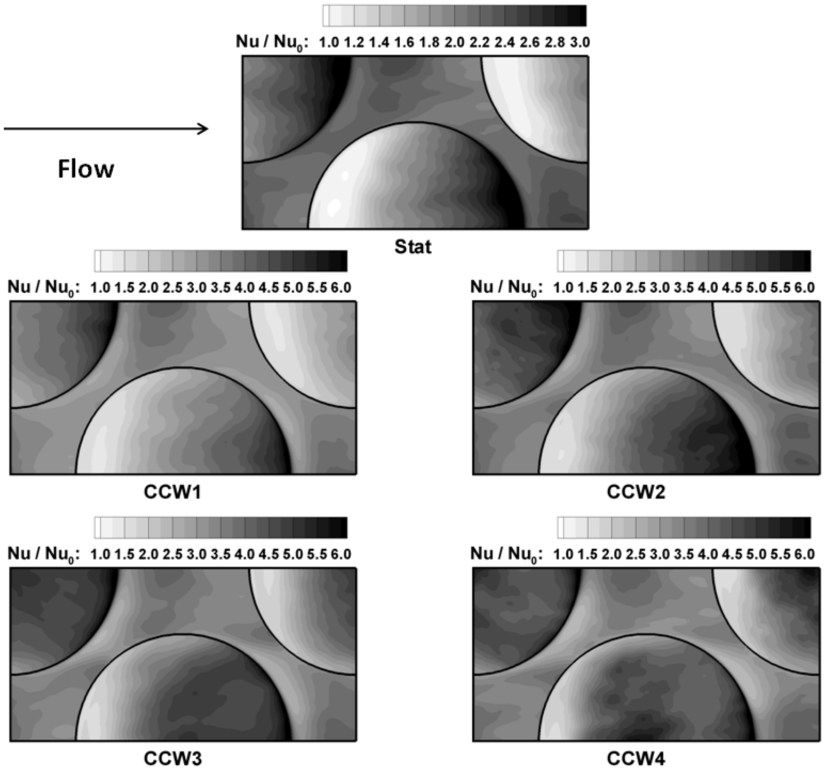

Figure 5.15: Mean Nusselt number augmentation distribution on the dimple surface for the CCW rotating channel cases. Flow from left to right)

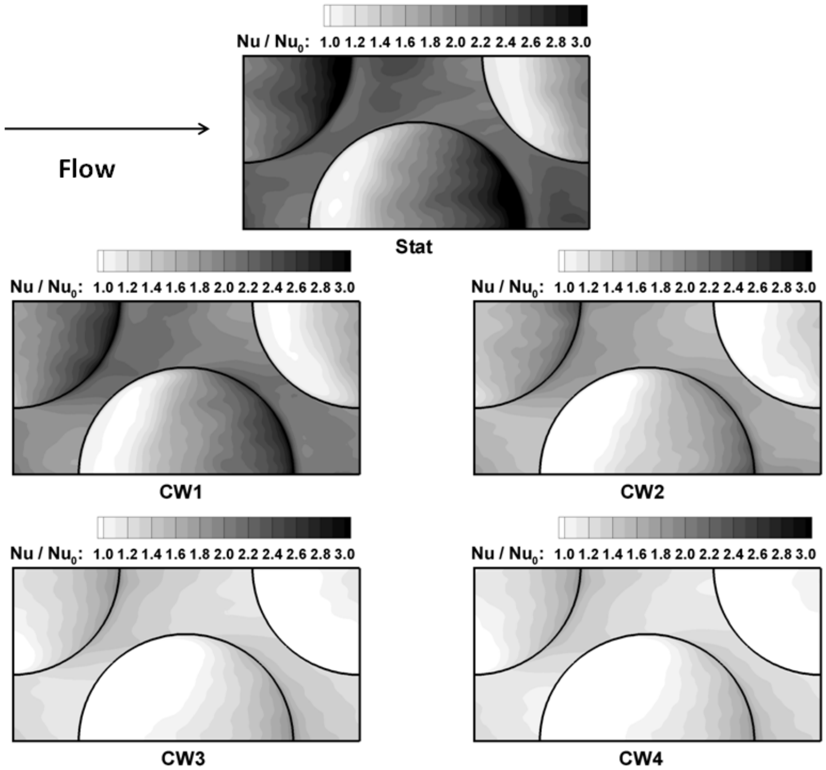

Figure 5.16: Mean Nusselt number augmentation distribution on the dimple surface for the CW rotating channel cases. (Flow from left to right).

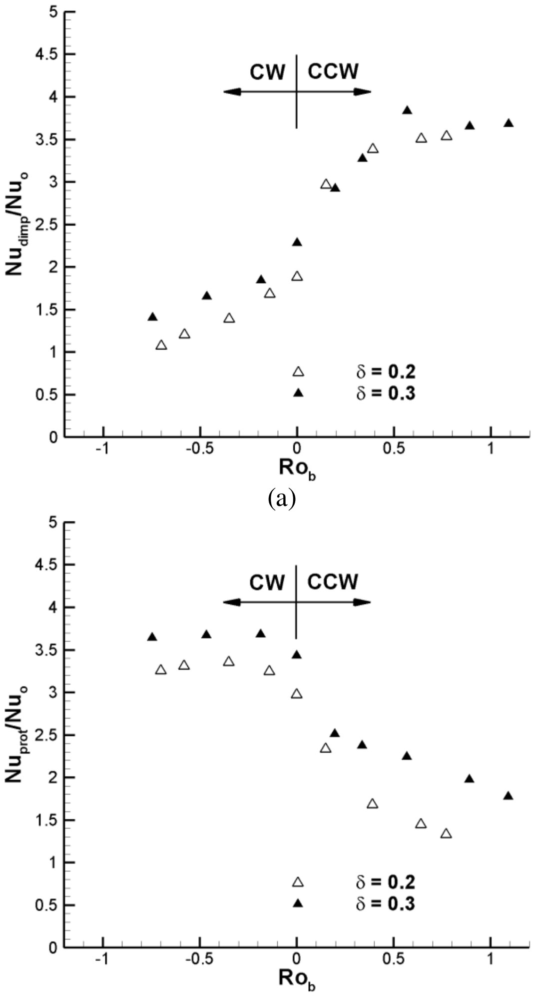

(a)

(b)

Figure 5.17: Time averaged area weighted Nusselt number of the: a) dimple side; b) protrusion side for both dimple depths.

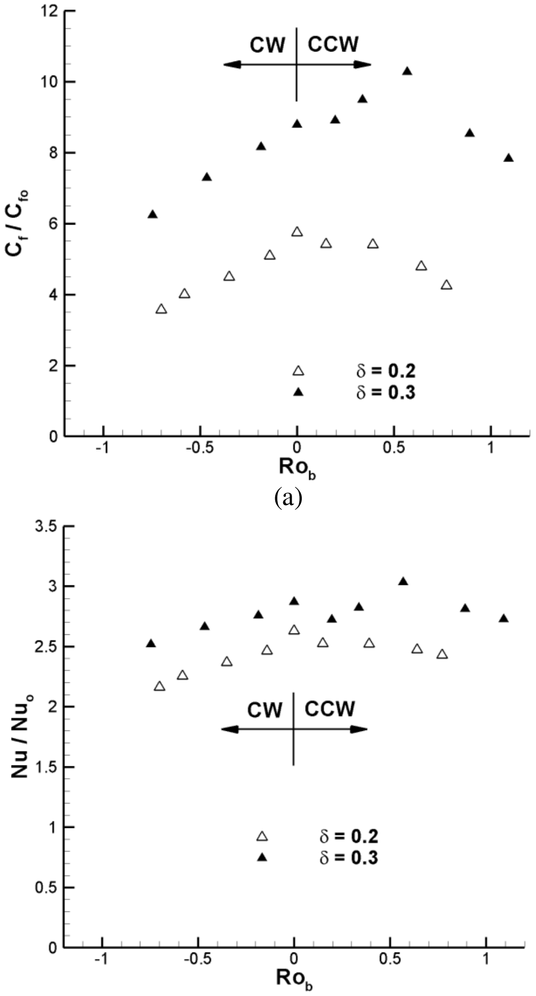

(a)

(b)

Figure 5.18: Variation of: a) friction coefficient ratio; and b) averaged Nusselt number augmentation.

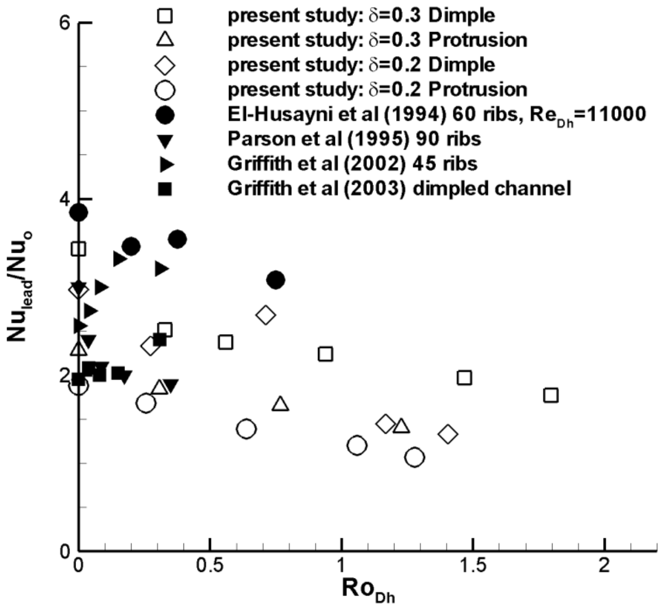

(a)

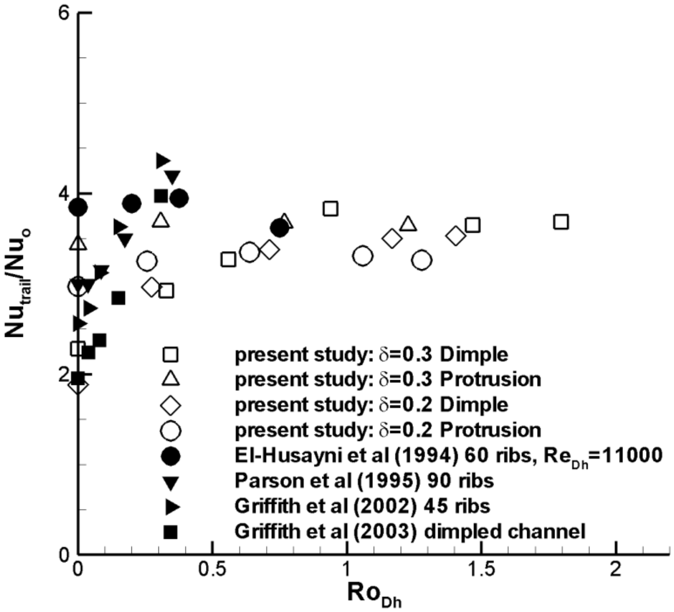

(b)

Figure 5.19: Comparison of Nusselt augmentation levels of the present study with experimental results for: a) leading surface; b) trailing surface.

Chapter 6: Summary and Conclusions:

High fidelity time dependent calculations were utilized to investigate different heat augmentation surfaces with modified dimples/protrusions for compact heat exchangers (Part I) and rotating turbine cooling applications (Part II). Part I consisted of three phases: Phase I considered dimpled continuous surfaces, Phase II considered dimpled plate fins, and Phase III investigated a novel fin shape, the split-dimple fin.

Phase I considered a channel with aligned dimples and protrusions for heat augmentation in compact heat exchangers. Two geometry cases were considered to study the channel height effect. Calculations of the dimpled channel covered the laminar to fully turbulent flow regime, Re_H=200-15000. Analysis of the flow structure showed that heat enhancement near the dimple surface is driven by separated shear layer reattachment inside the dimple cavity and vortex shedding out of the dimple cavity. Whereas flow impingement, acceleration, and wake reattachment on the protrusion side were the main heat enhancement mechanism. While the smaller fin pitch geometry was found to have better performance in low Reynolds number applications, heat transfer and pressure drop were almost insensitive to fin pitch for the fully turbulent flow regime.

Phase II investigated the application of dimples as surface roughness on plain fin surfaces. The dimple imprint diameter and perforation effect on flow structure and heat transfer from the surface were tested using three geometries. While the dimple imprint diameter did not produce any effect on the flow structure and heat transfer from the fin, the dimple perforation had a significant effect on the flow structure and heat transfer levels of the fin. Perforated dimple resulted in flow redirection between the top and bottom sides of the fin, reduced flow recirculation inside the dimple cavity, and further increased boundary layer regeneration from the fin surface, which resulted in higher heat transfer from the fin. Although the heat transfer levels of the perforated fin are comparable to those of the plain fin, it provided a 10% increase in the heat transfer area, which adds to its attractiveness as a viable option of heat enhancement.

Phase III investigated a novel fin design, the split-dimple fin, over a wide range of Reynolds number, Re_H=100 to 4,000, covering the laminar to fully turbulent flow regime.

Superior heat transfer augmentation levels over the conventional plain fin were produced with the split-dimple; this was mainly produced by additional boundary layer regeneration at fin and split-dimple edges, successful flow redirection between fin sides, enhanced flow mixing, and additional flow impingement on the protrusion surface. The split dimple augmented heat transfer by 60-175% over that of a plain fin but with 4-8 times the pressure drop penalty.

The second part of this research focused on the employment of dimple/protrusion surface roughness for internal cooling of rotating turbine blades. Coriolis forces effect was investigated on the flow structure and heat transfer distribution inside the channel for two dimple depth geometries, $\delta=0.2$ and 0.3. Simulations covered a wide range of rotation numbers, $Ro_b=-0.77$ to 1.1, where the positive rotation (CCW) places dimples on the trailing side and negative rotation (CW) places protrusions on the trailing side. When the channel rotates in the CCW direction, Coriolis forces energize the flow on the trailing dimple wall and induce early reattachment in the dimple cavity, also increasing the strength of the flow ejection out of the dimple cavity. While the protrusion side shows less energetic flow and results in a gradual growth of the wake. Negative rotation (CW) does not show a strong effect of Coriolis forces on the flow structure near the trailing surface—only a small shrinkage in the wake of the protrusion is observed. On the other hand, the leading (dimple) side shows delayed reattachment in the of the separated shear layer with the recirculation zone extending across the whole dimple. It is concluded that for low rotation number $|Ro_b|<0.2$, placing protrusions on the trailing side is advantageous, while for higher rotation number ($Ro_b>0.2$) placing dimples on trailing side gives better performance. Moreover, the deeper dimple geometry gives higher heat augmentation at the penalty of higher pressure drop.

Appendix: Complete Derivation of Rotational Source Terms

In this appendix the complete derivation of the governing equations of a channel rotating about an axis orthogonal to the main flow direction will be given[1]. Figure A.1 shows the general case of a particle (A) moving in space that has a position vector ($\overrightarrow{r^*}$) with respect to a reference frame (*xyz*) rotating at an angular velocity ($\overrightarrow{\omega^*}$), as shown in Figure A.1.

The non-inertial reference frame (*xyz*) is located at a position vector ($\overrightarrow{R^*}$) from an inertial frame (XYZ). The absolute acceleration of the particle (A) can be shown to be (*: denotes dimensional quantities)

$$\vec{a}^*_{abs} = \underbrace{\frac{d^2}{dt^{*2}}\vec{r}^*}_{I} + \underbrace{2\left[\vec{\omega}^* \times \frac{\partial \vec{r}^*}{\partial t^*}\right]}_{II} + \underbrace{\vec{\omega}^* \times \left(\vec{\omega}^* \times \vec{r}^*\right)}_{III} + \underbrace{\left[\frac{\partial \vec{\omega}^*}{\partial t^*} \times \vec{r}^*\right]}_{VI} + \underbrace{\vec{a}^*_o}_{V} \qquad \text{(A.1)}$$

where: I is the relative acceleration vector of the particle.

II is the Coriolis acceleration acting on the particle;

III is the centripetal acceleration

VI is the angular acceleration of the (*x, y, z*) reference frame.

V is the transitional acceleration of the (*x, y, z*) reference frame.

---

[1] This derivation borrows heavily from the text book of David Morris entitled "Heat Transfer and Fluid Flow in Rotating Coolant Channels," Research Studies Press, New York, 1981.

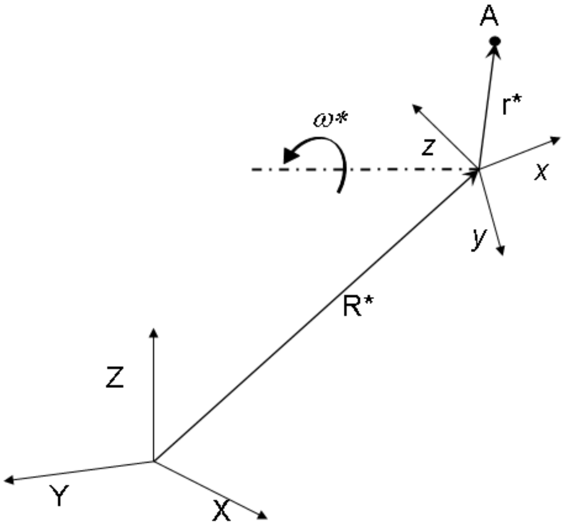

Figure A. 1: Particle motion about a rotating reference frame

For the special case of a fluid particle moving in a straight channel which rotates, at a uniform angular velocity ($\overrightarrow{\omega^*}$), about an axis orthogonal to the main flow direction, Figure A.2, the absolute acceleration of the particle (equation 13) reduces to:

$$\vec{a} = \left(\frac{\partial u^*}{\partial t^*} - 2\omega_z^* v^* - \omega_z^2 * (R^* + x^*) \right)\vec{i} + \left(\frac{\partial v^*}{\partial t^*} + 2\omega_z^* u^* - \omega_z^2 * y^* \right)\vec{j} \quad \text{(A.2)}$$

Note how the Coriolis and centripetal acceleration both have components in the x and y directions with no z-components for this special case,

Coriolis acceleration = $-2\omega_z^* v^* \vec{i} + 2\omega_z^* u^* \vec{j}$

Centripetal acceleration= $-\omega_z^2 * (R^* + x^*)\vec{i} - \omega_z^2 * y^* \vec{j}$

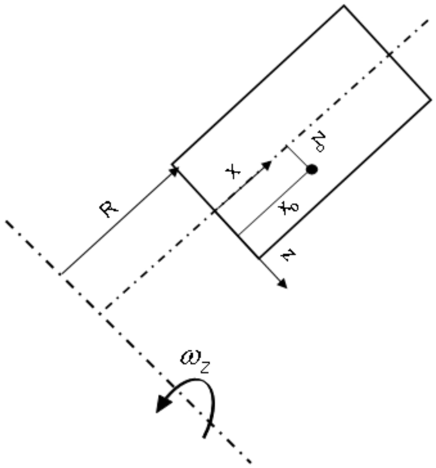

Figure A. 2: Straight duct rotating around an axis orthogonal to the flow direction

The effect of rotation can now be incorporated into the Navier-Stokes equations through the absolute acceleration term. In order to account for the density variation that might occur in the channel, a density gradient has been incorporated into the x-momentum equation

$$\left(\rho_o^* + \Delta\rho^*\right)\left(\frac{\partial u_i^*}{\partial t^*} + \vec{v}^* \bullet \nabla u_i - 2\omega_z^* v^* - \omega_z^2 {}^*(R^* + x^*)\right) = -\frac{\partial P^*}{\partial x_i^*} + \mu^* \nabla^2 u_i^*$$

(A.3)

With the assumption that the density gradient effect is important on the Coriolis and centrifugal buoyancy forces terms only and with simple expansion and manipulation of the different terms, equation A.3 can be reduced to

$$\rho_o^*\left(\frac{\partial u^*}{\partial t^*} + \vec{v}^* \bullet \nabla u^*\right) = -\frac{\partial P^*}{\partial x^*} + \mu^* \nabla^2 u^* + \left(\rho_o^* + \Delta\rho^*\right)\left(2\omega_z^* v^* + \omega_z^2 {}^*(R^* + x^*)\right)$$

$$\frac{\partial u^*}{\partial t^*} + \vec{v}^* \bullet \nabla u^* = -\frac{1}{\rho_o^*}\frac{\partial P^*}{\partial x^*} + \nu^* \nabla^2 u^* + \left(1 + \frac{\Delta\rho^*}{\rho_o^*}\right)\left(2\omega_z^* v^* + \omega_z^2 {}^*(R^* + x^*)\right)$$

(A.4)

The Boussinesq approximation is used to evaluate the density gradient in the fluid in terms of the temperature gradient,

$$\frac{\Delta\rho^*}{\rho_o^*} \cong -\beta_\rho^*\left(T^* - T_{ref}^*\right) \tag{A.5}$$

where β_ρ is the volume expansion coefficient of the fluid at constant pressure; $\beta_\rho^* = -\frac{1}{\rho_o^*}\left(\frac{\partial\rho^*}{\partial T^*}\right)_p$ and it is equal to $1/T_{ref}^*$ for ideal gases. T_{ref}^* is the dimensional mixed-mean reference temperature defined as $\left(T_{ref}^* = \frac{\iint |u^*| T^* dA_x}{\iint |u^*| dA_x}\right)$.

Substituting back in the x-momentum equation results in the following modified x-momentum equation

$$\begin{aligned}\frac{\partial u^*}{\partial t^*} + \vec{v}^* \bullet \nabla u^* &= -\frac{1}{\rho_o^*}\frac{\partial P^*}{\partial x^*} + \nu^* \nabla^2 u^* \\ &\quad + \left[1 - \beta_\rho^*\left(T^* - T_{ref}^*\right)\right]\left(2\omega_z^* v^* + \omega_z^2 * (R^* + x^*)\right)\end{aligned}$$

$$\begin{aligned}\frac{\partial u^*}{\partial t^*} + \vec{v}^* \bullet \nabla u^* &= -\frac{1}{\rho_o^*}\frac{\partial P^*}{\partial x^*} + \nu^* \nabla^2 u^* + 2\omega_z^* v^* - \beta_\rho^*\left(T^* - T_{ref}^*\right)2\omega_z^* v^* \\ &\quad + \omega_z^2 * (R^* + x^*) - \beta_\rho^*\left(T^* - T_{ref}^*\right)\omega_z^2 * (R^* + x^*)\end{aligned} \tag{A.6}$$

Following the same procedure for the y-momentum equation, the y-momentum equation becomes

$$\begin{aligned}\frac{\partial v^*}{\partial t^*} + \vec{v}^* \bullet \nabla v^* &= -\frac{1}{\rho_o^*}\frac{\partial P^*}{\partial x^*} + \nu^* \nabla^2 v^* - 2\omega_z^* u^* + \beta_\rho^*\left(T^* - T_{ref}^*\right)2\omega_z^* u^* \\ &\quad + \omega_z^2 * (y^*) - \beta_\rho^*\left(T^* - T_{ref}^*\right)\omega_z^2 * (y^*)\end{aligned} \tag{A.7}$$

It can seen that the Coriolis and centrifugal buoyancy appear as source terms in the Navier-Stokes equations

1. x-momentum:

$$F_x = 2\rho^*\omega_z^* v^* - \beta_\rho^*\left(T^* - T_{ref}^*\right)2\omega_z^* v^* + \rho^*\omega_z^2 * (R^* + x^*) - \beta_\rho^*\left(T^* - T_{ref}^*\right)\omega_z^2 * (R^* + x^*)$$

2. y-momentum:

$$F_y = -2\rho^*\omega_z^* u^* + \beta_\rho^*\left(T^* - T_{ref}^*\right)2\omega_z^* u^* + \rho^*\omega_z^2 * y * - \beta_\rho^*\left(T^* - T_{ref}^*\right)\omega_z^2 * (y^*)$$

Since the radius of rotation of the channel (R^*) is typically much larger than the y-coordinate of the channel (y^*) and assuming that the mean centrifugal buoyancy term is combined with the mean pressure gradient, the centrifugal buoyancy force in the y-direction can be neglected. Thus, the source term in the y-direction will account for the Coriolis forces only, i.e. $F_y = -2\rho^* \omega_z^* u^*$.

Non-dimensionalizing the Navier-Stokes equations with the characteristic length scale (fin height, H^*), velocity scale (friction velocity, u_τ), and time scale (H^*/ u_τ), the x and y momentum equations reduce to

x-momentum:

$$\frac{\partial u}{\partial t} + \vec{v} \bullet \nabla u = -\frac{\partial P}{\partial x} + \frac{1}{Re_\tau} \nabla^2 u + 2Ro_\tau v - Ri_\tau \left(T - T_{ref}\right) + Ro_\tau^2 (R + x) \qquad \text{(A.8)}$$

y-momentum:

$$\frac{\partial v}{\partial t} + \vec{v} \bullet \nabla v = -\frac{\partial p}{\partial y} + \frac{1}{Re_\tau} \nabla^2 u_i - 2 Ro_\tau u \qquad \text{(A.9)}$$

where Ro_τ is the rotation number of the channel defined as $Ro_\tau = \frac{\omega_s H}{u_\tau}$. Ri_τ is the Richardson number of the flow defined as $Ri_\tau = -\beta_\rho Ro_\tau^2 (x + R)$.

The above formulation of the governing equations implies the following assumptions:

1. The mean centrifugal buoyancy is combined with the pressure gradient term.
2. The effect of variable density only appears in the centrifugal buoyancy term.
3. Centrifugal buoyancy contribution is neglected in the y-direction.
4. The Boussinesq approximation is valid (ΔT small).

For the special case of a fully developed periodic channel rotating about an axis orthogonal to the main flow direction (Chapter 5), the mean pressure and temperature gradients are isolated from the fluctuating periodic components (Chapter 5) and the x and y momentum equations take the form

$$\begin{aligned} \frac{\partial u_i}{\partial t} + \vec{v} \bullet \nabla u_i = -\frac{\partial p}{\partial x_i} + \frac{1}{Re_\tau} \nabla^2 u_i + 2 Ro_\tau u_j \varepsilon_{i3m} \\ - Ri_\tau \left(\theta - \theta_{ref}\right) \delta_{i1} + \beta\, \delta_{i1} \end{aligned} \qquad \text{(A.10)}$$

where θ is the modified fluctuating non-dimensional temperature. θ_{ref} is the volume-weighted average of the modified non-dimensional temperature. β is the mean streamwise pressure gradient defined earlier in Chapter 5, $\beta = \frac{4}{D_h}$.

The above treatment of the periodic rotating channel assumes that the Richardson number is constant, i.e. represents a fixed radial location, for compatibility with the fully developed flow assumption, in addition to the assumptions listed above.